sciendo

Identification of corrosion products on iron artefact from Bratislava castle

Roman Košťúr, Matilda Zemanová

Institute of Inorganic Technologies and Materials, Slovak University of Technology, Radlinského 9, 812 37 Bratislava, Slovakia
roman.kostur@stuba.sk

Abstract: Corrosion layers of an iron artefact were characterized to study long-term exposition of iron in Slovakia. The iron artefact from Bratislava castle has been coated with a strong layer of corrosion products and masonry residues. Corrosion products were characterized by different methods including energy-dispersive X-ray spectroscopy (EDX), X-Ray diffraction (XRD), and μ-Raman Spectroscopy. Magnetite and goethite on the surface are confirmed typical corrosion products from long-term atmospheric exposure in environment with corrosivity category C-2 (low).

Keywords: corrosion layers, Bratislava castle, magnetite, goethite

Introduction

Iron and ferrous alloys are susceptible to corrosion deterioration which can lead to damage of historical or archaeological pieces and the loss of their aesthetic aspects including disappearing of information, change in shape or loss of function (Neff, 2013).

Reactivity of metals and the susceptibility to corrosion can be influenced by many factors due to the type of atmosphere there are exposed to. The studied iron artefact from Bratislava castle was exposed to outdoor atmosphere and the main factor influencing its reactivity was rainfall (Bernard, 2009). Other factors responsible for atmospheric corrosion are humidity, temperature, pollutant concentration, dust particles and time of wetness (Schweitzer, 2010). Corrosion can endanger the conservation of an artefact by partially or completely corroding the metallic core.

The study of long-term corrosion of iron is relevant especially in the context of conservation and restoration. It is very important to understand corrosion mechanisms in metallic heritage artefacts to diagnose the alteration behavior of metallic artefacts and to subsequently adapt their treatment and storage (Saheb, 2013).

Each corrosion product has a different impact on the corrosion system. Corrosion systems containing iron corrosion products magnetite (Fe_3O_4) and goethite (α — FeO(OH)) are considered as stable, whereas akaganeite (β — FeO(OH)) and lepidocrocite (γ — FeO(OH)) are considered as degradation accelerators (Veneranda, 2018).

There are two basic procedures in corrosion protection of metallic heritage artefacts. If the metallic core of an historical artefact is not sufficiently preserved, it is recommended to stabilize the layers of corrosion products by elimination of corrosion stimulants. On the other hand, for objects with thin layers of corrosion products with sufficiently preserved metallic core, the second procedure should be applied, which includes complete elimination of corrosion products (stimulants) followed with conservation of clean metal surface (Šilhová, 2011).

An iron artefact (Fig. 1) was found during work at eastern terrace in Bratislava castle in 2015. Excavations were carried out under the direction of M. Samuel, Archaeological Institute of the Slovak Academy of Science (AÚ SAV) in Nitra. The artefact was identified as ironwork with age estimated to about 300 years (personal communication with Dr. P. Bednár, AÚ SAV, Slovakia).

Bratislava castle has been the dominant of the town Bratislava for centuries from its first written reference in 907 to present. It is located on an isolated rocky hill of the Little Carpathians above the Danube river (Čambal, 2014). Residents of the castle, who changed many times, contributed to the history and reconstruction of the castle. Under the reign of Maria Theresa extensive redevelopment of the castle had been taking place. Another important milestone in the history was the use of the castle as barracks for soldiers at the beginning of the 19th century. Clumsiness of soldiers caused a fire and the castle burnt down. However, it was still used by the army and changed to ruins. The army left the castle after World War II. Recovery and reconstruction of the castle was initiated by the artist and writer Janko Alexy in 1953. Since then, the Bratislava castle has become a part of cultural heritage. After the reconstruction it has become the residence of the Slovak National Museum and representative halls of the Slovak National Council. An extensive archaeological and research project was conducted here between 2008—2014. The main target was to reconstruct the castle and its surround-

ings into the form it had after the reconstruction during the reign of Maria Theresa (http://www.bratislava-hrad.sk/historia 29. 9. 2020).
Atmospheric corrosivity category for Bratislava castle for carbon steel was estimated to be C-2 (low pollution) according to standard EN ISO 9223:2012 (personal communication with Dr. K. Kreislová, SVÚOM, s.r.o., Czech Republic).
The aim of this work was to identify corrosion product layers in an iron artefact from Bratislava castle to evaluate its corrosion damage. Corrosion product layers formed on the iron artefact were analyzed by different techniques such as XRD, EDX and μ-Raman Spectroscopy.

Material and Methods

Description of the iron artefact
The examined iron artefact (Fig. 1) is about 35 cm long, twisted inwards on one side; a protruding nail (about 5 cm long) can be found 10 cm from the twist. The object lent by AÚ SAV in Nitra was identified as a 300-year-old ironwork found in eastern terrace of Bratislava castle.
The whole object is covered with a thick layer of corrosion products and masonry residues which partially fell off during handling. However, the metal core seems to be preserved. Corrosion products are brown to orange in color. Various crusts and blisters formed on the surface of the object.
The cut sample was photographed by a digital camera (Fig. 2). Fig. 2 shows three specific areas marked with different color circles. The white-grey part marked with a red circle is possibly masonry residue. In reference to corrosion product layers,

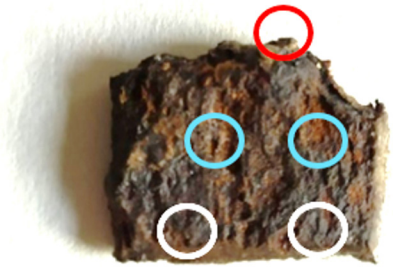

Fig. 2. Digital photograph of the cut sample from the ironwork.

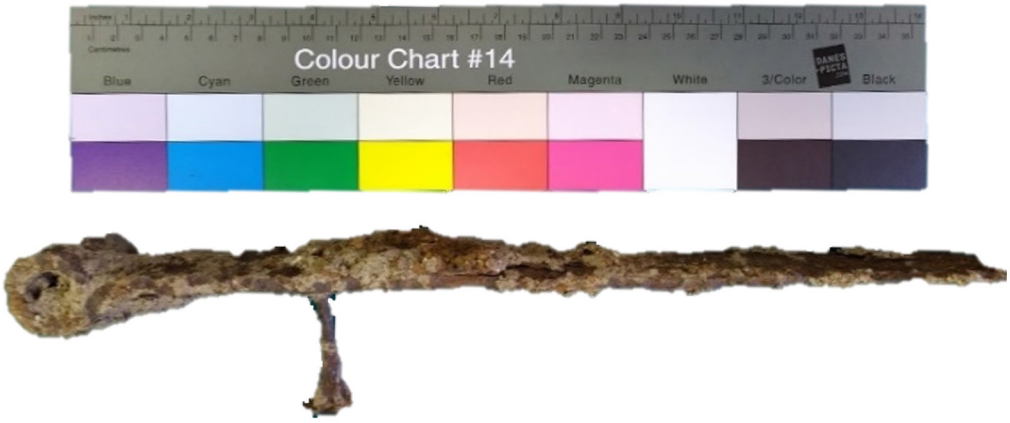

a)

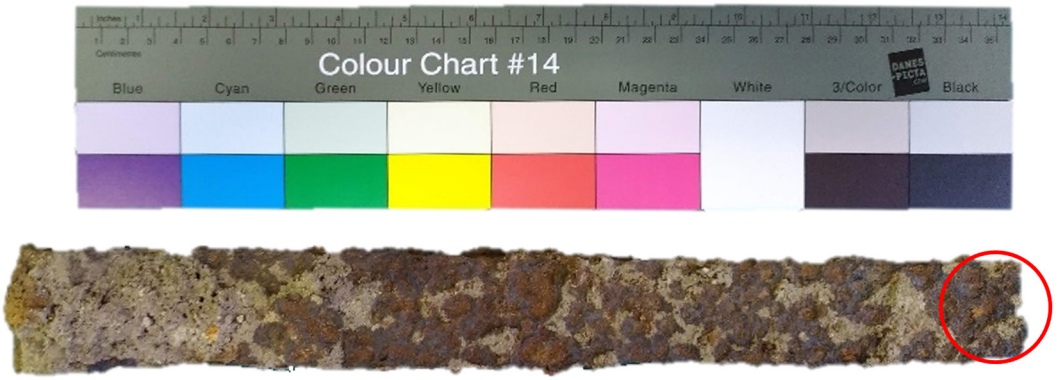

b)

Fig. 1. Ironwork from Bratislava castle (Slovakia) with corrosion products and masonry residues: a) side view, b) top view.

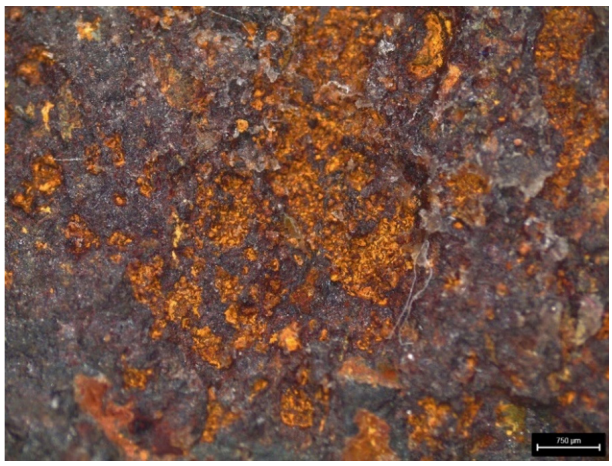

Fig. 3. Detailed micrograph of the ironwork.

two different colors of corrosion products are distinguished. The area marked with blue circles presents the typical red-orange color of rust. Another type of corrosion product with dark brown-black color is marked with white circles. A more detailed photograph was taken by a stereomicroscope Stereozoom Leica S9 (Fig. 3). Fig. 3 shows orange corrosion product as well as a dark brown form of the corrosion products.

Sample preparation

The cut specimen was embedded in epoxy resin. The sample was grinded with abrasive paper SiC under water from P320 up to P2000 (grit size), then polished with different diamond pastes up to 1 µm. The polished sample was rinsed with ethanol and dried with hot air from a heater.

Identification and characterization of corrosion products

Three different areas shown in Fig. 4 were observed using a scanning electron microscope (Zeiss EVO 40HV, Germany) equipped with a EDX analyzer Bruker Axs (Germany) for element composition of the selected areas. Fig. 4a shows the surface of the sample, Fig. 4b and Fig. 4c depict the cross-section. Identification of crystalline phases in the corrosion product layers was done by XRD on the sample

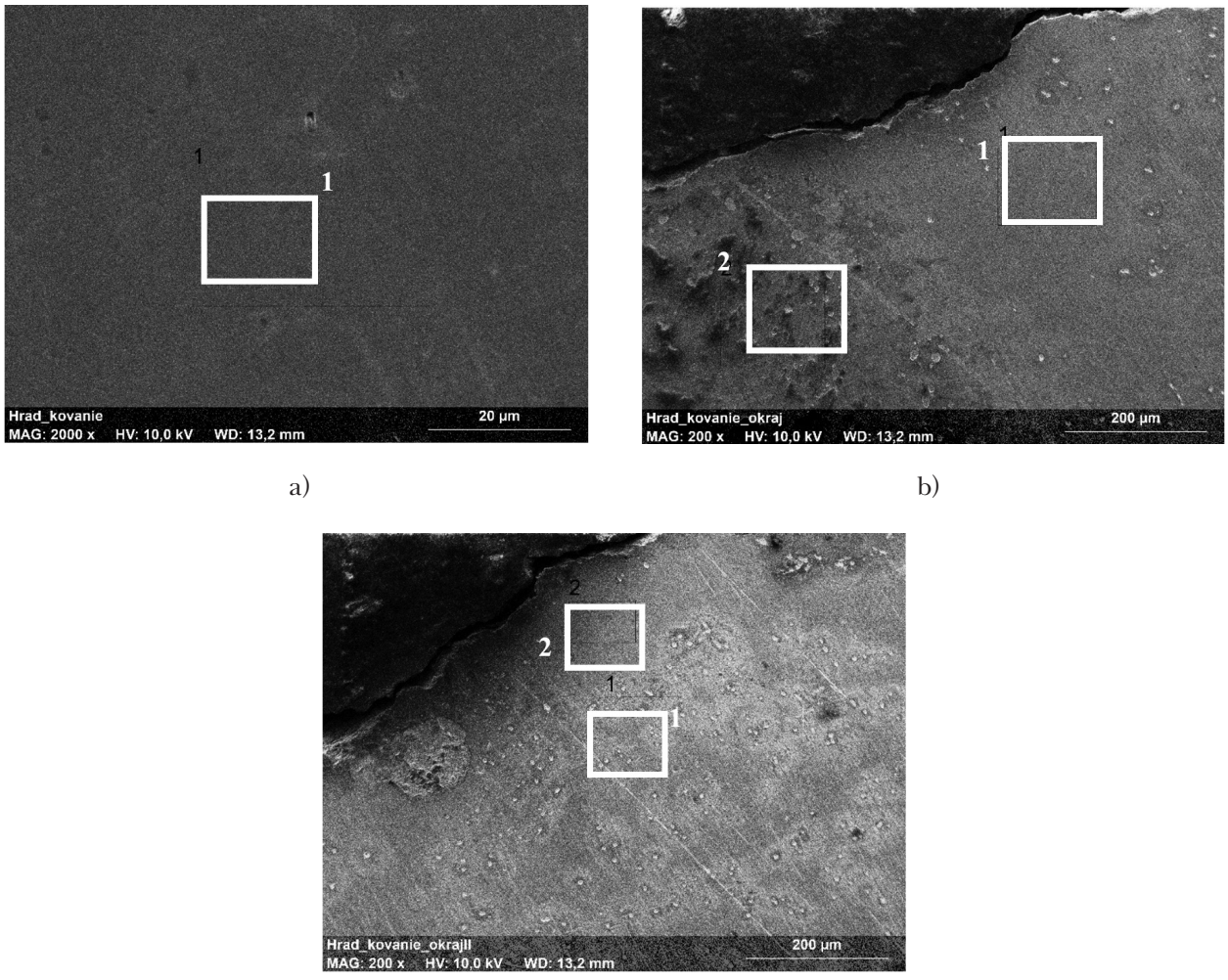

Fig. 4. SEM images with selected areas for EDX measurements.

cross-section. XRD was recorded within the 2Θ range of 3°—90° on an automatic powder diffractometer with Brag-Brentano focusing geometry (Philips PW1700, The Netherlands). The instrument was equipped with an X-ray tube providing Co Kα radiation.

Measurements of corrosion products by μ-Raman spectroscopy were realized on the cross-section of the samples (Raman Microscope DXR IMA4476). Raman excitation was provided by a laser operating at 532 nm.

Results and Discussion

Corrosion layer analysis

All results from EDX analysis are summarized in Tab. 1. The sample from the iron artefact (Bratislava castle) corresponds to wrought iron (to 2.1 wt. % of C) according to surface elemental analysis. Higher carbon content in the cross-section at the edge of samples may be due to the residues of the previous historical surface treatment (bluing). EDX analysis also shows that phosphorus and silicon content is below 1 wt. % except one measurement with high amount of silicon due to masonry residues.

XRD pattern is shown in Fig. 5. Two corrosion products of iron were identified: magnetite and goethite. There were additional strong lines for calcite and quartz which confirm the presence of masonry residue in the sample.

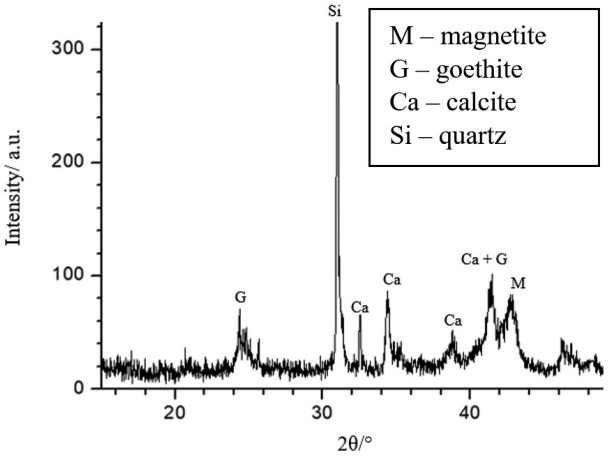

Fig. 5. XRD patterns for the iron artefact sample (Bratislava castle).

Magnetite, goethite and lepidocrocite are the main phases identified in the sample by μ-Raman Spectroscopy. The spectra were taken from inner and outer layer of corrosion products on the cross-section of the cut sample. The intensive band at 670 cm^{-1} (width from 600—750 cm^{-1}) and weak

Tab. 1. Elemental composition from EDX analysis of the iron artefact sample (wt. %).

measurement spot	type of analysis	spectrum	magnification	Fe	O	C	Mn	Si	P	K
„Fig. 4 A“	surface	1	2000×	98.23	1.28	0.10	–	–	0.39	–
„Fig. 4 B“	cross-section	1	200×	95.02	3.63	0.47	–	0.78	–	0.18
„Fig. 4 B“	cross-section	2	200×	31.70	43.64	3.73	–	20.62	0.31	–
„Fig. 4 C“	cross-section	1	200×	82.33	13.13	2.33	0.99	0.72	0.50	–
„Fig. 4 C“	cross-section	2	200×	93.38	3.31	0.61	1.58	0.39	0.80	–

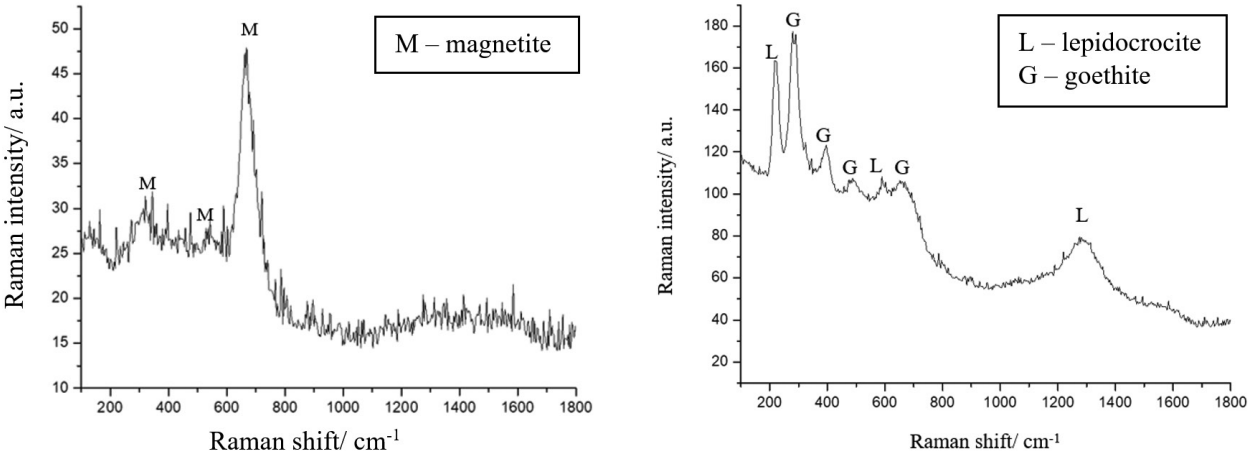

a) b)

Fig. 6. Raman spectra for two areas of corrosion layers on the ironwork.

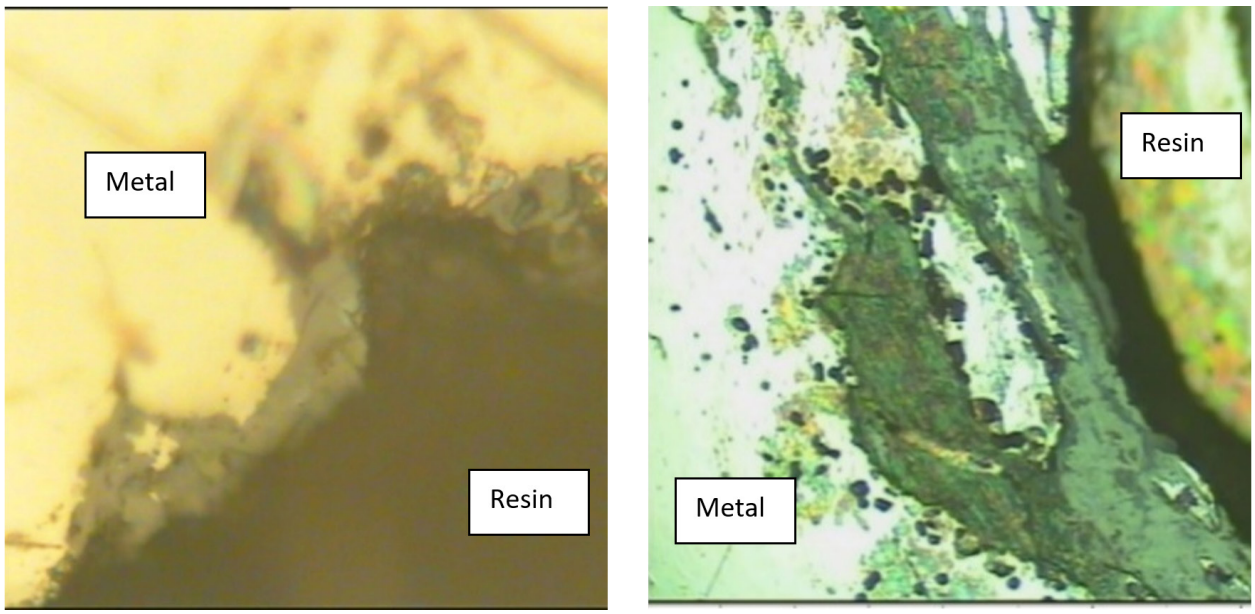

a) b)

Fig. 7. Corrosion layers on metallic core of the ironwork (Bratislava castle).

bands at 310 cm^{-1} and 580 cm^{-1} are attributed to magnetite from the inner layer of the corrosion products (Fig. 6a). Outer layer consists of goethite and lepidocrocite. Bands at about 300 cm^{-1}, 390 cm^{-1} and 680 cm^{-1} are attributed to goethite. Lepidocrocite was identified at about 250 cm^{-1}, 520 cm^{-1} and 1300 cm^{-1} (Fig. 6b) (Bellot-Gurlet, 2009; Grousset, 2016; Rocca, 2019; Neff, 2006).

Based on the obtained results and in accordance with literature (Neff, 2013) it is possible to present the structure of the studied iron artefact (Fig. 7). The layer of corrosion products can be divided into three parts: internal part, close to the metal substrate, is attributed to magnetite; outer part of the corrosion layer consists of two identified oxo-hydroxides (goethite, lepidocrocite); middle part is identified as goethite and magnetite. Metallic core is sufficiently preserved; however, it is clearly seen that corrosion damage affects the core of the substrate in two forms: pitting (Fig. 7a) and penetration into the metallic core (Fig. 7b).

EDX analysis showed that the elemental composition, apart from the corrosion products of iron, is formed by various dust particles or masonry residues. It is clearly seen at the edge of sample I, spectrum 2 (Tab. 1), with high content of Si (20.6 wt. %), O (43.6 wt. %). The result was confirmed by XRD analysis as quartz (SiO_2). Results obtained from XRD analysis showed that main corrosion products are magnetite and goethite. XRD analysis is considered as analysis in the macroscale range (Monnier, 2013). The presence of magnetite (680 cm^{-1}) was confirmed by μ-Raman Spectroscopy in the inner layer of corrosion products. Magnetite is usually black in color and occurs as a bottom layer of corrosion products, mostly under red brown-orange corrosion products of iron. Red brown-orange corrosion products contain lepidocrocite and goethite (oxo-hydroxides of iron). μ-Raman Spectroscopy serves to identify the compounds in microscale range. On the top of the layer surface, goethite and lepidocrocite were recognized; goethite as a stable form and lepidocrocite as an unstable form of iron corrosion products. Lepidocrocite as an unstable form can communicate with the atmosphere promoting corrosion reaction.

Conclusion

An iron artefact (ironwork) from Bratislava castle dated from the beginning of the 18th century and lent by AÚ SAV in Nitra was studied. The artefact was identified as wrought iron with bluing surface treatment at the edges. The metallic core of the artefact is preserved with corrosion layers on the surface identified as goethite and magnetite in macroscale and lepidocrocite in microscale. The corrosion damage corresponds to long-term corrosion in the atmosphere with low corrosivity.

Acknowledgement

This work was financially supported by a grant from the Scientific Grant Agency of the Ministry of Education, Science, Research and Sport of the Slovak Republic and the Slovak Academy of Sciences (VEGA) under the contract number VEGA 1/0792/17.

References

Bellot-Gurlet L, Neff D, Réguer S, Monnier J, Saheb M, Dillmann P (2009) Journal of Nano Research 8: 147—156.

Bernard MC, Joiret S (2009) Electrochimica Acta 54: 5199—5205.

Grousset S, Bayle M, Dauzeres A, Crusset D, Deydier V, Linard Y, Dillmann P, Mercier-Bion F, Neff D (2016) Corrosion Science 112: 264—275.

Monnier J, Guillot I, Legrand L, Dillmann P (2013) In: Dillmann P, Watkinson D, Angelini E, Adriaens A (Ed) Corrosion and conservation of cultural heritage metallic artefacts (pp. 285—310), Woodhead Publishing Limited, Cambridge.

Čambal R (2014) In: Musilová M, Barta P, Herucová A (Ed) Bratislavský hrad: dejiny, výskum a obnova. (pp 31—37). Alfa print s.r.o., Martin.

Neff D, Bellot-Gurlet L, Dillmann P, Reguer S, Legrand L (2006) Journal of Raman Spectroscopy 37: 1228—1237.

Neff D, Reguer S, Dillmann P (2013) In: Dillmann P, Watkinson D, Angelini E, Adriaens A (Ed) Corrosion and conservation of cultural heritage metallic artefacts (pp 55—57). Woodhead Publishing Limited, Cambridge.

Rocca E, Faiz H, Dillmann P, Neff D, Mirambet F (2019) Electrochimica Acta 316: 219—227.

Saheb M, Neff D, Dillmann P, Descostes M, Matthiesen H (2013) In: Dillmann P, Watkinson D, Angelini E, Adriaens A (Ed) Corrosion and conservation of cultural heritage metallic artefacts (pp 260—261). Woodhead Publishing Limited, Cambridge.

Schweitzer PA (2010) Fundamentals of Corrosion: Mechanisms, Causes, and Preventative Methods, CRC Press, USA.

Šilhová A (2011) In: Team of authors (Ed) Konzervování a restaurování kovů (pp 413—414). Gill. s.r.o., Brno.

EN ISO 9223:2012. Corrosion of metals and alloys — Corrosivity of atmospheres — Classification, determination and estimation.

Veneranda M, Aramendia J, Bellot-Gurlet L, Colomban P, Castro K, Madariaga JM (2018) Corrosion Science 133: 68—77.

http://www.bratislava-hrad.sk/historia 29. 9. 2020

sciendo

Theoretical study of lumichrome, 1-methyl-lumichrome and lumiflavin binding ability with thymine

Denisa Cagardová, Martin Michalík, Vladimír Lukeš

Institute of Physical Chemistry and Chemical Physics, Slovak University of Technology in Bratislava, Radlinského 9, SK-812 37 Bratislava, Slovakia
denisa.cagardova@stuba.sk

Abstract: Gas-phase geometry and electronic structure of lumichrome, 1-methyl-lumichrome and lumiflavin in the electronic ground state and their excited states were investigated using the Density Functional Theory. Their binding ability with thymine was estimated for model van der Waals dimers with two intermolecular hydrogen bonds. The influence of hydrogen bonds on their photophysical properties was analyzed. Obtained theoretical data were compared with available experimental absorption and fluorescence spectra.

Keywords: Chemosensor; flavins; fluorescence; hydrogen bond; vertical excited states

Introduction

Chemosensors are organic or inorganic molecules used for analyte sensing resulting in a detectable change or signal generation (Wu et al., 2017). In this context, changes in the ultraviolet and visible absorption or emission properties are evaluated. Although the fluorescence signal detection is technically more demanding, a low concentration of analytes can be observed with standard fluorescence spectrometers offering the advantage of using the sensors directly within fiber optic systems. Chemosensors can also be applied together with electrochemical methods. All these outlined techniques are suitable for monitoring of various environmental samples or determination of drug concentrations and blood content.

Chemosensors applicable in the recognition of nucleobases have attracted immense interest because of their application in DNA-binding drugs research or in medical analytical chemistry and molecular biology (White et al., 1998). One alternative approach used in the development of these chemical probes involves the use of small molecules (ligands) that are able to bind to intrahelical target bases by hydrogen bonds in DNA duplexes (Rajendran and Nair, 2006). Selective binding of these ligand molecules is promoted by a pseudo-base pairing along the nucleobase (Hagihara et al., 2004). From the thermodynamic point of view, pairing of ligands with a nucleon base target can lead to more stable structures than the Watson-Crick base pairing (Lee and Kool, 2005; Kim and Kool, 2005; Gao et al., 2005). Considering chemosensors, benzo[g]pteridine based molecules represent a perspective group. Rajendar et al. (2010) showed that lumichrome (7,8-dimethylbenzo[g]pteridine-2,4(1H,3H)-dione) and 1-methyl-lumichrome (1,7,8-trimethylbenzo[g]pteridine-2,4(3H)-dione) selectively bind to thymine over adenine, cytosine, and guanine. The authors proved visible fluorescence quenching by performing spectroscopic experiments.

Although amber molecular mechanics was applied by Rajendar et al., electron donating effects of methyl group on hydrogen bonding with thymine and on the whole electron structure have not been

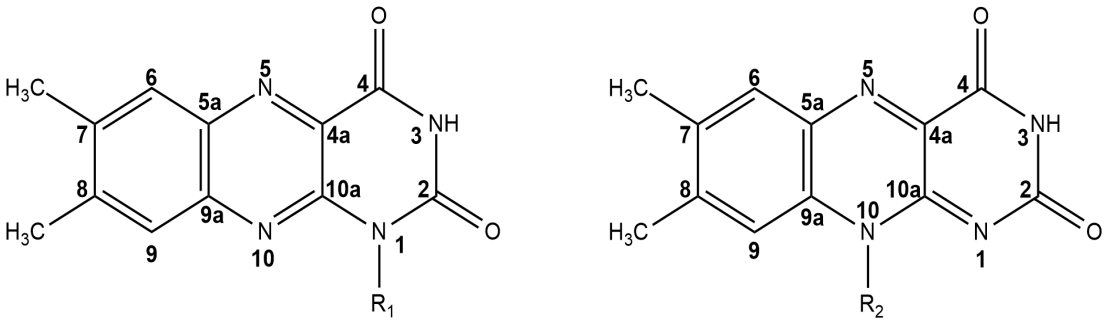

A/B
Molecule **A** (Lumichrome): $R_1 = H$
Molecule **B** (1-Methyl-lumichrome): $R_1 = CH_3$

C
Molecule **C** (Lumiflavin): $R_2 = CH_3$

Fig. 1. Schematic structure of studied molecules with atom notation.

properly analyzed. In addition, only one dimer configuration was examined. Since three more dimer patterns are possible, we decided to present a thorough computational analysis of thymine binding ability to lumichrome (7,8-dimethyl-alloxazine), 1-methyl-lumichrome and lumiflavin (Fig. 1). Partial aims of this study are: (1) to calculate optimal geometries of electroneutral monomer molecules and four model van der Waals dimers within electronic ground and lowest excited states; (2) to compare hydrogen bond lengths and interaction energies of model dimers; (3) to evaluate optical transitions contributing to the lowest energy transition in absorption and fluorescence spectra. These changes in photo-physical properties with respect to the non-interacting subsystems are discussed below.

Computational details

The Gaussian 16 program package was used to perform quantum chemical calculations (Frisch et al., 2016). Optimal geometries of the studied molecules were calculated by the Density Functional Theory (DFT) with the B3LYP hybrid functional (Lee et al., 1988; Becke, 1998) without any constraints (energy cut-off of 10^{-5} kJ mol^{-1}, final RMS energy gradient under 0.01 kJ mol^{-1} A^{-1}). The 6-31+G** basis set of atomic orbitals was applied (Hariharan and Pople, 1973; Rassolov et al., 1998). Based on the B3LYP geometries, the vertical singlet transition energies and oscillator strengths between the initial and final electronic states were computed by time-dependent TD-DFT (Furche and Ahlrichs, 2002). The TD-DFT was also used to calculate the lowest excited state geometries and de-excitation energies corresponding to the fluorescence energies. True minima on the potential energy surface were confirmed by frequencies' inspection (no imaginary frequencies).

The molecules and molecular orbitals were visualized using the Molekel (Flukiger et al., 2002) and Avogadro (Hanwell et al., 2012) program packages. Dimer interaction energies of the investigated molecule with thymine supersystem were calculated within the supermolecular approach, including the empirical dispersion corrections. The Grimme's dispersion correction with Becke-Johnson damping function (GD3BJ) (Grimme et al., 2011) was used. The Basis Set Superposition Error (BSSE) (Boys and Bernardi, 1970) was corrected using the counterpoise method (Simon et al., 1996; Xantheas, 1996).

Results and Discussion

Optimal gas-phase geometries of the studied molecules are planar like in crystal structures of their derivatives 3-methyl-lumichrome or flavinium nitrate (Norrestam and Stensland, 1972; Wouters et al., 1995). However, compared to the symmetric benzene molecule in electronic ground state (S_0), their aromaticity is slightly perturbed. The gas-phase B3LYP/6-31+G** optimal bond length in benzene is 1.398 Å. Consecutive alternation of single and double bonds can be seen for the dimethyl-substituted ring shown in Fig. 2. For the electronic ground state (S_0), differences between these bonds changed from 0.03 to 0.06 Å. The longest carbon-carbon interatomic distances were found for the **A** molecule while the shortest bonds occur in the **C** molecule. The middle ring containing N(5) and N(10) atoms in **A** and **B** molecules exhibits larger differences between the single and double carbon-carbon bonds, i.e. 0.05 to 0.09 Å. For reference, in symmetric pyrazine gas-phase B3LYP/6-31+G** molecule, the C—N distance is 1.340 Å and C—C distance is 1.398 Å. Although only one ring is aromatic, effective global π-conjugation is theoretically predicted. The shortest distance of 1.299 Å was found for the C(4a)—N(5) bond. Electronic excitation to the S_1 state can change the investigated bond lengths significantly. Maximal changes were found between the carbon and nitrogen atoms (see Fig. 2). Within supramolecular chemistry, the presence of a guest (the analyte) at the host site (the sensor) in chemosensing results in recognition signal (sensing) which can be monitored in real time. This requires the binding of the analyte to the receptor using all kinds of binding interactions such as hydrogen bonding, dipole- and electrostatic interactions, metal chelation, etc.

Potential of lumichrome derivatives as bioorganic molecular sensors was tested by examination of van der Waals-bounded (vdW) supersystems with thymine. As it was reported by Rajendar et al. (2010), methyl-substitution and benzo-annellation of lumazine to lumichrome or its derivatives increase the binding affinity significantly. Compared to alloxazine with the binding constants of 0.7×10^6 M^{-1} obtained from fluorescence titration analysis, lumichrome and lumiflavin bind to thymine with remarkably higher affinity of 16×10^6 M^{-1} and 21×10^6 M^{-1}, respectively (Sankaran et al., 2009). Moreover, the methyl group of thymine seems to increase the molecular polarizability which allows more favorable van der Waals interaction determined by the coulombic and dispersion forces. Four different dimer configurations with two intermolecular O···H hydrogen bonds are possible (Fig. 3). These can be explained by local dipolar pairs of atoms and not by global molecular static dipole moments. The supermolecular electronic interaction energies collected in Tab. 1 confirmed the thermodynamic stabil-

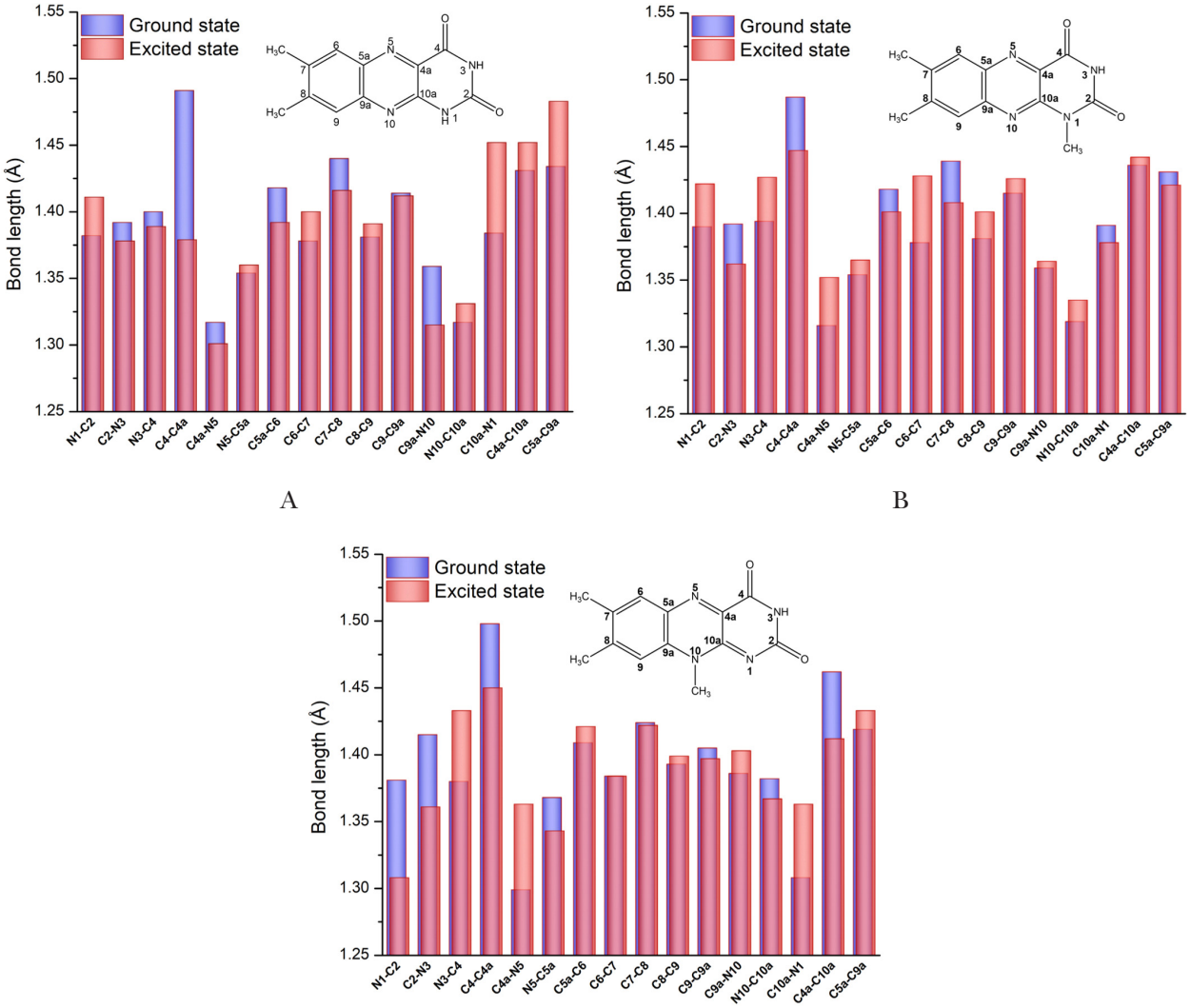

Fig. 2. B3LYP/6-31+G** optimal bond lengths (in Angströms) of electronic ground state (S_0) and the lowest excited state (S_1) in A, B and C molecules.

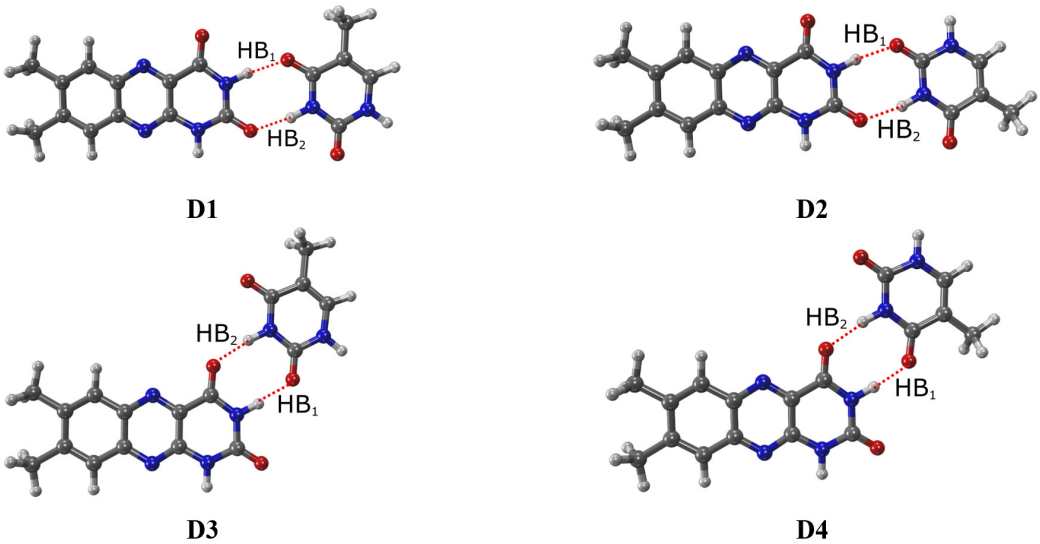

Fig. 3. Notation of relative arrangement of studied dimers and notation of hydrogen HB_1 and HB_2 bonds.

ity of all arrangements, with the longitudinal planar one (D1) being the most stable. This agrees with the recent force-field simulations of lumichrome interaction with thymine (Rajendar et al., 2010). However, energy differences between different arrangements can be considered negligible, therefore, occurrence of all the arrangements in a real sample is predicted according to the Boltzmann distribution.

When correction on BSSE is included in full geometry optimization, the interaction energy is slightly increased by up to 1.8 kJ mol^{-1}. Otherwise, the trends in evaluated interaction energies are comparable (Tab. 1). Dimer stability is also directly influenced by hydrogen bond lengths (see notation in Fig. 3). The length of intermolecular hydrogen bond HB_1 increases concurrently with the decreasing HB_2 length (Tab. 2). It is obvious that shorter hydrogen bond lengths stabilize the supersystem resulting in a more negative interaction energy. The most stable dimer configuration is D1 with optimal methyl group orientation while D4 is slightly less stable. In case of lumiflavin, D2 is energetically more favorable than D4.

The application of chemosensors is a form of molecular recognition. Usually, the change (signal) during chemosensing is observed by measuring various physical properties of the chemosensor, such as the photophysical properties demonstrated in absorption or emission. Signaling is often optically based on electromagnetic radiation which causes changes in either (or both) the ultraviolet and visible absorption or the emission properties of the sensors. Moreover, electronic structure and its connection with the chemical modification can be described in terms of vertical transitions. Comparison of the energies for singlet states of the studied non-interacting monomers and model dimers is listed in Tab. 3.

Lumichrome (**A**) energy of the first excited vertical singlet state (S_1) over the electronic ground state is 3.39 eV (366 nm) and it is assigned to the HOMO to LUMO transition. However, B3LYP also predicts the third (HOMO–1→LUMO) transition with significant absorption probability (86 %) and the oscillator strength of 0.22, which corresponds with experimental optical absorption at 3.50 eV (354 nm) (Sheraz et al., 2014; Maity et al., 2015, Sikorski et al., 2001). Slightly increased aromaticity of the keto-groups bearing ring in molecules **B** and **C** probably leads to the bathochromic shifts of the lowest energy transitions. Excitation energy of the $S_0 \rightarrow S_1$ optical transition is 3.00 eV (413 nm)

Tab. 1. Supermolecular interaction energies of vdW dimers in S_0 state obtained for fully optimized geometries (*IE*) and geometries optimized with correction on BSSE (IE_{BSSE}). Values are in kJ mol^{-1}.

Dimers	D1		D2		D3		D4	
Molecule	*IE*	IE_{BSSE}	*IE*	IE_{BSSE}	*IE*	IE_{BSSE}	*IE*	IE_{BSSE}
A	–59.0	–60.5	–57.1	–58.3	–56.9	–58.2	–58.7	–60.5
B	–58.5	–59.6	–56.7	–57.8	–56.2	–57.7	–58.2	–60.0
C	–58.1	–60.0	–56.2	–57.8	–53.0	–53.9	–54.5	–55.7

Tab. 2. Hydrogen bond lengths HB_1 and HB_2 (in Å) of vdW dimers in S_0 state obtained for fully optimized geometries and geometries optimized with correction on BSSE. Values in parentheses stand for the hydrogen bond lengths in optimized S_1 state of dimers.

System	without correction		BSSE correction	
Molecule-Dimer	HB1	HB2	HB1	HB2
A-D1	1.788 (1.802)	1.827 (1.840)	1.800	1.841
A-D2	1.804 (1.785)	1.842 (1.826)	1.817	1.856
A-D3	1.795 (1.788)	1.848 (1.761)	1.808	1.862
A-D4	1.778 (1.806)	1.833 (1.775)	1.790	1.847
B-D1	1.798 (1.841)	1.813 (1.823)	1.810	1.826
B-D2	1.814 (1.836)	1.827 (1.857)	1.828	1.841
B-D3	1.804 (1.805)	1.840 (1.769)	1.817	1.853
B-D4	1.787 (1.785)	1.825 (1.755)	1.799	1.838
C-D1	1.815 (1.833)	1.787 (1.816)	1.827	1.798
C-D2	1.831 (1.832)	1.802 (1.847)	1.845	1.813
C-D3	1.846 (1.752)	1.830 (1.824)	1.862	1.843
C-D4	1.831 (1.732)	1.816 (1.807)	1.845	1.829

Tab. 3. Selected TD-B3LYP/6-31+G** lowest energy singlet ($S_0 \rightarrow S_n$) transition energies E (in eV), wavelengths λ (in nm) and the corresponding oscillator strengths f.

System	n	E	λ	f	System	n	E	λ	f	System	n	E	λ	f
A	1	3.39	366	0.06	**B**	1	3.36	369	0.20	**C**	1	2.99	415	0.20
	2	3.44	360	0.00		2	3.42	363	0.00		2	3.14	395	0.00
	3	3.86	322	0.22		3	3.85	322	0.19		3	3.31	375	0.00
	4	3.97	312	0.00		4	3.94	315	0.00		4	3.79	327	0.15
A-D1	1	3.40	364	0.00	**B-D1**	1	3.38	367	0.00	**C-D1**	1	3.03	410	0.24
	2	3.44	361	0.08		2	3.41	363	0.10		2	3.03	409	0.00
A-D2	1	3.41	364	0.00		3	3.78	328	0.00		3	3.07	404	0.00
	2	3.43	361	0.08	**B-D2**	1	3.38	366	0.00	**C-D2**	1	3.03	410	0.24
A-D3	1	3.35	370	0.08		2	3.41	364	0.10		2	3.07	404	0.00
	2	3.45	359	0.00		3	3.80	327	0.00		3	3.16	393	0.00
A-D4	1	3.35	370	0.08	**B-D3**	1	3.32	374	0.10	**C-D3**	1	2.95	420	0.22
	2	3.45	360	0.00		2	3.43	362	0.00		2	3.17	391	0.00
						3	3.67	338	0.00		3	3.18	390	0.00
					B-D4	1	3.27	379	0.10	**C-D4**	1	2.95	421	0.22
						2	3.42	363	0.00		2	3.15	393	0.00
						3	3.64	341	0.00		3	3.16	392	0.00

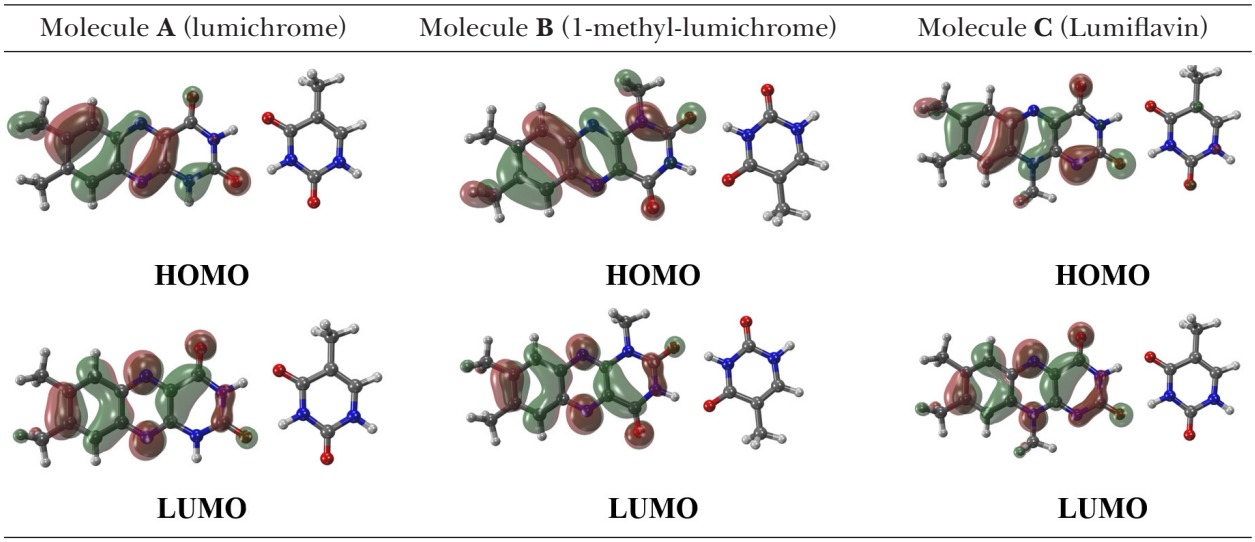

Fig. 4. Shapes of B3LYP/6-31+G** selected molecular orbitals of model D1 dimer for thymine and studied molecules. Depicted iso-surface value is 0.025 a.u.

and 2.99 eV (415 nm) for **B** and **C**, respectively, indicating methyl groups attached to the N(1) or N(10) atoms to increase the first transition oscillator strength up to 0.20 (compare lumichrome **A** with **B** and **C**). Experimental absorption bands at 368 nm and 441 nm for lumiflavin **C** in aqueous solution were measured by Sheraz et al. (2014). It seems that the corresponding theoretical values with significant oscillator strengths are 3.79 eV (327 nm) and 2.99 eV (415 nm), respectively.

Interestingly, bonding with thymine causes a negligible shift of vertical $S_0 \rightarrow S_1$ transition energies. Red shift up to 0.04 eV was found for D1 and D2 supersystems and blue shift up to 0.09 eV for the D3 and D4 ones. Also, in case of D1 and D2 dimer configurations containing **A** and **B** molecules, HOMO→LUMO transition is the second $S_0 \rightarrow S_2$ transition with higher oscillator strength while in other supersystems it corresponds to the first vertical excitation. The first vertical $S_0 \rightarrow S_1$ transition in these four cases (**A-D1/D2**, **B-D1/D2**) match the HOMO–3→LUMO transition.

Graphical frontier molecular orbitals analysis in Fig. 4 shows negligible contribution of the thymine molecule. HOMO electrons are uniformly delocalized over the longest axial direction. Similarity

Tab. 4. Selected vertical TD-B3LYP/6-31+G** de-excitation ($S_1 \rightarrow S_0$) energies E (in eV), wavelengths λ (in nm) and oscillator strengths f estimated for the lowest excited singlet states.

System	E (λ)	f	System	E (λ)	f	System	E (λ)	f
A	2.77 (448)	0.00	**B**	2.89 (430)	0.05	**C**	1.95 (637)	0.00
A-D1	2.79 (444)	0.00	**B-D1**	2.95 (421)	0.06	**C-D1**	2.54 (488)	0.18
A-D2	2.79 (444)	0.00	**B-D2**	2.94 (422)	0.06	**C-D2**	2.53 (490)	0.17
A-D3	2.85 (436)	0.05	**B-D3**	2.84 (436)	0.06	**C-D3**	1.81 (684)	0.00
A-D4	2.85 (436)	0.05	**B-D4**	2.84 (437)	0.06	**C-D4**	1.80 (688)	0.00

between the shapes of the orbitals in dimers and non-interacting monomers suggests minimal effect on the chromophore confirming small differences in vertical transitions. The thymine molecule does not contribute with its own electrons to these excitations.

Moreover, transition from the S_0 state to the first excited state is related to the significant change in hydrogen bond lengths for the D1 dimer (Tab. 2). Rajendar et al. (2010) found fluorescence peak broadening after mixing lumichrome and 1-methyl-lumichrome with thymine. Indeed, the $S_1 \rightarrow S_0$ de-excitation energies of D1 and D2 dimers show small blue shifts compared to the non-interacting molecules (Tab. 4). Therefore, pairing with thymine is expected to provide a visible change in the fluorescence spectra. The increase of fluorescence oscillator strength up to 0.17 is predicted for **C-D1** and **C-D2** dimers. Despite higher oscillator strength prediction, the theoretical TD-CAM-B3LYP de-excitation energies were not included because of significant energy overestimation. According to experimental data measured by Rajendar et al. (2010), fluorescence maximum of free-of-DNA lumichrome **A** is at 476 nm (2.60) with three-times higher fluorescence intensity than in the supersystem with thymine (**A-D1**). Position of the peak for the supersystem is negligibly shifted to 473 nm (2.62 eV). The shift agrees well with theoretical values in the present study; however, the TD-B3LYP method overestimates the de-excitation energies. In case of 1-methyl-lumichrome **B**, maxima were observed at 474 nm and 473 nm (2.62 eV) for the free-of-DNA form and **B** binding to thymine, respectively. This also agrees well with the experimental value of 475 nm measured for both lumichrome **A** and 1-methyl-lumichrome **B** in aqueous solution by Sikorski et al. (2001). They have also shown that lumiflavin **C** exhibits fluorescence maximum at about 530 nm.

Conclusion

Optimal geometries and electronic structure of lumichrome, 1-methyl-lumichrome and lumiflavin in the electronic ground state and in the lowest excited states were theoretically studied. Compared with the reference lumichrome, the addition of electron donating methyl groups to the N(1) or N(10) position had a significant effect on the bond lengths in the benzo[g]pteridine backbone. The lowest predicted vertical excitation energy for lumichrome is 3.39 eV whereas these energies for **B** and **C** molecules are red shifted. These vertical electronic excitation energies correspond to the HOMO to LUMO transition of the π-type character. Two stable intermolecular hydrogen bonds with thymine were confirmed by the theoretical calculations of interaction energies of four model van der Waals complexes. For all the studied dimers, optical transitions with sufficient oscillator strengths corresponding to the HOMO→LUMO transition are predicted. Only small blue shifts of de-excitation energies in the fluorescence spectra of the supersystems were found compared with the monomers. Even though the used quantum mechanical approaches have limitations, the obtained theoretical trends in the (de-)excitation energies correspond well with experimental observations. Thus, theoretical analysis could help in chemosensors modeling and identification of new organic candidates for chemosensing. The studied molecules can be used as chemosensors in DNA due to its high binding ability and formation of stable van der Waals dimers with thymine.

Acknowledgement

The work has been supported by Slovak Research and Development Agency (APVV-15-0053) and VEGA 1/0504/20. We are grateful to the HPC center at the Slovak University of Technology in Bratislava, which is a part of the Slovak Infrastructure of High Performance Computing (SIVVP project, ITMS code 26230120002, funded by the European region development funds, ERDF) for the computational time and resources made available. D.C. would like to thank for support from the STU Grant scheme for Support of Young Researchers (1848).

References

Becke AD (1998) Phys Rev A 38(6): 3098—3100.

Boys SF, Bernardi F (1970) Mol. Phys. 19: 553—566.

Flukiger P, Luthi HP, Sortmann S, Weber J (2002) Molekel 4.3, Swiss National Supercomputing Centre, Manno, Switzerland.

Frisch MJ, Trucks GW, Schlegel HB, Scuseria GE, Robb MA, Cheeseman JR, Scalmani G, Barone V, Petersson GA, Nakatsuji H, Li X, Caricato M, Marenich AV, Bloino J, Janesko BG, Gomperts R, Mennucci B, Hratchian HP, Ortiz JV, Izmaylov AF, Sonnenberg JL, Williams-Young D, Ding F, Lipparini F, Egidi F, Goings J, Peng B, Petrone A, Henderson T, Ranasinghe D, Zakrzewski VG, Gao J, Rega N, Zheng G, Liang W, Hada M, Ehara M, Toyota K, Fukuda R, Hasegawa J, Ishida M, Nakajima T, Honda Y, Kitao O, Nakai H, Vreven T, Throssell K, Montgomery JA Jr., Peralta JE, Ogliaro F, Bearpark MJ, Heyd JJ, Brothers EN, Kudin KN, Staroverov VN, Keith TA, Kobayashi R, Normand J, Raghavachari K, Rendell AP, Burant JC, Iyengar SS, Tomasi J, Cossi M, Millam JM, Klene M, Adamo C, Cammi R, Ochterski JW, Martin RL, Morokuma K, Farkas O, Foresman JB, Fox DJ (2016) Gaussian 16, Revision B.01, Gaussian, Inc., Wallingford CT.

Furche F, Ahlrichs R (2002) J Chem Phys. 117(16): 7433.

Gao J, Liu H, Kool ET (2005) Angew. Chem. Int. Ed. 44: 3118—3122.

Grimme S, Ehrlich S, Goerigk L (2011) J. Comput. Chem. 32: 1456—1465.

Hagihara S, Kumasawa H, Goto Y, Hayashi G, Kobori A, Saito I, Nakatani K (2004) Nucleic Acids Res. 32: 278—286.

Hanwell MD, Curtis DE, Lonie DC, Vandermeersch T, Zurek E, Hutchison GR (2012) J Cheminform. 4(1): 17.

Hariharan PC, Pople JA (1973) Theor. Chim. Acta. 28(3): 213—222.

Kim TW, Kool ET (2005) J. Org. Chem. 70: 2048—2053.

Lee AH, Kool ET (2005) J. Am. Chem. Soc. 127: 3332—3338.

Lee C, Yang W, Parr RG (1988) Phys Rev B. 37(2): 785—789.

Maity B, Chatterjee A, Seth D (2015) RSC Adv. 5: 3814—3824.

Norrestam R, Stensland B (1972) Acta Crystallographica B: Struct. Crystallogr. Cryst. Chem., 28: 440.

Raibenspies JH, Guo F, Rizzo CJ (2000) Org. Lett. 2(7): 903—906.

Rajendar B, Rajendran A, Ye Z, Kanai E, Sato Y, Nishizawa S, Sikorski M, Teramae N (2010) Org. Biomol. Chem. 8: 4949—4959.

Rajendran A, Nair BU (2006) Biochim. Biophys. Acta 1760: 1794—1801.

Rassolov VA, Pople JA, Ratner MA, Windus TL (1998) J Chem Phys. 109(4): 1223—1229.

Sankaran NB, Sato Y, Sato F, Rajendar B, Morita K, Seino T, Nishizawa S, Teramae N (2009) J. Phys. Chem. B 113: 1522—1529.

Sheraz MA, Kazi SH, Ahmed S, Qadeer K, Khan MF, Ahmad I (2014) Cent. Eur. J. Chem. 12(6): 635—642.

Sikorski M, Sikorska E, Koziolowa A, Gonzalez Moreno R, Bourdelande JL, Steer RP, Wilkinson F (2001) J. Photochem. Photobiol. B 60: 114—119.

Simon S, Duran M, Dannenberg JJ (1996) J. Chem. Phys. 105: 11024—11031.

White S, Szewczyk JW, Turner JM, Baird EE, Dervan PB (1998) Nature 391: 468—471.

Wouters J, Evrard G, Durant F (1995) Acta Cryst. C51: 1223—1227.

Wu D, Sedgwick AC, Gunnlaugsson T, Akkaya EU, Yoon J, James TD (2017) Chem. Soc. Rev. 46(23): 7105—7123.

Xantheas SS (1996) J. Chem. Phys. 104: 8821—882.

sciendo

Effect of ambient parameters change on mint leaves solar drying

Abdul Wasim Noori[1, 2], Mohammad Jafar Royen[1, 2], Juma Haydary[1]

[1]*Institute of Chemical and Environmental Engineering, Slovak University of Technology in Bratislava, Radlinského 9, 81237 Bratislava, Slovakia, juma.haydary@stuba.sk*
[2]*Faculty of Chemical Technology, Kabul Polytechnic University, Kart-e Mamoorin, Kabul, Afghanistan awnoori@kpu.edu.af*

Abstract: This study investigates the effect of ambient conditions change on mint leaves solar drying performance and product water activity. Two drying methods, active indirect solar drying (AISD) and open sun drying (OSD) were compared while the experiments were carried out at specific dry climate conditions. During the experimental days, temperature varied from 20 to 30 °C, air relative humidity from 14 to 28.8 % and ambient pressure was around 82 kPa. The effect of air relative humidity change during the day on the rehydration of the product during the drying process was observed. After 7 h of drying, moisture content of mint leaves decreased from 85.29 % to 5.38 % in the AISD and 7.42 % in the OSD system. The 0.97 initial water activity decreased to 0.195 in AISD and 0.79 in OSD. Rehydration during the evening hours caused an increase in product water activity from 0.2 to 0.51. Changes of ambient conditions such as temperature and air relative humidity during the day can significantly affect water activity of dried product due to its rehydration and thus increase the risk of product spoilage.

Keywords: drying, mint, rehydration, solar dryers, sun drying

Introduction

One of the major problems in the world today is how to preserve seasonal agricultural crops, especially fruits and vegetables for a long time. Most of these products are exposed to spoilage. The percentage of spoiled products is not only related to the way they are harvested, stored, and used, but 10 % to 40 % spoilage of fresh fruit and vegetables is related to their water content (more than 80 %) (Maker Associates Limited (MMA), 2008; Joardder, 2016). To prevent these valuable products from being spoiled, their shelf life has to be increased.

Mint (*Mentha spicata L*), a leafy vegetable of the large family of *Labiatae*, has shorter shelf-life than many other agricultural products (Doymaz, 2006). Most people around the world are familiar with using fresh or dried leaves and mint leaf oil. This valuable herb has culinary, medicinal and flavoring properties and is one of the aromatic herbs (fragrant herbs) (Akpinar, 2010) widely used in pesticides, food production and cosmetics due to its properties (Eltawil et al., 2018).

Mint is also one of the most important vegetables produced in Afghanistan where this research was done. Afghanistan is a developing country whose economy is based on agriculture and livestock. It is geographically located in Central Asia and it is a landlocked highland country. Most areas of the country have high altitude above the sea level, including the country's capital Kabul, which is located 1800 meters above the sea level. Due to its geographical location, Afghanistan has dry climate with high summer temperatures, low humidity and low pressure (Palka, 2001; Heuring, 2010; USAID Afghanistan, 2011). Afghanistan, with more than 300 sunny days per year, has high potential for solar energy applications. In average, solar irradiation from 4 to 6.5 kWh/m^2 /day is available (Jahangiri et al., 2019). These conditions indicate that the climate of the country is suitable for solar drying of agricultural products (Bhardwaj et al., 2012) as well as for cultivation and drying of mint as a valuable herb (Amini & Hamdam, 2017).

Shelf-life of fresh leafy vegetables (mint) after harvesting is not so long and thus they are often stored in dry state (Aktaş et al., 2017). Drying is not only considered essential for increasing shelf-life of fresh products but also for substantial reduction in volume, weight, packaging, storage, and transportation cost as well as for the increase in agricultural productivity. In practice, drying eliminates water from mint leaves and increases the resistance of dried mint leaves against microbiological degradation to ensure longer shelf-life (Ekechukwu & Norton, 1999). However, drying is an energy extensive and relatively time-consuming process. In addition, the loss of some quality parameters of the fresh products during drying is considered as a disadvantage. Beside the conventional convective drying method, different alternative methods have been developed; for example: spray drying (Sormoli & Langrish, 2016), freeze drying (Kudra & Mujumdar, 2009), microwave drying (Sagar &

Kumar 2010), osmotic drying (Karam et al., 2016), vacuum drying (Wang, 2016), ultrasound drying (Mulet et al., 2003) and solar drying methods such as open sun drying OSD (Akpinar, 2010), or cabinet solar drying (CSD) (Mohamed et al., 2008). Supplying power required for drying is one of the fundamental problems in the drying process which constitutes the basic economics of the drying process. Solar drying of agricultural crops is the simplest and cheapest way to preserve such products. OSD has been known and used for centuries to dry meat, cereals, fruits, vegetables, etc.

Developing or underdeveloped countries such as Afghanistan still use OSD to dry meat and all kinds of agricultural products. Utilization of OSD is common as it is easy to use, inexpensive, and the energy source is accessible anywhere. Main focus today is on drying processes using renewable sources, especially solar energy. For vegetables (mint) drying, two basic solar drying methods are applied: OSD and CSD (Demissie et al., 2019; Babu et al., 2018). OSD is the simplest and cheapest way of mint leaves drying as it does not require capital costs for equipment preparation, but longer drying time and bigger area for sample spreading are needed. In this method, quality of the dried product is not high, and its contamination is very likely; also, the solar radiation intensity during the drying process cannot be controlled (Saleh & Badran, 2009). The CSD system is a good alternative for mint drying instead of the OSD system. CSD requires some investment costs for device preparation; the amount of invested capital is low considering the device utilization. CSD decreases the drying time and drying surface, increases the quality of dried products, and includes solar radiation intensity controlling facilities (Zambrano et al., 2019). Various types of CSD are available, including direct, indirect, and mixed models with forced and natural convection of airflow (Mustayen et al., 2014). During the last decades, OSD and CSD systems have been studied by many researchers. Different aspects of the OSD system have been studied (Jain & Pathare, 2007; Akpinar, 2006; Toğrul & Pehlivan, 2004; Swami et al., 2006; Kingsly et al., 2007; Anwar & Tiwari, 2001; Jain & Tiwari, 2003). CSD includes passive systems such as direct natural airflow solar dryer (DNASD) or indirect natural airflow solar dryer (INASD), and active systems with forced air flow such as indirect active solar dryer (IASD) (Islam et al., 2019; Vijayan et al., 2020; Petros et al., 2019; Hatami et al., 2020; César et al., 2020; Lakshmi et al., 2019).

Open sun drying and cabinet solar drying were compared in various studies. Grapes drying was faster in DNASD and TGSD than in OSD (Fadhel et al., 2005). Akpinar et al. (2006) developed and compared mathematical models for parsley leaves drying in convective and OSD dryers. It can be concluded that higher drying rate considering the experiment time is achieved in the convective system than in OSD. The results also show that the drying rate is directly related to the heated air temperature. Tunde-Akintunde (2011), compared DNASD and OSD for chili drying. Consequently, his research showed that application of osmotic solutions can increase the drying rate, which is much higher in DIASD than in OSD. Essalhi et al. (2018) compared an indirect natural airflow convective solar dryer (INACSD) and OSD for grapes drying achieving a 60 % decrease in the grapes drying time in INACSD compared to OSD, which was related to the increased air temperature in the INACSD system. They also recorded ambient parameters changes during the night (humidity increase and ambient temperature decrease). Purohit et al. (2006) investigated the economics of CSD versus OSD system finding that, although drying in CSD requires small investment costs, it is more economically effective than the OSD system. Akpinar, (2010), analyzed and evaluated mint leaves drying mathematical models for AISD and OSD systems concluding that the temporal effects of AISD are more significant than those of OSD and stating that the quality of the AISD dried product is higher than that of the OSD dried product. Generally, researchers have shown that drying in a CSD requires a shorter time and smaller space than OSD drying. In addition, products dried in CSD have better quality and economics than OSD dried products.

Despite the wide publication activity dealing with solar drying, limitations of solar drying systems have not been studied as extensively. Solar irradiation during the day is not constant and thus the drying conditions change during the process, e.g. temperature and air relative humidity. These factors affect the solar drying process, especially the product rehydration due to increased air humidity. Except for the paper by Essalhi et al. (2018), no literature sources provide an analysis of the effect of ambient conditions change during the day on solar drying performance. Particularly, product water activity during the whole period of solar drying is very important to be monitored as temperature decrease and relative air humidity increase can lead to the rehydration of the product and an increase in its water activity.

The main purpose of this paper was to evaluate the effect of ambient conditions changes during the day on the actual drying characteristics of mint leaves in both OSD and AISD systems. Change of the water activity as a result of dried product rehydration during the process was monitored. In addition, the drying

time and final product quality were compared for both AISD and OSD systems. In this study, qualitative evaluation of dried products in both methods was also performed by a statistic survey.

Materials and Methods

Sample preparation

Branches of fresh mint were purchased from a local market in Kabul, Afghanistan. The leaves were removed from the stems, weighted and washed with tap water. The samples were placed onto a tray and in a plastic basket; the tray was placed into the AISD and the basket was exposed to the sunlight for the OSD experiment. For each experimental run, 270 g of fresh mint leaves were placed in the AISD tray and the same amount in the OSD basket. The initial height (thickness) of fresh mint leaves layer was 5 cm. Fresh mint leaves were weighed on a precise digital scale with the capacity to weight material from 0.01 to 500 g with the precision of 0.01 g.

AISD system

The active indirect solar drying (AISD) system used is a renewable energy independent system consisting of three essential parts: dryer chamber, solar collector and photovoltaic solar panel for centrifugal air blower and exhaust fan power supply (Noori et al., 2019). Outer dimensions of the wooden rectangular drying chamber are 120 × 60 × 40 cm. To achieve bigger heat exchange surface area, the drying chamber includes four metal mesh trays placed 15 cm from each other. The chamber has the capacity of 1000 g of mint leaves in one run. Outer dimensions of the flat solar collector are 150 × 60 × 10 cm with a 0.9 m^2 surface area. The main component of the collector is a 10.5 m long helix shape aluminum pipe with a rectangular cross-section of 5.5 × 3.5 cm. The pipe surface is coated with a non-reflective and sun-absorbing black color layer. To increase air velocity, a DC centrifugal air blower in the collector inlet and a DC exhaust fan at the top of the drying chamber were installed. A 240 watts photovoltaic (PV) solar panel was used to supply power to the centrifugal air blower and exhaust (Fig. 1).

To measure controllable parameters in the device and drying environment, three types of digital data logger instruments were used. Temperature in the device was determined by a Testo 176T4 data logger measuring temperature in four different positions. To determine temperature, humidity, and pressure of ambient air outside and inside the dryer, a Testo 176P1 data logger with an integrated sensor for precise measurement of absolute pressure in the range from 600 mbar up to 1,100 mbar was used. Air velocity was measured by a Testo 405 thermal anemometer, which measures air velocity up to 10 m/s. All these instruments are produced by Testo SE & Co. KGaA.

OSD system

In this experiment, samples were placed in a plastic basket with the inner dimensions of 50 × 35 × 10 cm and exposed to direct sun radiation and climate conditions considering the same sample thickness as in the AISD device. The experiments were done at the end of March on sunny days from 9:15 am to 6:15 pm when ambient temperature varied between 20 and 30 °C and average air velocity was 2.2 m/s.

Experimental procedure

In the first step, the chamber with sample trays and baskets was washed with tap water and the collector and solar panel surface were cleaned. In the second step, initial moisture content and initial water activity of mint leaves were measured. The moisture content of mint leaves was measured with an analytical moisture analyzer (VWR MBT160 moisture analyzer, VWR International, Italy capacity: 0.001—160 g). The water activity measurements were provided by a water activity analyzer (LABTOUCH — aw SET ADVANCED, Novasina AG, Switzerland).

After placing the weighed first sample in the AISD, the second sample was placed close to the AISD and exposed to sunlight for the OSD process. By turning on the AISD system blower and exhaust fan, the drying process started as well. During sampling (every hour from the beginning up to the end of the drying process), all parameters such as temperature (ambient, collector outlet, chamber outlet), pressure (ambient), humidity (ambient, collector outlet, chamber outlet), samples weight (for AISD and OSD samples), water activity (for AISD and OSD samples), moisture content (for AISD and OSD samples), and air velocity in the chamber inlet stream (5.08 cm Ø — pipe) were recorded for each sample. Each drying experiment was repeated two times but results of both series of measurements are presented separately because of different weather conditions during the experiments. In case of water activity measurement, two parallel measurements were performed, the measurement was done in triplicate if the relative deviation between two measurements was more than 5 %.

Water sorption from ambient air experiments

Dried samples were ground to powder; 2.1 g of dried mint powder was placed in 8.5 cm Ø — petri dishes to create a layer with 1 mm thickness and the samples were stored in a box with the average

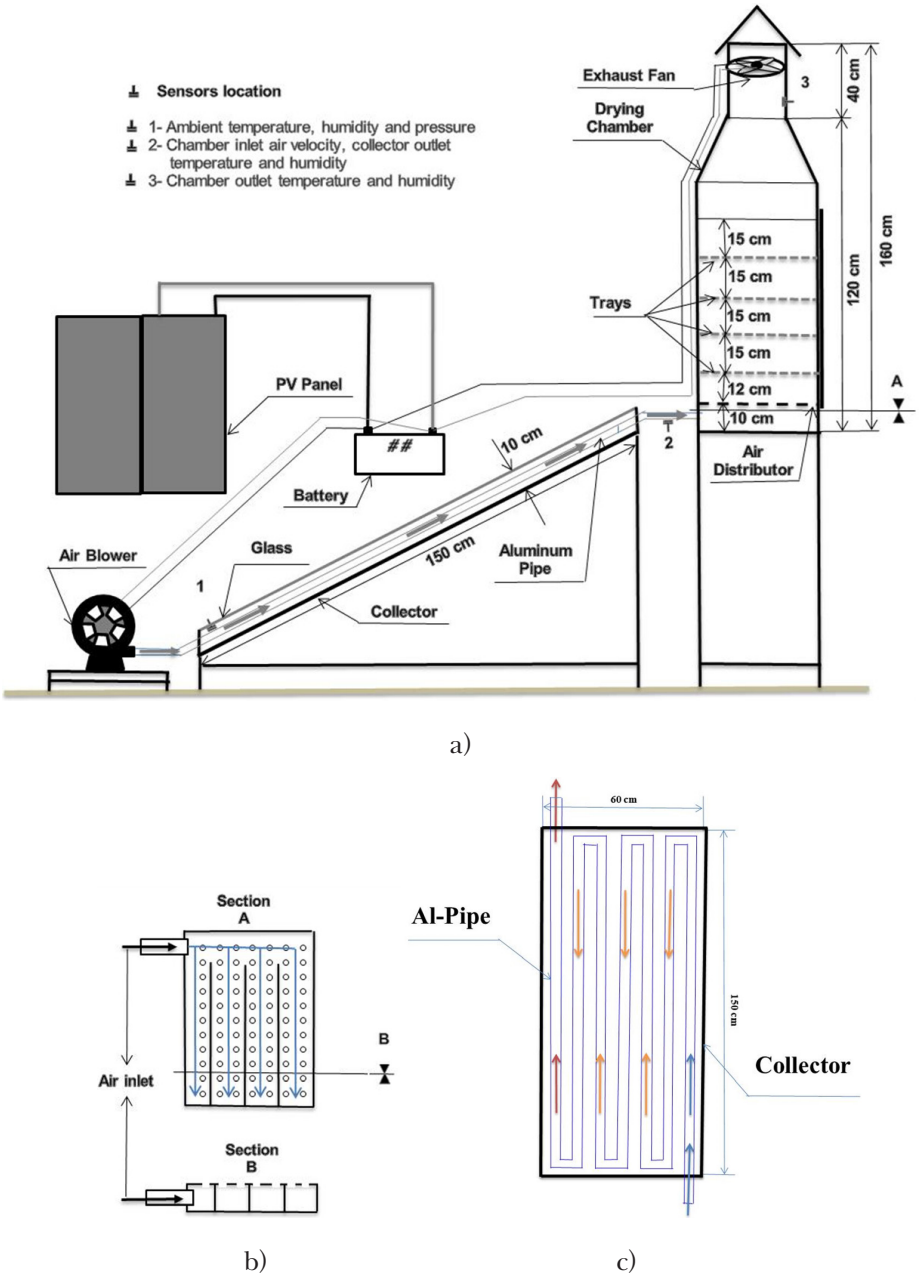

Fig. 1. Schematic description of the AISD system (a — device scheme, b — air distributor, c — collector scheme).

temperature of 29.6 °C, relative humidity of 22.8 % and pressure of 81.1 kPa for six days. In order to accurately evaluate the effect of ambient conditions on dried product rehydration, temperature, humidity and pressure in the box were recorded by Testo 176P1 digital data logger three times per day during all six days of the storage time. In addition, water activity and moisture content of each sample were determined daily.

Survey on dried products quality

Samples dried by the OSD and AISD systems were marked anonymously and provided to 120 respondents to compare and evaluate their color, taste, and odor. Preservation of the original green color is one of the quality parameters of dried mint leaves in visual appearance, which can affect the immediate decision of the consumer to accept or reject the product. Mint leaves have a typical minty flavor profile, preservation of represents another important quality factor. All 120 survey participants were in the age range of 18 to 60 years. The question to the respondents was: Which sample has better color? odor? and taste?

Results and discussion

Effect of ambient parameters changes

To increase the drying rate of the process, air temperature has to be increased which was ensured by

the solar collector in the AISD system. Influence of the collector on drying temperature can be seen clearly in Fig. 2. In this experiment, temperature was monitored at three basic points: collector inlet (ambient), collector outlet (chamber inlet) and at the outlet of the drying chamber. The ambient temperature varied from 20 to 30 °C with a maximum at the midday. During the experiment, the temperature difference between the collector inlet and outlet increased from 11.8 °C to 28.5 °C when the maximum temperature (58.5 °C) was reached at midday when the sunlight angle was perpendicular to the collector surface; the lowest temperature difference (only 2.8 °C) was recorded at the end of working time when the sun was on the horizon. During the working time, the temperature at the drying chamber outlet was always lower than at the collector output and it is higher than the ambient temperature. Only at the initial points is the chamber outlet temperature lower than the ambient one due to the high amount of water in mint leaves and free surface evaporation effect. After hot air passes through the drying chamber, some of its heat was transferred to the sample to evaporate water from fresh mint leaves. As a result, the air temperature decreased.

The air relative humidity (Fig. 3) shows exactly the reversed behavior compared to temperature (Fig. 2). During the working hours, ambient humidity fluctuated between 14 % and 28.4 %. The minimum air humidity was recorded at noon when the ambient temperature was maximal. The humidity curve illustrates that air humidity at the beginning of the experiment in the outlet stream of the drying chamber is higher than ambient air humidity, which is also related to the free surface evaporation in fresh mint leaves. However, at the end of the drying process, humidity at all three points was approximately the same.

Fig. 4 shows the sample residue mass versus working time for both drying methods. In the AISD system, the time to achieve minimum residue mass

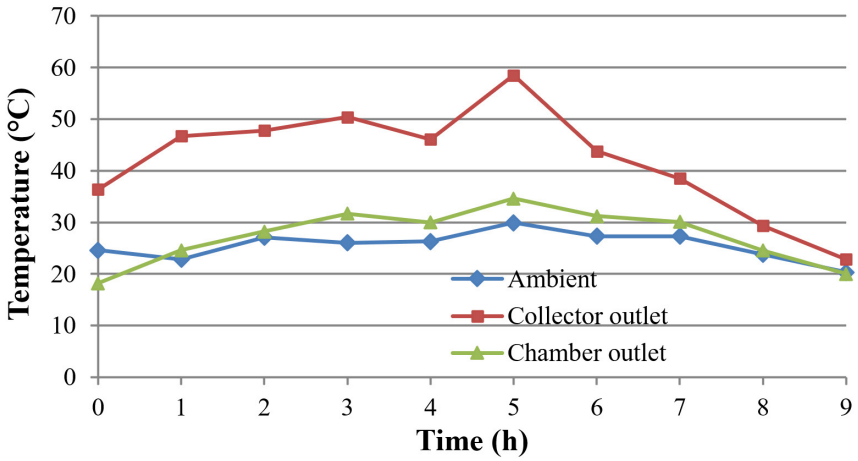

Fig. 2. Time-dependent change of ambient, collector outlet and chamber outlet temperature.

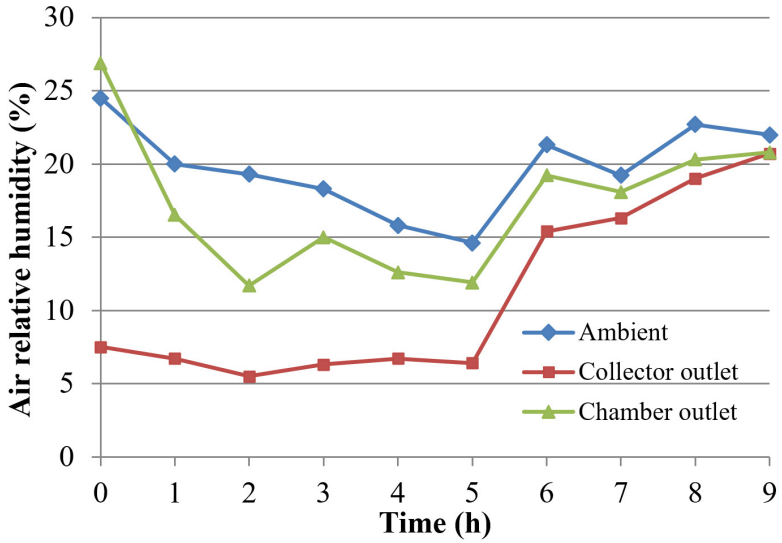

Fig. 3. Time-dependent change of ambient, collector outlet and chamber outlet humidity.

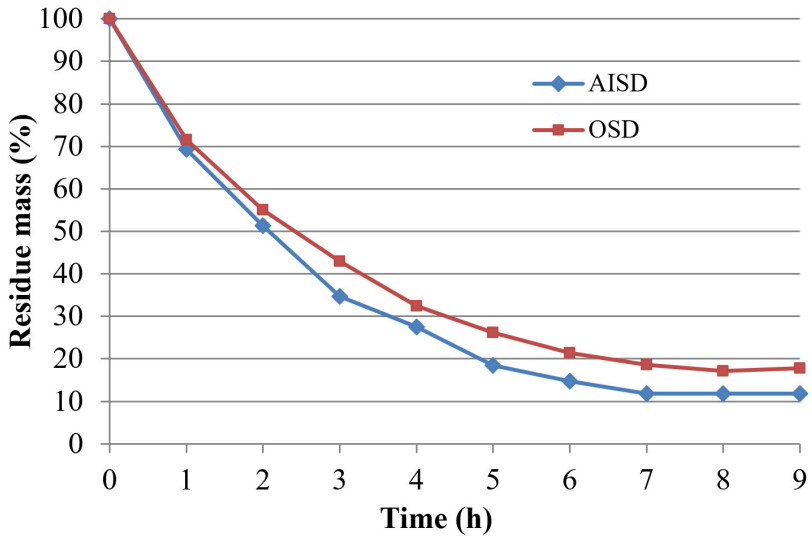

Fig. 4. Variation of sample residue mass as a function of drying time (h).

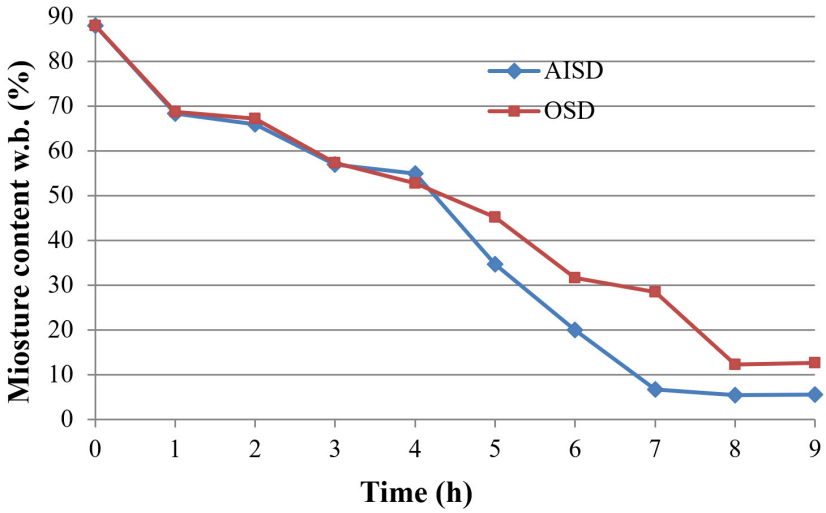

Fig. 5. Variation of moisture content (%) as a function of drying time (h).

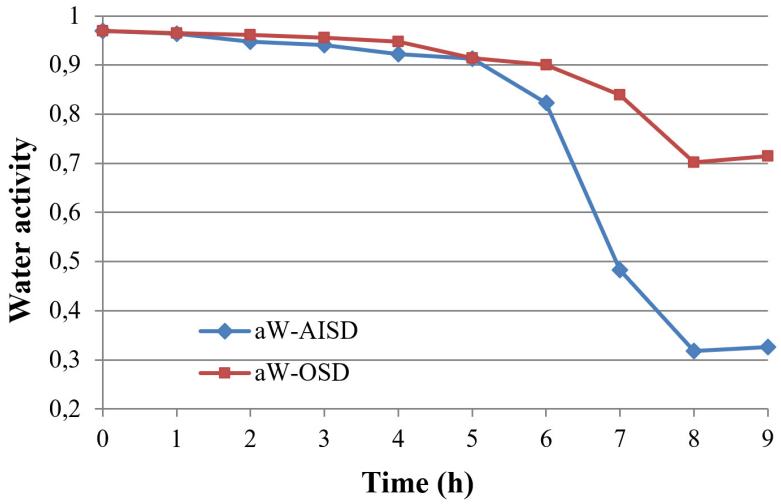

Fig. 6. Variation of water activity (aW) as a function of drying time (h).

is much shorter than in the OSD system. Due to the difference in temperature in these two systems and the consequent difference of air relative humidity, the equilibrium moisture content of dried material also differs. Thus, to achieve the same final moisture content was impossible in either

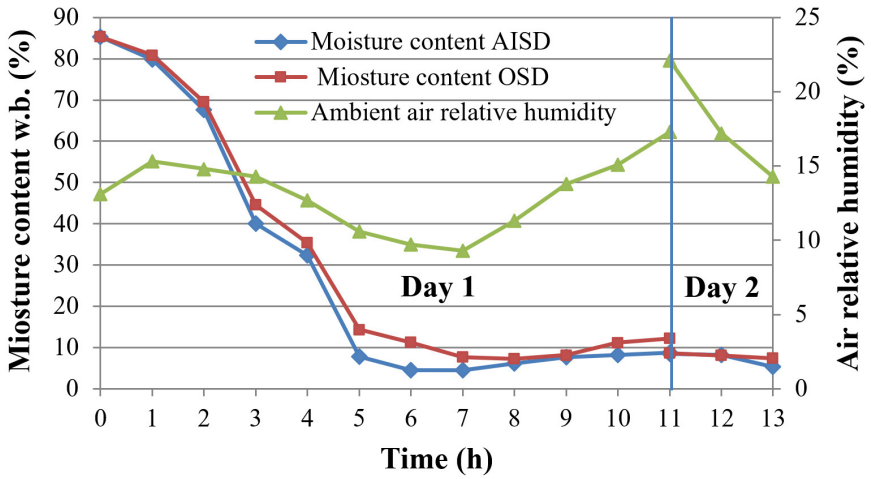

Fig. 7. Product moisture content (%) versus drying time (h) and ambient air humidity (%).

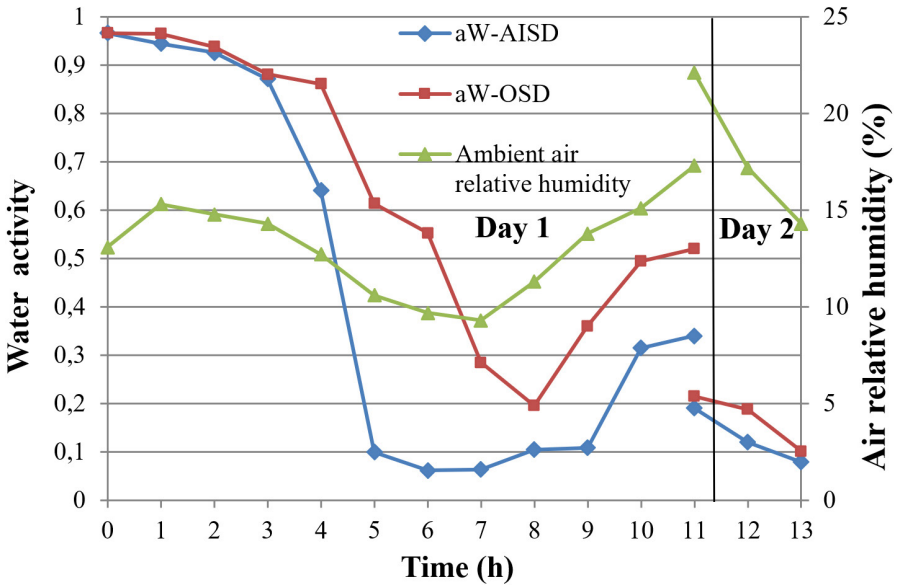

Fig. 8. Product water activity (aW) versus drying time (h) and ambient air humidity (%).

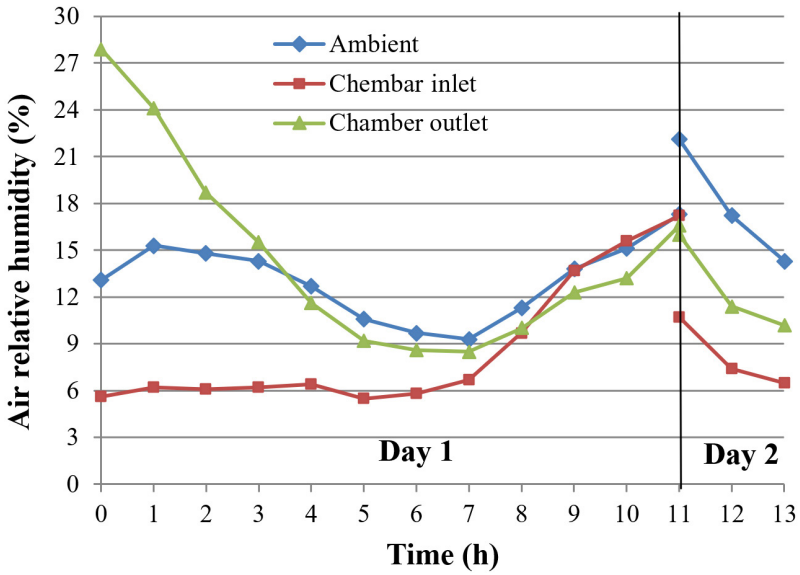

Fig. 9. Air humidity at different locations in the AISD system during product dehydration.

case. Mass loss in the first five hours of working time in the AISD is approximately equal to nine hours in the OSD system, which means that the AISD system is by approximately 44.4 % more time-efficient than the OSD system. Lakshmi et al. (2019) studied drying of stevia leaves and recorded a 60 % higher time efficiency of a mixed mode solar dryer (MMSD) compared to open sun drying. However, mixed mode solar dryers combine forced air flow with direct sunlight which results in higher temperatures. High temperatures, however, can destroy the product texture and increase its rehydration capability (Mujaffar et al., 2016). Lower drying time in cabinet solar dryers compared to open sun dryers was confirmed also by Chauhan et al. (2018).

The change of product moisture content measured by a moisture analyzer is presented in Fig. 5. The initial moisture content of mint leaves was 85.29 % which decreased to 5.38 % in AISD and to 7.42 % in OSD. During the last measurement hours, a slight increase in the product moisture content was recorded. The same phenomena were observed also in water activity curves (Fig. 6).

Water activity is one of the storage stability (shelf-live) characteristics of dried products. The initial water activity of fresh mint leaves was 0.97. In the AISD system, the product reached the most suitable level of water activity below 0.5 in the first seven hours of the experiment. In case of OSD, the dried product did not reach water activity below 0.7 at the given ambient conditions. At the end of the drying processes, water activity curves showed an opposite movement and the products water activity started increasing, which means that the dried product started to absorb water from the ambient humid air after the sunset when the air relative humidity increased. Repeated measurements confirmed this phenomenon. To determine the significance of this rehydration process and the extent of the product water activity increase during the late hours of the day, a second series of experiments was carried out in which the experiments continued also during the evening hours. The results are shown in (Figs. 7, 8 and 9).

As shown in Figs. 7 and 8, an increase in the air relative humidity after seven hours (4:30 pm) of the working time when the sun became to set, water absorption begins and continues until the end of the experimental time. Water absorption from ambient air is more clearly visible in the water activity behavior than in the product moisture content curves as reabsorbed water is available in free form in the product and its small amount causes significant increase in the water activity. By increasing the ambient air relative humidity during the evening hours from 10 to 17 %, the water activity of the product increased from 0.2 to 0.52 in the OSD system. Also, the air relative humidity in the chamber of the AISD system reached similar values after the sunset (Fig. 9) when ambient air and product water activity increased from 0.1 to 0.32. Restart of the drying process the next day at 8:00 am decreased the product water activity in both systems due to the decreasing ambient air humidity and increasing temperature.

In Afghanistan, where air humidity is very low, ambient pressure is around 82 kPa and usual air relative humidity remains at low values also during the night, the increase in product water activity during the evening hours does not represent a significant hazard. However, in many other locations with higher air humidity, the increase in water activity during the process can present a significant problem as it can cause product spoilage. Based on this observation, it can be stated that changes in ambient conditions during the day can crucially affect solar drying processes, particularly the product water activity thus causing product spoilage. This issue has to be considered in the solar drying system design.

Water sorption from ambient air during storage

To determine the importance of water sorption from the ambient air in the climate conditions of Afghanistan, a rehydration experiment was carried out considering the storage of dried products at average ambient conditions (temperature of 29.6 °C, relative humidity of 22.8 %, pressure of 81.1 kPa)).

The results are shown in Figs. 10 and 11. Both moisture content and water activity curves indicate that during the first two or three days, the products absorbed water from ambient air and their water activity increased; however, after the second and third day of the experiment, the products slowly dried and their water activity decreased. When the daily average ambient humidity curve was added to the plot, the reason was clear: the decrease in water activity and moisture content was caused by the decrease in ambient air relative humidity. Generally, the results show that in locations with dry climate, such as Afghanistan, dried product rehydration does not present a significant problem. However, rehydration of dried product in ambient air during the process or storage in open air in locations with higher air humidity can represent a significant hazard due to product spoilage. Especially leafy vegetable products with poor texture have higher rehydration rate than other vegetables such as potatoes, during the storage time (BobiĆ et al., 2002, Chauhan et al. 2018).

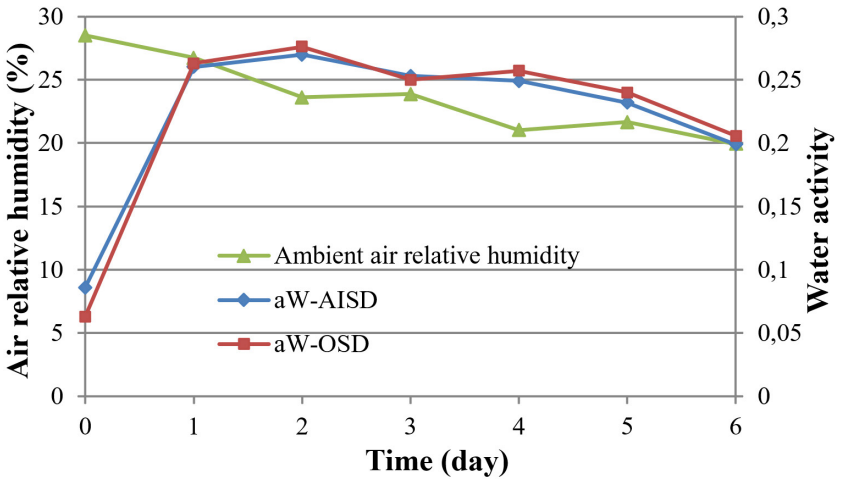

Fig. 10. Variation of water activity (aW) during dry product rehydration.

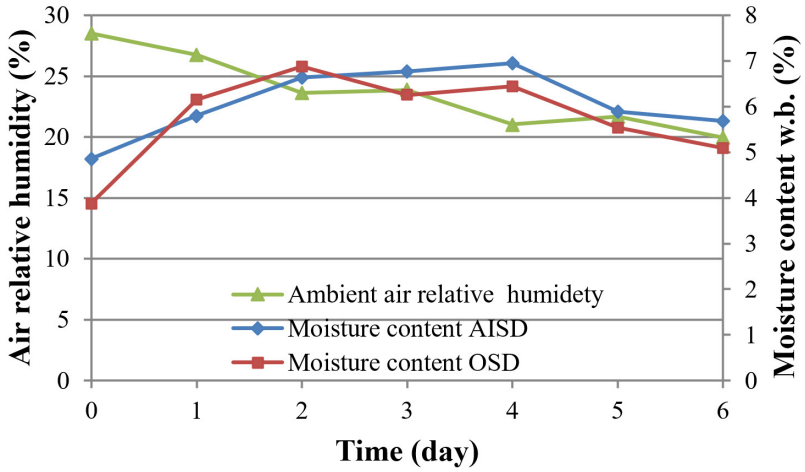

Fig. 11. Variation of moisture content (%) during dry production rehydration.

Fig. 12. OSD and AISD product color comparison: a – AISD products, b – OSD products.

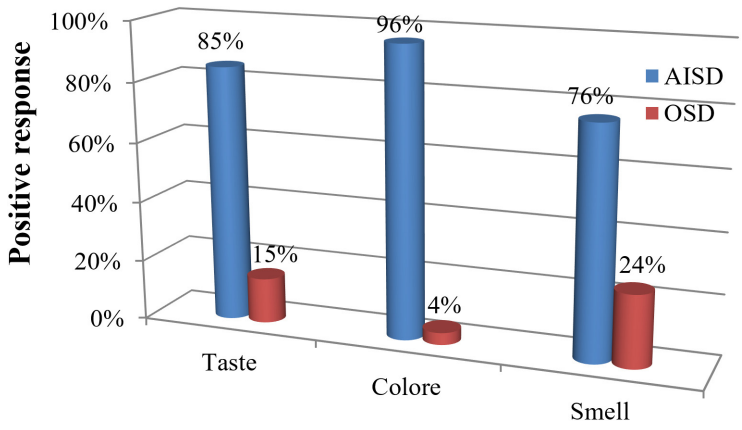

Fig. 13. Statistic survey results.

Comparison of quality parameters of dried products

Fig. 12 shows an overview of the dried products; sample Aa is the dry mint produced in AISD, sample Ab is the OSD dried product, Ca and Da samples are AISD dried product while Cb and Db represent OSD dried product in various forms (milled and unmilled). In all three pictures, better color quality of the AISD product is clearly visible. Picture B compares the dried product immediate water sorption. The product from the OSD system (Bb) seems to be more hydrophilic than that from the AISD system (Ba). Open sun drying and high temperature destroy the mint leave texture and increase its rehydration capability (Mujaffar et al., 2016).

A survey of the sensory parameters: odor, color, and taste, of OSD and AISD dried mint leaves was done with 120 respondents. The respondents were asked to select the product with better color, odor, and taste. The result of the survey is shown in Fig. 13. More than 95 % of the respondents have chosen color, 85 % taste and 76 % odor to be better in the AISD dried product. The results indicate that the AISD system ensures not only faster drying of the products and prevents contamination, but it also shows lower potential for product rehydration and better visible quality parameters.

Conclusion

Changes of ambient conditions such as temperature and air relative humidity during the day can significantly affect the performance of solar drying systems. In an open sun drying system, by the ambient air relative humidity increase from 10 to 17 % during the day, water activity of the product increased from 0.2 to 0.52. In the AISD system product, water activity increased from 0.1 to 0.32. In locations with dry climate such as Afghanistan, dried product rehydration during the processing and storage does not represent a significant issue. However, in locations with higher air humidity, this hazard can be quite significant since water activity of the dried product can reach values suitable for microorganisms' reproduction. The results of this study show that the AISD system is by approximately 44.4 % more time efficient than the OSD system in drying mint leaves. During the first seven hours of the experiment in the AISD system, the product water activity decreased below 0.5 from the initial value of 0.97, while the dried product did not reach water activity below 0.7 in the OSD system at the given ambient conditions. Compared to the OSD system, AISD provides not only faster and safer food product drying, but it also ensures lower potential of product rehydration and better sensory parameters. From 120 respondents, the product dried in the AISD system was positively evaluated by 95 % for color, 85 % for taste and 76 % for odor.

Acknowledgement

This work was supported by the Grants APVV-15-0148 and APVV-19-0170 provided by the Slovak Research and Development Agency.

References

Akpinar EK (2010) Energy conversion and management 51: 2407–2418.

Akpinar EK (2006) Journal of Food Engineering 77: 864–870.

Akpinar EK, Bicer Y, Cetinkaya F (2006) Journal of food engineering 75: 308–315.

Aktaş M, Khanlari A, Aktekeli B, Amini A (2017) International Journal of Hydrogen Energy 42: 18034–18044.

Amini MH, Hamdam SM (2017) International Journal of Pharmacognosy and Chinese Medicine 1: 2576–4772.

Anwar SI, Tiwari GN (2001) Energy conversion and management 42: 627–637.

Babu AK, Kumaresan G, Raj VAA, Velraj R (2018) Renewable and Sustainable Energy Reviews 90: 536–556.

Bhardwaj ML (2012) In: Bhardwaj ML, Sharma HD, Kumar M, Kumar, R, Kansal S, Thakur K, Singh SP,Kumar D, Kumari S, Gupta M, Sharma V (Eds) Vegetable production under changing climate scenario (pp 13—18). Dr Y S Parmar University of Horticulture and Forestry, Nauni, Solan, Himachal Pradesh, India.
BobiĆ Z, Bauman I, ĆuriĆ D (2002) Sadhana, 27(3): 365—374.
César LVE, Lilia CMA, Octavio GV, Isaac PF, Rogelio BO (2020) Renewable Energy 147: 845—855.
Chauhan N, Singh S, Singh J, Samsher, Chandra S, Singh BR, Singh G (2018 Journal of Pharmacognosy and Phytochemistry 7:1507—1509.
Demissie P, Hayelom M, Kassaye A, Hailesilassie A, Gebrehiwot M, Vanierschot M (2019) Energy Procedia 158: 1128—1134.
Doymaz I (2006) Journal of Food Engineering 74: 370—375.
Ekechukwu OV, Norton B (1999) Energy conversion and management 40: 615—655.
Eltawil MA, Azam MM, Alghannam AO (2018) Journal of cleaner production 181: 352—364.
Essalhi H, Benchrifa M, Tadili R, Bargach MN (2018) Innovative food science & emerging technologies 49: 58—64.
Fadhel A, Kooli S, Farhat A, Bellghith A (2005) Desalination 185: 535—541.
Hatami S, Payganeh G, Mehrpanahi A (2020) Journal of Cleaner Production 244: 118809.
Heuring E (2010) Afghanistan-Sustainable horticulture crop production. Libraries digital conservancy, papers 41.
Islam M, Islam MI, Tusar M, Limon AH (2019) Energy Procedia 160: 769—776.
Jahangiri M, Haghani A, Mostafaeipour A, Khosravi A, Raeisi HA (2019) Renewable and Sustainable Energy Reviews 99: 169—190.
Jain D, Tiwari GN (2003) Energy 28: 37—54.
Jain D, Pathare PB (2007) Journal of Food Engineering 78: 1315—1319.
Joardder MUH (2016) A study on pore formation and evolution, and its effect on food quality during intermittent microwave-convective drying (IMCD). [PhD. Thesis.] Australia, Queensland University of Technology.
Karam MC, Petit J, Zimmer D, Djantou EB, Scher J (2016) Journal of Food Engineering 188: 32—49.
Kingsly ARP, Meena HR, Jain RK, Singh DB (2007) Journal of food engineering 79: 6—10.
Kudra T, Mujumdar AS (2009) Advanced drying technologies (2nd Ed). CRC Process, Taylor & Francis Group.
Lakshmi DVN, Muthukumar P, Layek A, Nayak PK (2019) Solar Energy 188: 507—518.
Maker Associates Limited (MMA) (2008) Dried Fruit and Vegetables for Urban and Export Markets Sub Sector and Value Chain Analysis Tanzania. Study Commissioned by SME Competitiveness Facility, Tanzania.
Mohamed LA, Kane CSE, Kouhila M, Jamali A, Mahrouz M, Kechaou N (2008) Energy Conversion and Management 49: 940—946.
Mujaffar S, Loy AL, Augustine T (2016) Journal of Food Research 5(6): 33—44.
Mulet A, Carcel JA, Sanjuan N, Bon J (2003) Food Science and Technology International 9: 215—221.
Mustayen AGMB, Mekhilef S, Saidur R (2014) Renewable and Sustainable Energy Reviews 34: 463—470.
Noori AW, Royen MJ, Haydary J (2019) Acta Chimica Slovaca 12: 142—149.
Palka EJ (2001) Afghanistan: A Regional Geography. CRC Process, United states Military Academy.
Petros D, Gebrehiwot M, Vanierschot M, Hailesilassie A, Hayelom M, Kassaye A (2019) Energy Procedia 158: 1128—1134.
Purohit P, Kumar A, Kandpal TC (2006) Solar energy 80: 1568—1579.
Sagar VR, Kumar SP (2010) Journal of food science and technology 47: 15—26.
Saleh A, Badran I (2009) Renewable Energy 34: 2239—2245.
Sormoli ME, Langrish TAG (2016) LWT-Food Science and Technology 72: 1—8.
Swami SB, Das SK, Maiti B (2006) Biosystems engineering 93: 393—402.
Toğrul İT, Pehlivan D (2004) Journal of Food Engineering 65: 413—425.
Tunde-Akintunde TY (2011) Renewable energy 36: 2139—2145.
USAID Afghanistan (2011) Accelerating Sustainable Agriculture, UASAP Final Report. USAID Contract No. 306-C-00-07-00501-00.
Vijayan S, Arjunan TV, Kumar A (2020) Renewable Energy 146: 2210—2223.
Wang WC (2016) Design and Analysis of an Energy Efficient Dehumidification System for Drying Applications. [Ph.D. Thesis.] London, University of Hertfordshire.
Zambrano MV, Dutta B, Mercer DG, MacLean HL (2019) Trends in Food Science & Technology 88: 484—496.

sciendo

Influence of sea buckthorn juice addition on the growth of microbial food cultures

Svetlana Schubertová, Zuzana Burčová, Mária Greifová, Marianna Potočňáková, Lívia Janotková, František Kreps

Department of Food Science and Technology, Faculty of Chemical and Food Technology, Slovak University of Technology in Bratislava, Radlinského 9, 812 37 Bratislava, Slovak Republic
svetlana.schubertova@stuba.sk

Abstract: The aim of the article was to investigate the effect of sea buckthorn juice addition on the growth of microbial cultures in growth medium and juice mixtures. Pure sea buckthorn juice was found to inhibit the growth of all 11 monitored microbial cultures. *Lactobacillus plantarum* CCM 7039, *Lactobacillus plantarum* K816, *Lactobacillus brevis* CCM 1815 and, to a lesser extent, the probiotic strain *Lactobacillus rhamnosus GG*, grew in a growth medium containing a 25 % addition of sea buckthorn juice. *Lactobacillus plantarum* K816 and *Lactobacillus brevis* CCM 1815 grew better in this mixture than in pure growth medium. Moreover, we focused on finding a suitable ratio of sea buckthorn and apple juice for *Lactobacillus plantarum* CCM 7039, leading to malolactic fermentation, which results in an increase in the pH value and an improvement in the sensory properties of juices. The intention was to incorporate the highest possible addition of sea buckthorn juice while maintaining the viability of *Lactobacillus plantarum* CCM 7039 for malolactic fermentation to occur. The best results were achieved using 40 % sea buckthorn juice. Practical application of the results points to the possibility of preparing a fermented fruit beverage and a dairy product containing sea buckthorn juice. The results of this work extend the current options of sea buckthorn juice processing increasing thus the consumption of healthy juice.

Keywords: bacteria growth, health promoting food, sea buckthorn juice

Introduction

Sea buckthorn (*Hippophae rhamnoides*) juice is a rich source of many bioactive compounds. It contains vitamin C in the range of 0.98—5.14 mg/g, depending on the analysed variety, cultivar, harvest time, growth site and climatic conditions during cultivation (Hussain et al., 2014; Sytařová et al., 2020), and a high number of phenolic substances, the most numerous being glycosides of phenols. Their content ranges from 0.59 to 4.07 mg/g. Among them, glycosides of isorhamnetin and quercetin predominate (Ma et al., 2017; Teleszko et al., 2015). Carotenoids are present mainly in form of β-carotene (Andersson et al., 2009; Sytařová et al., 2020), vitamin E in form of α-tocopherol (Eccleston et al., 2002; Kallio et al., 2002) and niacin is the most abundant of the B vitamins. The content of these substances, together with the content of minerals, puts sea buckthorn in the foreground in terms of nutritional value compared to other fruits (Stobdan et al., 2010).

Many of these substances, mainly phenolic compounds, have a strong antioxidant activity (Gao et al., 2000; Rop et al., 2014; Sharma et al., 2008; Sytařová et al., 2020). Antioxidant properties of sea buckthorn berries determines its various health benefits including the cytoprotective effect of sea buckthorn flavonoids reducing endothelial cell injuries (Bao & Lou, 2006), lymphocytes apoptosis and formations of DNA breaks (Geetha et al., 2009) induced by oxidizing agents. Moreover, some studies document antiproliferative effect of phenols extracted from sea buckthorn berries against human cancer cells. Guo et al. (2014) observed a correlation between antiproliferation towards liver cancer cells and the content of phenolic acids and flavonoids. One of the substances with a strong impact in this process is isorhamnetin. Monitoring of the effect of isorhamnetin on colon cancer cells showed that isorhamnetin induced cell cycle arrest and suppressed cell proliferation by inhibiting the signal pathway affecting metabolism and stress response (Li et al., 2014). Another study showed apoptosis of lung cancer cells induced by down-regulation of oncogenes and up-regulation of apoptotic genes due to the application of isorhamnetin (Li et al., 2015). Another benefit of sea buckthorn berries and their juice is their antiatherogenic effect. Multiple authors have proven that phenolic compounds can be used to prevent thrombogenesis thanks to their antiplatelet activity (Cheng et al., 2003; Olas et al., 2016; Skalski et al., 2019). Also, sea buckthorn juice and its components decrease the susceptibility of low-density lipoproteins to oxidation (Eccleston et al., 2002) and thus protect macrophage against apoptosis associated with atherosclerotic plaque formation (Skalski et al., 2019). Another way sea buckthorn fruit contributes to the prevention of cardiovascular disease is by promoting re-

duction in serum triglycerides and very low-density lipoproteins levels (Larmo et al., 2013). Consumption of sea buckthorn berries offers improvement in human metabolism in form of delayed insulin response and improved glycaemic profile (Mortensen et al., 2018). Attri et al. (2018) reported probiotic properties of sea buckthorn juice. The presence and digestion of its polyphenols influence the gut microbial population towards proliferation of beneficial bacteria.

Sea buckthorn juice contains organic acids in the range of 18—54 mg/g, of which malic acid represents 8—40 mg /g. The pH value is in the range of 2.57—3.20. The monosaccharide content is 5—74 mg/g and the monosaccharide to acid ratio is typically below 1 (Ma et al., 2017; Markkinen et al., 2019; Tkacz et al., 2020; Zheng et al., 2012). These parameters cause the sourness and astringency of sea buckthorn juice (Ma et al., 2017; Tiitinen et al., 2005) and sea buckthorn berries are perceived as less-liked fruit (Laaksonen et al., 2016). Suitable ways to increase the attractiveness of sea buckthorn juice and minimize its less pleasant taste are to ferment it or to incorporate the juice into dairy products. Therefore it is desirable to investigate the effect of sea buckthorn juice on the viability of microorganisms used in the food production process. In addition, the use of sea buckthorn fruit in food offers the benefit of pathogenic bacteria inhibition. *Staphylococcus aureus* was inhibited by lyophilized berries and by phenolic berry extract while *Salmonella enterica* sv. Typhimurium was inhibited by lyophilized berries only (Puupponen-Pimiä et al., 2005).

Malolactic fermentation, enzymatic decarboxylation of malic acid to lactic acid, is a commonly used process, especially in the production of red wine as it increases pH, decreases bitterness, and softens the flavour (Jackson, 2008). The application of malolactic fermentation in fruit juice processing leads to several positive changes; e.g., Filannino et al. (2013) monitored the course of malolactic fermentation of pomegranate juice using different strains of *Lactobacillus plantarum*. Fermented juice showed increased concentration of total polyphenolic compounds, improved antioxidant activity, enhanced antimicrobial activity against *Escherichia coli* and *Bacillus megaterium* and preferable sensory attributes compared to unfermented juice. Di Cagno et al. (2011) used mixed lactic acid bacteria starter to process fruit and vegetable smoothies. In this case, malolactic fermentation led to better preservation of polyphenolic compounds and ascorbic acid and thus to improved antioxidant activity. Sensory properties were improved as well. In another studies, the authors confirmed the increased antioxidant activity (Li et al., 2019; Wu et al., 2020) and improved aroma complexity (Chen et al., 2019; Ricci et al., 2018) to be a result of malolactic fermentation. Also, malolactic fermentation can lead to extended shell life of juices (Muhialdin et al., 2017).

Malolactic fermentation is the result of lactic acid bacteria metabolism, which in an acidic environment with the intention of increasing pH prefer the metabolism of organic acids over that of monosaccharides (Cirlini et al., 2020; Filannino et al., 2014; Miller et al., 2011). Due to its high content of malic acid, low pH, and low content of monosaccharides (Ma et al., 2017; Zheng et al., 2012), sea buckthorn juice is a suitable medium for malolactic fermentation. Malolactic fermentation was observed in pure sea buckthorn juice (Markkinen et al., 2019; Tkacz et al., 2020) and in a 1:1 mixture of sea buckthorn juice and apple juice (Tkacz et al., 2020) using *Lactobacillus plantarum* and *Oenococcus oeni*; as well as in a 1:1 mixture of sea buckthorn juice and water using *Oenococcus oeni* (Tiitinen et al., 2006).

Regarding the possibility of incorporating sea buckthorn juice into dairy products, the positive effect of the addition of sea buckthorn berries on the viability of *Lactobacillus casei* in the production of cheese (Terpou et al., 2017) and frozen yoghurt (Terpou et al., 2019) has been studied so far. This issue remains without extensive research.

Material and methods

Materials

Sea buckthorn and apple juice were purchased from Tvrdošovské zlato (Tvrdošovce, Slovak Republic). Apple juice was prepared from a mixture of apples of the variety Golden Delicious, Jonagold and Gala. Sea buckthorn juice was obtained by pressing sea buckthorn berries of the cultivar Leikora. The lipid fraction was not centrifuged. In the production process, the juices were pasteurized at 82 °C in a circulation pasteurizer for 2—3 seconds and then immediately filled into plastic containers.

Determination of ascorbic acid content

The ascorbic acid content was determined by an HPLC analysis system Agilent Technologies 1260 Infinity II LC System with a Multiple Wavelength Detector and a Quaternary Pump using 20 mmol/l of potassium dihydrogen phosphate (Chemapol, Czech Republic) acidified with sulphuric acid (Centralchem, Slovak Republic) to pH 2.4 as the mobile phase. The standard of ascorbic acid was of analytical grade and was purchased from Sigma-Aldrich (Slovak Republic). Prior to the analysis, the juices were precipitated by Carrez solu-

tions and filtered. Carrez I (30 % aqueous solution of zinc sulphate) and Carrez II (15 % aqueous solution of potassium hexacyanoferrate) were prepared using chemicals purchased from Centralchem (Slovak Republic).

Determination of total phenolic and flavonoid content

The total phenolic content was determined spectrophotometrically after a reaction with the Folin-Ciocalteu reagent and sodium carbonate anhydrous, p. a. (both purchased from Centralchem, Slovak Republic), according to Yu et al. (2002). The flavonoid content was determined spectrophotometrically after a reaction with aluminium chloride $\cdot 6H_2O$ in ethanol (both purchased from Centralchem, Slovak Republic) according to Kreft et al. (2002). The standards of gallic acid and quercetin were of analytical grade and were purchased from Sigma-Aldrich (Slovak Republic).

Microbial cultures

The growth of 11 microbial cultures was studied: *Lactobacillus plantarum* CCM 7039 (Czech Collection of Microorganisms), *Lactobacillus plantarum* K816, *Lactobacillus acidophilus* LA, *Lactobacillus brevis* CCM 1815, *Lactobacillus reuteri* BioGaia, *Lactobacillus rhamnosus* GG, *Streptococcus thermophilus* TH3, yoghurt starter culture (*Streptococcus thermophilus*, *Lactobacillus delbrueckii ssp. bulgaricus*), probiotic starter culture (*Streptococcus thermophilus*, *Lactobacillus acidophilus*, *Bifidobacterium*), sour cream starter culture (*Lactococcus lactis ssp. lactis*, *Lactococcus lactis ssp. cremoris*, *Lactococcus lactis ssp. diacetilactis*) and kefir starter culture (*Lactococcus lactis ssp. lactis*, *Lactococcus lactis ssp. cremoris*, *Lactocccus lactis ssp. diacetilactis*, *Lactobacillus acidophilus*, *Lactococcus delbrueckii*, *Lactobacillus kefir*, yeasts *Candida kefir* a *Kluyveromyces marxianus*). Dried pure cultures were purchased from Christian Hansen (Denmark) and dried mixed cultures from Milcom a.s. (Czech Republic). Suspensions used in the experiment were obtained from overnight cultures grown in MRS (de Man, Rogosa and Sharpe) broth and rinsed twice with saline. Initial concentration of bacterial cells was approximately 10^9 colony forming units in 1 ml.

Analysis of microbial culture growth

The growth of microbial cultures in MRS broth (Merck, Germany), solutions of MRS broth and sea buckthorn juice with final juice concentrations of 25 % and 50 %, and in pure sea buckthorn juice was monitored spectrophotometrically. Before adding sea buckthorn juice to the MRS broth, it was centrifuged for 10 minutes; due to its opacity. After phase separation, the middle, clearest, phase was separated and used. Then, 200 µl of individual solutions and 20 µl of microbial suspensions were added to the wells of the microtiter plate. The inoculated solutions were incubated in a microplate reader Epoch Microplate Spectrophotometer, BioTek (Slovak Republic) for 24 hours at 37 °C under aerobic conditions. Absorbance was measured every hour at the wavelength of 600 nm after brief stirring of the plate. From the measured absorbance values, absorbance of the blank represented by the uninoculated solutions was subtracted.

The viability of *Lactobacillus plantarum* CCM 7039 in not centrifuged sea buckthorn and apple juice mixtures was determined by a culture method. Juice mixtures (5 ml) with the final sea buckthorn juice concentrations of 10 %, 20 %, 30 % and 40 % were prepared and inoculated with 500 µl of bacterial suspension. Then, they were placed in a thermostat set to 37 °C under aerobic conditions. At 0^{th}, 10^{th}, 24^{th}, 48^{th} and 72^{th} hours, samples were taken and inoculated on MRS agar (Biolife Italiana, Italy). After culturing for 48 hours in a thermostat, colony forming units were counted.

Statistical analysis

Absorbance, according to which the growth of microorganisms was described, was measured in three replicates. Inoculation for colony forming units calculation was also performed in three replicates. Standard deviations were calculated in Excel and the graphs were constructed in OriginPro 8.1.

Results and discussion

Characterisation of sea buckthorn and apple juice

Sea buckthorn juice had the pH of 2.8 and contained 4.90 mg/g of ascorbic acid, 210.32 mg GAE/g of phenols (gallic acid equivalent), 1.40 mg QE/g of flavonoids (quercetin equivalent). Apple juice had the pH of 3.4 and 0.058 mg/g of ascorbic acid, 13.57 mg GAE/g of phenols, and 9.29 mg QE/kg of flavonoids.

Influence of sea buckthorn juice addition on the growth of microbial cultures

The effect of sea buckthorn juice addition to MRS broth on the growth of seven pure and four mixed microbial cultures was investigated. Identification of bacteria capable of growing in such an environment allows designing new foods which combine the nutritional and functional properties of sea buckthorn juice, the taste of fermented products, and the benefits of probiotic products. Up to date, only a limited number of publications monitoring

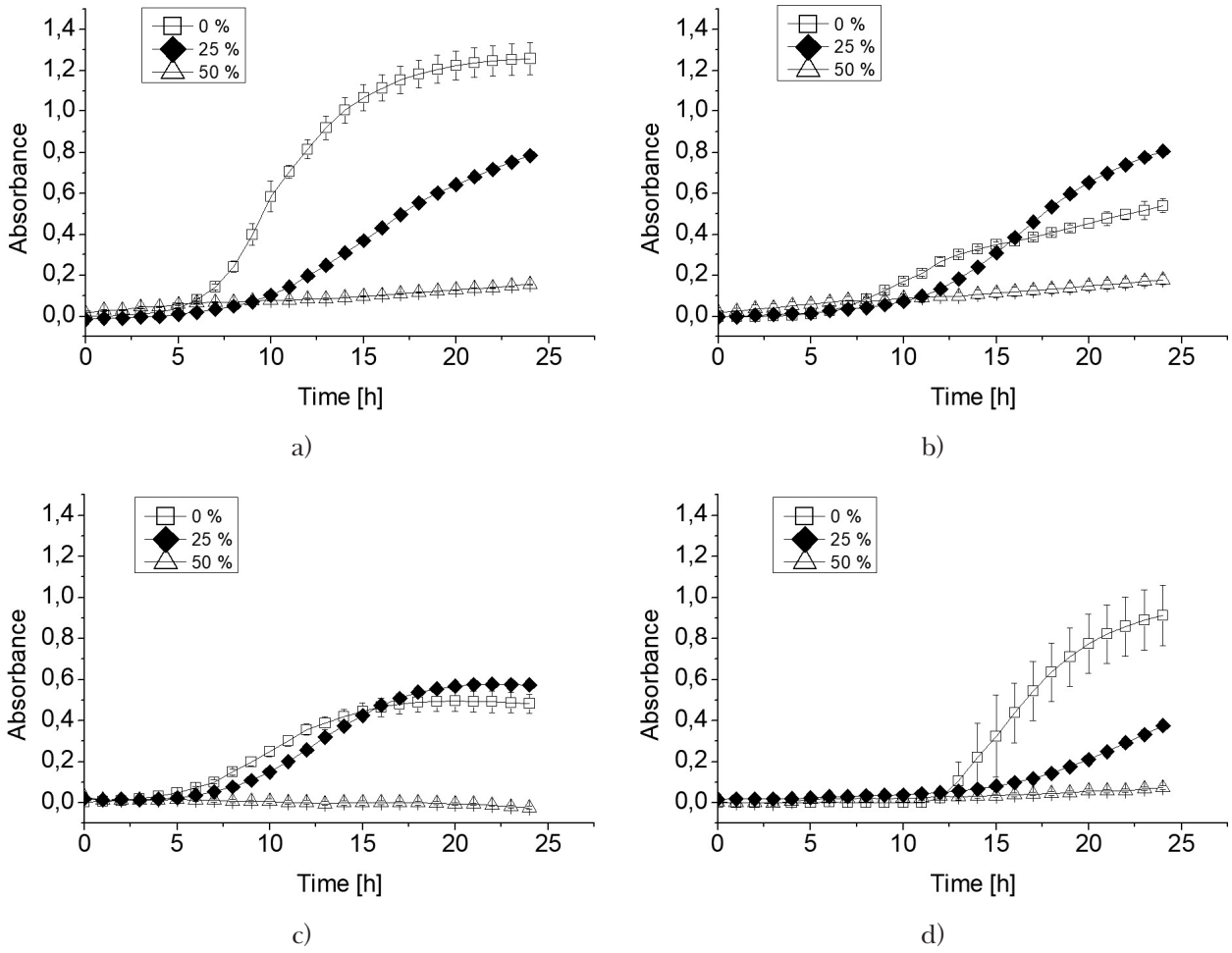

Fig. 1. Effect of 0 %, 25 % and 50 % addition of sea buckthorn juice to MRS broth on the growth of a) *Lactobacillus plantarum* CCM 7039, b) *Lactobacillus brevis* CCM 1815, c) *Lactobacillus plantarum* K816, d) *Lactobacillus rhamnosus* GG. Note: The effect of 100 % sea buckthorn juice is not shown due to complete inhibition of the growth of microorganisms.

the viability of lactic acid bacteria in sea buckthorn juice have been published.

Lactobacillus plantarum CCM 7039 (Fig. 1a), *Lactobacillus brevis* CCM 1815 (Fig. 1b) and *Lactobacillus plantarum* K816 (Fig. 1c) showed good growth in 25 % sea buckthorn juice. *Lactobacillus plantarum* K816 and *Lactobacillus brevis* CCM 1815 had better viability in 25 % sea buckthorn juice than in MRS broth without added buckthorn juice. Markkinen et al. (2019) and Tkacz et al. (2020) pointed to the growth of *Lactobacillus plantarum* in pure sea buckthorn juice, while our results do not indicate the growth of *Lactobacillus plantarum* CCM 7039 or *Lactobacillus plantarum* K816 in this environment. Contrasting results may be due to the use of a different variety of sea buckthorn and different *Lactobacillus plantarum* strain.

Lactobacillus rhamnosus GG (Fig. 1d) grew weakly in 25 % sea buckthorn juice; there is no published study focused on the preparation of a drink containing sea buckthorn juice and *Lactobacillus rhamnosus GG*. However, Sheehan et al. (2007) prepared probiotic orange and pineapple juice in which *Lactobacillus rhamnosus GG* survived at least 12 weeks at commercially critical levels. Despite the weak growth of *Lactobacillus rhamnosus* GG in the presence of sea buckthorn juice, this finding is interesting due to the probiotic nature of this bacterial strain. *Lactobacillus rhamnosus* GG is an effective agent protecting the intestinal tract from pathogens (EFSA Panel on Dietetic Products, Nutrition and Allergies, 2011). The combination of a probiotic with nutritious sea buckthorn juice with a prebiotic effect (Attri et al., 2018) and, at the same time, inhibiting the growth of pathogenic bacteria (Puupponen-Pimiä et al., 2005), could allow for the preparation of a new product supporting intestinal health.

Apart from the four bacterial cultures mentioned above, the other microbial cultures studied were not able to grow in the MRS broth with an addition of sea buckthorn juice. Thus, it would be advantageous to find conditions allowing for the

combination of sea buckthorn juice and yoghurt culture, which is a widespread starter culture improving lactose digestion (EFSA Panel on Dietetic Products, Nutrition and Allergies, 2010).

While monitoring the fermentation of pomegranate juice, Mousavi et al. (2013) observed the growth of *Lactobacillus acidophilus* for 72 hours while the lag phase of *Lactobacillus acidophilus* lasted for 24 hours. It is possible that in our 24-hour experiment, the lag phase of *Lactobacillus acidophilus* was not completed. Thus, under other conditions, *Lactobacillus acidophilus* could potentially be another probiotic bacterium suitable for combination with sea buckthorn juice.

In a publication focused on the development of a food matrix enriched with probiotics, the viability of probiotic strains of *Lactobacillus plantarum*, *Lactobacillus rhamnosus* and *Lactobacillus acidophilus* in sea buckthorn juice was ensured by adjusting the pH of the juice to 4.5 and by addition of malt. The presence of sea buckthorn juice has enhanced the antipathogenic effect of bacteria, especially in case of *Lactobacillus rhamnosus* GG. The observed increase in antipathogenic effect was higher than in equally treated apple juice (Sireswar et al., 2017b). The second possibility of formulating a probiotic beverage containing *Lactobacillus rhamnosus* GG is the supplementation of sea buckthorn juice with whey protein, trisodium citrate, and dextrose (Sireswar et al., 2017a). In order to formulate a probiotic sea buckthorn beverage, the addition of similar ingredients to create more suitable conditions for the growth of probiotic microorganisms is to be considered.

Viability of Lactobacillus plantarum CCM 7039 in mixtures of sea buckthorn and apple juice

Research on the fermentation of fruit juices points to many advantages of such processed products. *Lactobacillus plantarum* is widely used in this process; its metabolism leads to changes that positively affect the antioxidant activity and organoleptic properties (Cirlini et al., 2020; Espirito-Santo et al., 2015; Filannino et al., 2013; Hashemi et al., 2017; Chen et al., 2019; Kwaw et al., 2018; Li et al., 2019; Markkinen et al., 2019; Mousavi et al., 2013; Muhialdin et al., 2020; Ricci et al., 2018; Wu et al., 2020). Here, the most suitable ratio to mix sea buckthorn and apple juice to maintain the viability of *Lactobacillus plantarum* CCM 7039 for malolactic fermentation was studied (Fig. 2.). This microorganism was chosen because its growth in MRS broth with a 25 % addition of sea buckthorn juice (Fig. 1a) was better than the growth of *Lactobacillus plantarum* K816 (Fig. 1d) under the same conditions. Tkacz et al. (2020) monitored the growth of *Lactobacillus plantarum* in a 1:1 mixture of sea buckthorn and apple juice and described the course of malolactic fermentation for 72 hours. They documented an increase in flavonol content and antioxidant activity of the juice mixture due to fermentation. As a result of weak growth of *Lactobacillus plantarum* CCM 7039 in the MRS broth with a 50 % addition of sea buckthorn juice (Fig. 1a), lower concentrations of the juice were employed than mentioned by these authors.

After 72 hours, the number of colony forming units decreased by approximately 4.7 logs for the 10 % sea buckthorn juice, by 5.3 logs for the 20 % juice, by 5.5 logs for the 30 % juice, and by 4.6 logs for the 40 % juice. It has been shown that *Lactobacillus plantarum* cells going through the decline phase have active metabolic pathways associated with malolactic fermentation. The decrease in the amount of malic acid is significant in case of a culture with a decreasing number of viable cells (Brizuela et al., 2017; Brizuela et al., 2018; Sun et

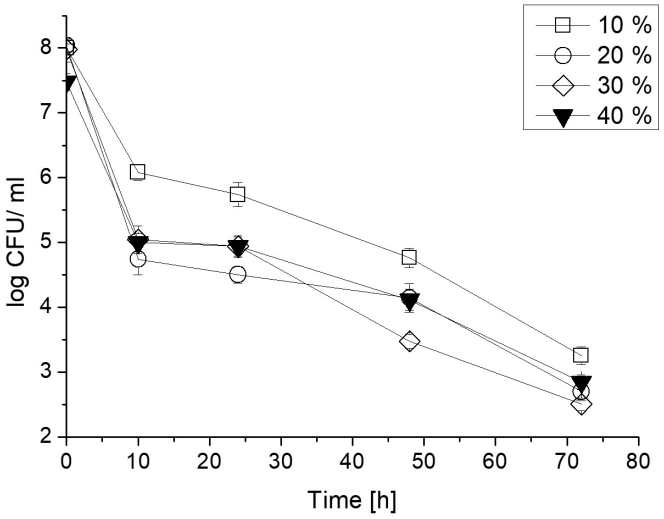

Fig. 2. Viability of Lactobacillus plantarum CCM 7039 in mixtures of sea buckthorn and apple juice with 10 %, 20 %, 30 % and 40 % sea buckthorn juice addition. Note: CFU — colony forming units.

al., 2018). Brizuela et al. (2018) recorded a decrease in the malic acid content even at the cell concentration at the level of 10^4 colony forming units in 1 ml. Our results show that the number of colony forming units at each time point is only slightly dependent on the concentration of the sea buckthorn juice. This means that the use of the highest studied concentration of sea buckthorn juice (40 %) should not be a problem from the point of view of fermentation. In addition, several studies suggest that the more acidic the medium, the more intense the acid conversion (Cirlini et al., 2020; Filannino et al., 2014; Miller et al., 2011). Therefore, the choice of the 40 % sea buckthorn juice could lead to more altered sensory characteristics or other functional properties of the fruit beverage compared to the 10 % sea buckthorn juice.

Conclusion

By monitoring the growth of 11 microbial cultures, *Lactobacillus plantarum* CCM 7039, *Lactobacillus plantarum* K816 and *Lactobacillus brevis* CCM 1815 were identified as microorganisms suitable for the combination with sea buckthorn juice at the concentration of 25 %. *Lactobacillus rhamnosus* GG showed only weak growth in this environment, nevertheless, this finding indicates the possibility of creating a probiotic product containing sea buckthorn juice. None of the monitored microbial cultures grew in a 100 % sea buckthorn juice.

Furthermore, the viability of *Lactobacillus plantarum* CCM 7039 in a mixture of sea buckthorn and apple juice was studied because its metabolism could lead to malolactic fermentation of this material. Differences in the inhibition of *Lactobacillus plantarum* CCM 7039 in mixtures with 20 %, 30 % and 40 % of sea buckthorn juice were not significant. Other studies have shown that the decrease in cell counts does not inhibit the conversion of malic acid to lactic acid (Brizuela et al., 2017; Brizuela et al., 2018; Sun et al., 2018) and that the more acidic the medium, the more intense the acid conversion (Cirlini et al., 2020; Filannino et al., 2014; Miller et al., 2011). Therefore, it can be concluded that among the investigated mixtures, the mixture with the highest concentration of sea buckthorn juice should be chosen for fermentation. In addition to improving the taste, malolactic fermentation offers an increase in the antioxidant activity and in other functional properties of beverages.

Research into the processing of sea buckthorn juice using microorganisms points to the possibilities of preparing new products with improved sensory attributes and with a positive effect on human health.

Acknowledgement

This publication was supported by the Operational Program Integrated Infrastructure within the project: Demand-driven research for the sustainable and innovative food, Drive4SIFood 313011V336, co-financed by the European Regional Development Fund.

References

Andersson SC, Olsson ME, Johansson E, Rumpunen K (2009) Journal of Agricultural and Food Chemistry 57: 250—258.

Attri S, Sharma K, Raigond P, Goel G (2018) Food Research International 105: 324—332.

Bao M, Lou Y (2006) Journal of Cardiovascular Pharmacology 48: 834—841.

Brizuela NS, Bravo-Ferrada BM, La Hens DV, Hollmann A, Delfederico L, Caballero A, Tymczyszyn EE, Semorile L (2017) LWT — Food Science and Technology 77: 348—355.

Brizuela NS, Bravo-Ferrada BM, Pozo-Bayón MÁ, Semorile L, Tymczyszyn EE (2018) Food Research International 106: 22—28.

Cirlini M, Ricci A, Galaverna G, Lazzi C (2020) LWT — Food Science and Technology 118: 108779.

Di Cagno R, Minervini G, Rizzello CG, De Angelis M, Gobbetti M (2011) Food Microbiology 28: 1062—1071.

Eccleston C, Baoru Y, Tahvonen R, Kallio H, Rimbach GH, Minihane AM (2002) The Journal of Nutritional Biochemistry 13: 346—354.

EFSA Panel on Dietetic Products, Nutrition and Allergies, EFSA Journal (2011) 9: 2167.

EFSA Panel on Dietetic Products, Nutrition and Allergies, EFSA Journal (2010) 8: 1763.

Espirito-Santo AP, Carlin F, Renard CM (2015) Food Research International 78: 352—360.

Filannino P, Azzi L, Cavoski I, Vincentini O, Rizzello CG, Gobbetti M, Di Cagno R (2013) International journal of food microbiology 163: 184—192.

Filannino P, Cardinali G, Rizzello CG, Buchin S, De Angelis M, Gobbetti M, Di Cagno R (2014) Applied and environmental microbiology 80: 2206—2215.

Gao X, Ohlander M, Jeppsson N, Björk L, Trajkovski V (2000) Journal of agricultural and food chemistry 48: 1485—1490.

Geetha S, Ram MS, Sharma S, Ilavazhagan G, Banerjee P, Sawhney R (2009) Journal of medicinal food 12: 151—158.

Guo R, Guo X, Li T, Fu X, Liu RH (2017) Food Chemistry 221: 997—1003.

Hashemi SMB, Khaneghah AM, Barba FJ, Nemati Z, Shokofti SS, Alizadeh F (2017) Journal of Functional Foods 38: 409—414.

Hussain M, Ali S, Awan S, Hussain M, Hussain I (2014) International Journal of Biosciences 4: 144—152.

Chen C, Lu Y, Yu H, Chen Z, Tian H (2019) Food Bioscience 27: 30—36.

Cheng J, Kondo K, Suzuki Y, Ikeda Y, Meng X, Umemura K (2003) Life Sciences 72: 2263—2271.

Jackson RS (2008) Wine science: Principles and Applications. Academic press, Cambridge.

Kallio H, Yang B, Peippo P, Tahvonen R, Pan R (2002) Journal of Agricultural and Food Chemistry 50: 3004–3009.
Kreft S, Štrukelj B, Gaberščik A, Kreft I (2002) Journal of Experimental Botany 53: 1801–1804.
Kwaw E, Ma Y, Tchabo W, Apaliya MT, Wu M, Sackey AS, Xiao L, Tahir HE (2018) Food chemistry 250: 148–154.
Laaksonen O, Knaapila A, Niva T, Deegan KC, Sandell M (2016) Food quality and preference 53: 117–126.
Larmo PS, Kangas AJ, Soininen P, Lehtonen H-M, Suomela J-P, Yang B, Viikari J, Ala-Korpela M, Kallio HP (2013) The American journal of clinical nutrition 98: 941–951.
Li C, Yang X, Chen C, Cai S, Hu J (2014) Molecular medicine reports 9: 935–940.
Li Q, Ren F-Q, Yang C-L, Zhou L-M, Liu Y-Y, Xiao J, Zhu L, Wang Z-G (2015) Asian Pacific Journal of Cancer Prevention 16: 3035–3042.
Li Z, Teng J, Lyu Y, Hu X, Zhao Y, Wang M (2019) Molecules 24: 51.
Luo Y, Sun G, Dong X, Wang M, Qin M, Yu Y, Sun X (2015) PLoS One 10: e0120259.
Ma X, Yang W, Laaksonen O, Nylander M, Kallio H, Yang B (2017) Journal of agricultural and food chemistry 65: 9871–9879.
Markkinen N, Laaksonen O, Nahku R, Kuldjärv R, Yang B (2019) Food chemistry 286: 204–215.
Miller BJ, Franz CM, Cho G-S, du Toit M (2011) Current microbiology 62: 1682.
Mortensen MW, Spagner C, Cuparencu C, Astrup A, Raben A, Dragsted LO (2018) European journal of nutrition 57: 2827–2837.
Mousavi ZE, Mousavi SM, Razavi SH, Hadinejad M, Emam-Djomeh Z, Mirzapour M (2013) Food Biotechnology 27: 1–13.
Muhialdin BJ, Kadum H, Zarei M, Hussin ASM (2020) LWT-Food Science and Technology 121: 108992.
Olas B, Kontek B, Malinowska P, Żuchowski J, Stochmal A (2016) Oxidative Medicine and Cellular Longevity 2016.
Puupponen-Pimiä R, Nohynek L, Hartmann-Schmidlin S, Kähkönen M, Heinonen M, Määttä-Riihinen K, Oksman-Caldentey (2005) Journal of Applied Microbiology 98: 991–1000.
Ricci A, Cirlini M, Levante A, Dall'Asta C, Galaverna G, Lazzi C (2018) Food Research International 105: 412–422.
Rop O, Ercişli S, Mlcek J, Jurikova T, Hoza I (2014) Turkish Journal of Agriculture and Forestry 38: 224–232.
Sharma UK, Sharma K, Sharma N, Sharma A, Singh HP, Sinha AK (2008) Journal of agricultural and food chemistry 56: 374–379.
Sheehan VM, Ross P, Fitzgerald (2007) Innovative Food Science & Emerging technologies 8: 279–284.
Sireswar S, Dey G, Dey K, Kundu A (2017) Beverages 3: 48.
Sireswar S, Dey G, Sreesoundarya T, Sarkar D (2017) Food Bioscience 20: 28–35.
Skalski B, Lis B, Pecio Ł, Kontek B, Olas B, Żuchowski J, Stochmal A (2019) Food and Chemical Toxicology 125: 614–620.
Stobdan T, Chaurasia OP, Korekar G, Yadav A, Singh SB (2010) Defence Science Journal 60: 226.
Sun SY, Chen ZX, Jin CW (2018) LWT – Food Science and technology 89: 449–456.
Sytařová I, Orsavová J, Snopek L, Mlček J, Byczyński Ł, Mišurcová L (2020) Food chemistry 310: 125784.
Teleszko M, Wojdyło A, Rudzińska M, Oszmiański J, Golis T (2015) Journal of Agricultural and Food Chemistry 63: 4120–4129.
Terpou A, Gialleli A-I, Bosnea L, Kanellaki M, Koutinas AA, Castro GR (2017) LWT – Food science and Technology 79: 616–624.
Terpou A, Papadaki A, Bosnea L, Kanellaki M, Kopsahelis N (2019) LWT 105: 242–249.
Tiitinen K, Vahvaselkä M, Hakala M, Laakso S, Kallio H (2006) European Food Research and Technology 222: 686–691.
Tiitinen KM, Hakala MA, Kallio HP (2005) Journal of Agricultural and Food Chemistry 53: 1692–1699.
Tkacz K, Chmielewska J, Turkiewicz IP, Nowicka P, Wojdyło A (2020) Food Chemistry 332: 127382.
Wu C, Li T, Qi J, Jiang T, Xu H, Lei H (2020) LWT 122: 109064.
Yu L, Haley S, Perret J, Harris M, Wilson J, Qian M (2002) Journal of Agricultural and Food Chemistry 50: 1619–1624.
Zheng J, Yang B, Trépanier M, Kallio H (2012) Journal of agricultural and food chemistry 60: 3180–3189.

sciendo

Thermodynamic prediction of proton and hydrogen atom abstraction in dehydroascorbic acid and its bicyclic form

Dagmar Štellerová, Vladimír Lukeš

Institute of Physical Chemistry and Chemical Physics, Slovak University of Technology in Bratislava, Radlinského 9, SK-812 37 Bratislava, Slovakia
dagmar.stellerova@stuba.sk

Abstract: Conformation analysis of dehydroascorbic acid and its bicyclic form was performed using the density functional theory. For the energetically preferred conformations, ionization potentials (IP) and bond dissociation enthalpies (BDE) were calculated using the B3LYP functional and 6-311++G** basis set. The effects of aqueous solution were estimated using the solvation model based on density (SMD) and the polarizable continuum model (IEF-PCM). The obtained results were compared with available experimental data for reference L-ascorbic acid (vitamin C). Our calculations indicate that the investigated bicyclic metabolic product of vitamin C can also exhibit limited radical scavenging ability due to the thermodynamically preferred dissociation of tertiary —CH bonds.

Keywords: vitamin C, oxidation product, radical scavenger, pK_a values

Introduction

Chemistry of L-ascorbic acid (**AA**, vitamin C) has been widely studied due to its biological importance (Bendich and Langseth, 1995). This water-soluble organic acid is a well-known radical scavenger and an antioxidant in living systems. Although the molecule of vitamin C normally loses only one electron, two electron oxidations can be observed under *in vitro* electrochemical conditions (Deakin et al., 1986). Apart from being a distinguished reducing agent of reactive radical species, vitamin C is a cofactor in the enzymatic biosynthesis of collagen, catecholamine, carnitine, and peptide neurohormones. It is transported across the blood-brain barrier in its oxidized form, called dehydroascorbic acid (**A**). This molecule is also involved in the oxidation of low-density lipoprotein (Wilson, 2002). Furthermore, dehydroascorbic acid has found its purpose in pharmaceutical industry. It has been used as a biochemical marker of oxidative stress in clinical investigations, as vitamin C dietary supplement or as a mucolytic drug called Ascoxal (Fisher and Ten Pas, 1966).

Since the vitamin C structure determination in 1930s, its oxidation mechanism, which is complex and still not fully understood, has been studied (Tu et al., 2017). Thermodynamics and kinetics of reactions associated with the mechanism have been studied by numerous experimental and theoretical research groups. Vitamin C is in these reactions oxidated to one-electron form — short-lived ascorbate radical, or to fully oxidized two-electron **A** form. Dehydroascorbic acid can also be formed by oxidation of the ascorbate radical or by the disproportionation reaction between two ascorbate radicals. Although the structure of **A** is generally presented as a molecule with one non-aromatic ring (Fig. 1), this structure is known to be energetically unstable in water. It is assumed that the structure of dehydroascorbic acid is an intermediate which immediately goes through ring closure, and along with hydration, forms a stable bicyclic form **B** (Fig. 1). To date, structures associated with the oxidation products of vitamin C have been studied extensively in many theoretical and experimental works (Bielski et al., 1981; Bielski et al., 1985; Kurata and Nishikawa, 2000). Recently, Tu and Njus (Tu et al., 2017; Njus et al., 2020) explored theoretically the oxidation mechanism of ascorbic acid and its reaction with superoxide determining the lowest energy conformations of oxidation products and deprotonated forms of ascorbic acid. In agreement with nuclear magnetic resonance measurements, the bicyclic hydrated isomer of dehydroascorbic acid was found to be the most stable structure of the fully oxidized form of ascorbic acid in aqueous solution. The suggested Pourbaix diagrams and calculated pK_a values were in good agreement with the available experimental values.

The mentioned experimental and theoretical works suggest that the antioxidant activity of the studied molecules is related to the dissociation of hydroxyl groups. On the other hand, thermodynamics of the deprotonation reaction from tertiary —CH bonds has not been discussed or analyzed. Therefore, we decided to theoretically investigate the thermo-

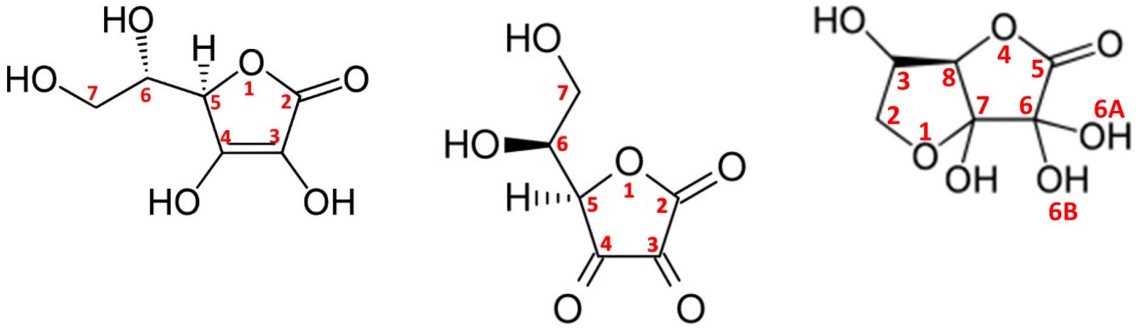

AA **A** **B**

Fig. 1. Schematic structure and atom numbering of L-ascorbic acid (**AA**), dehydroascorbic acid (**A**) and its bicyclic form (**B**).

dynamics of hydrogen atom and proton abstraction from the tertiary methyl —CH groups of dehydroascorbic acid and its bicyclic hydrated isomer (Fig. 1). Partial aims of this study are: (1) perform conformational analysis for the gas-phase and water environment; (2) calculate the reaction enthalpies and Gibbs energies at the room temperature and (3) evaluate the corresponding pK_a values. The obtained results were compared with published theoretical and available experimental data.

Computational Details

All quantum chemical calculations were carried out by the Gaussian 16 software package (Frisch et al., 2016). Visualizations of the parent molecules, their radicals and ions were designed in the Molekel program package (Flukiger et al., 2002). Geometries were optimized using the B3LYP (Lee et al., 1988; Becke, 1988) DFT hybrid functional with the 6-311++G** basis set (Binkley et al., 1980). Vibrational frequency calculations were included at the same level of theory to confirm that the optimised structures were real stationary points and no imaginary vibrations were present. As both dehydroascorbic acid structures have numerous conformers according to the alkyl chain and several rotatable hydroxyl groups, these were investigated first. The lowest-energy structures were used to obtain gas-phase enthalpies and Gibbs free energies of the radicals/ions at p = 101325 Pa and T = 298.15 K. Furthermore, these structures were used as starting points for re-optimization in aqueous solution to obtain more accurate pK_a values. Solvent contribution was applied using SMD (Marenich et al., 2009) and IEF-PCM (Tomasi et al., 2005) polarizable continuum models. The combination of B3LYP with implicit solvent models offers relevant prediction of thermodynamic quantities (Michalík and Lukeš, 2016).

Results and Discussion

The selected energetically preferred structures of L-ascorbic acid (**AA**), dehydroascorbic acid (**A**) and its bicyclic form (**B**) are depicted in Fig. 2. Orientation of the hydroxyl substituents allows the formation of intramolecular hydrogen bonds (see Tab. 1) which contribute to the relative stability of their geometry. For reference L-ascorbic acid, the selected conformation was taken from Tu and Schlegel (2017). The energetically preferred geometry is represented by a planar five-membered ring and a 1,2-dihydroxyethyl chain bent in the direction of the ring forming three stable hydrogen bonds between the groups. The dehydroascorbic acid **A** molecule contains a planar furan-2,3,4(5H)-trione moiety and an 1,2-dihydroxyethyl group. Multiple possible rotations of the 1,2-dihydroxylethyl group around C5—C6 and C6—C7 bonds with respect to the planar ring lead to eighteen possible conformers. For molecule **B**, the presence of bicyclic rings reduces the number of possible conformations. With respect to the orientation of hydroxyl groups, eight possible structures were identified. In case of vitamin C, the studied conformation contains three intramolecular hydrogen bonds. The shortest bond length is that of C4OH···OC7, e.g. 1.757 Å in the gas-phase. The most stable conformation **A** contains only two hydrogen bonds between C6OH···OC4 atoms, with the length of 2.285 Å, and between C6OH···OC7 atoms, with the length of 2.818 Å. The oxolane rings of bicyclic **B** molecule are not planar but bent to each other, leaving groups OH7 and OH3 behind their plane. Therefore, the most energetically preferred **B** conformer possesses eight internal hydrogen bonds. Compared with the gas-phase geometries, the inclusion of implicit solvent models affects the intramolecular bond lengths.

Chemical structure of the studied molecules has direct impact on the homolytic or heterolytic bond

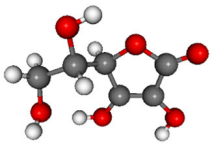

AA
(–684.991461 hartree)

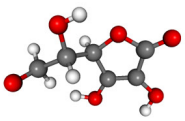

AA(7-OH)
(–684.4040538 hartee)

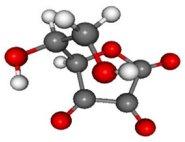

A
(–683.754712 hartree)

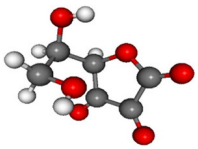

A1
(–683.752188 hartree)

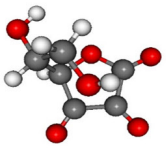

A2
(–683.754407 hartree)

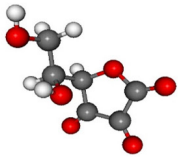

A3
(–683.754028 hartree)

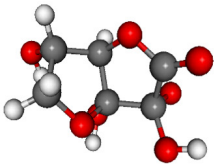

B
(–760.240071 hartree)

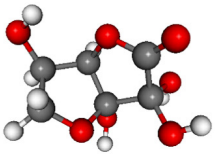

B1
(–760.240106 hartree)

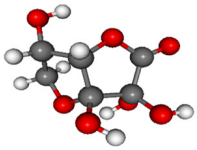

B2
(–760.239710 hartree)

Fig. 2. Optimal gas-phase B3LYP/6-311++G** geometries of energetically preferred conformations of studied molecules. Conformation **AA(7-OH)** with two intramolecular hydrogen bonds was used for the evaluation of *PA* and pK_a values. Values in parentheses represent the corresponding electronic energies in hartree.

dissociation. For further thermodynamic calculations of the most stable state and its derivates, geometries of conformer **A** and **B** were selected (see Fig. 2). Thermodynamics of homolytic dissociation of chemical bonds can be estimated from the bond dissociation enthalpies (BDEs) which represent a one-step mechanism of hydrogen atom transfer (HAT). This quantity can be calculated as

$$\mathrm{BDE} = H(\mathrm{A}^{\bullet}) + H(\mathrm{H}^{\bullet}) - H(\mathrm{A—H}) \qquad (1)$$

where $H(\mathrm{A}^{\bullet})$ stands for the total enthalpy of formed radical, $H(\mathrm{H}^{\bullet})$ for total enthalpy of hydrogen atom, and H(A—H) is the total enthalpy of the molecule. The total gas-phase enthalpy of hydrogen atom is –1306 kJ mol^{-1} and the contribution of the solvation enthalpy in water is –4 kJ mol^{-1} (Rimarčík et al., 2010).

For reference L-ascorbic acid (see Tab. 2), the gas-phase BDEs for possible radical structures formed from the hydroxyl groups and tertiary methyl group are in the range of 332 kJ mol^{-1} to 450 kJ mol^{-1}. The values of C3—OH and C5—H are in the best agreement with the available experimental value of 326.4 kJ mol^{-1} (Warren et al., 2010). The homolytic dissociation of hydroxyl groups located at the side 1,2-dihydroxylethyl substituent is less preferable. For **AA** and **A** molecules, the gas-phase BDEs are higher by about 100 kJ mol^{-1}. Interestingly, molecule **A** gas-phase BDEs for homolytic splitting of C5—H bond is 342 kJ mol^{-1}. The energetically preferred homolytic cleavage of C—H

Tab. 1. Calculated B3LYP/6-311++G** gas-phase, SMD and IEF-PCM intramolecular hydrogen bond lengths of most stable conformers.

		R(O···H)/Å		
	Substituent	**Gas-phase**	**SMD**	**IEF-PCM**
AA	**C3OH···OC4**	2.599	2.688	2.649
	C4OH···OC7	1.757	1.661	1.689
	C6OH···O1	2.214	2.392	2.295
A	**C6OH···OC4**	2.285	2.270	2.470
	C6OH···OC7	2.818	2.724	2.715
B	**C3OH···OC7**	2.422	2.762	2.525
	C3OH···O1	2.977	3.111	3.036
	C7OH···O1	2.358	2.452	2.394
	C7OH···OC6B	3.113	3.093	3.157
	C6AOH···OC7	2.273	2.229	2.238
	C6AOH···OC6B	2.672	2.718	2.705
	C6BOH···OC5	2.572	2.718	2.695
	C6BOH···OC6A	2.623	2.531	2.545

bonds was predicted for various Δ 5- and Δ 7-sterols by Lengyel et al. (Lengyel et al., 2012) and Škorňa et al. (Škorňa et al., 2014). Considering the implicit solvent models, the BDE values slightly deviate (1 to 5 kJ mol^{-1}) in most calculations but there are more significant differences (~10 kJ mol^{-1}) in molecule **AA** hydroxyl groups C3—OH and C6—OH, molecule **A** C6—OH and molecule **B** C3—H and C7—OH groups.

Abstraction of hydrogen atom is also possible *via* a two-step mechanism denoted as single electron transfer followed by proton transfer (SET-PT). In the first step, the electron is abstracted from the molecule and the proton transfer reaction results in a cation radical. Thermodynamics of the first step of the SET-PT mechanism is described by ionization potential (IP),

$$IP = H(\text{A—H}^{\bullet+}) + H(e^-) - H(\text{A—H}) \quad (2)$$

where $H(\text{A—H}^{\bullet+})$ is total enthalpy of radical cation, and $H(e^-)$ is enthalpy of electron. The total gas-phase enthalpy of electron is 3.145 kJ mol^{-1} and the contribution of the solvation enthalpy in water is –105 kJ mol^{-1} (Rimarčík et al., 2010).

Predicted gas-phase ionization potential values for **AA** and **A** molecules are 794.3 kJ mol^{-1} and 872.8 kJ mol^{-1}, respectively. The presence of two cyclic moieties in **B** molecule increases the IPs by about 11 kJ mol^{-1}. Entering the solvent models, the values drop to 557.3 kJ mol^{-1} (SMD) and 581.7 kJ mol^{-1} (IEF-PCM). The minimum value appears to be the SMD one. In general, vitamins with higher *IP* values are more susceptible to ionization and they have stronger antioxidant potential (Pandithavidana and Jayawardana, 2019).

Thermodynamics of heterolytic dissociation of chemical bonds can be described using through proton affinity (PA), which is for the anion formation defined as:

$$PA = H(A^-) + H(H^+) - H(\text{A—H}) \quad (3)$$

where $H(A^-)$ is enthalpy of anion and $H(H^+)$ is total enthalpy of proton. The total gas-phase enthalpy of proton is 6.197 kJ mol^{-1} and the contribution of the solvation enthalpy is –1090 kJ mol^{-1} (Rimarčík et al., 2010).

Values collected in Tab. 2 indicate show significant differences in *PA*s between gas-phase and solvent calculations, as expected for the deprotonation mechanism. In case of the **AA** anion with starting geometry including a deprotonated 7-OH group, the resulting calculated geometry belongs to the anion with deprotonated 4-OH group. This proton transfer from 4-OH group to the negatively charged 7-O atom results in the presence of a hydrogen bond in the parent **AA** conformation (see Tab. 1). The stable geometry of **AA(7-O$^-$)** anion was reached

Tab. 2. Ionization potentials (*IP*), bond dissociation enthalpies (*BDE*) and proton affinities (*PA*) calculated for the energetically preferred conformations.

	IP/kJ mol^{-1}			*BDE*/kJ mol^{-1}			*PA*/kJ mol^{-1}		
	Gas	Water		Gas	Water		Gas	Water	
		SMD	IEF-PCM		SMD	IEF-PCM		SMD	IEF-PCM
AA	794	462	498						
A	873	557	582						
B	889	538	580						
AA(3-OH)				332	319	316	1421	109	120
AA(4-OH)				335	333	334	1305	67	61
AA(6-OH)				450	436	435	1472	159	178
AA(7-OH)*				426	432	430	1459	169	179
AA(5-H)				334	341	336	1476	196	200
A(6-OH)				440	432	430	1452	150	164
A(7-OH)				430	430	430	1351	84	89
A(5-H)				342	343	341	1334	80	80
B(3-OH)				429	431	427	1414	150	148
B(6-OH^A)				394	391	385	1406	109	117
B(6-OH^B)				391	390	382	1383	99	105
B(7-OH)				328	316	309	1377	106	108
B(3-H)				387	378	376	1390	121	119
B(8-H)				429	427	425	1533	269	264

*Starting geometry does not include hydrogen bond between C4OH···OC7 atomic pair.

for the conformation with one intramolecular hydrogen bond (see Fig. 1). The calculated gas-phase values for deprotonated hydroxyl groups range from 1305 kJ mol^{-1} to 1472 kJ mol^{-1}. Similarly, as in the case of homolytic dissociation of the hydroxyl group, the energetically preferred dissociation is in the vicinity of the double carbon-carbon bond. The inclusion of solvent leads to rapid decrease of proton affinities; B3LYP values change from 67 kJ mol^{-1} to 169 kJ mol^{-1} (SMD) and 61 kJ mol^{-1} to 179 kJ mol^{-1} (IEF-PCM). Theoretical calculations for the **AA** molecule predict deprotonation as more energetically preferable for the 4-OH than for the 3-OH group. A possible explanation is related to the effect of π-electron conjugation occurring along the *trans*-oriented bonds O═C2—C3═C4—OH. In general, such conjugated groups are more likely to deprotonate (Wyman, 1955).

Formation of molecule **A** anion is most convenient through tertiary **A(5-H)** group (80 kJ mol^{-1} in solvent). Hydrogen atom at the C5 atom (5-H) is more acidic than the other hydroxyl groups due to the classic withdrawing effect of three neighboring keto groups present in the molecule. Also, *PA* values of chain **A(6-OH)** and **A(7-OH)** groups show differences; the latter one is energetically preferred due to steric effects. In case of molecule **B**, both **B(6-OH)** groups show the lowest values of *PA*. Comparing tertiary **B(3-H)** and **B(8-H)** groups**,** the first exhibits lower *PA* value due to the presence of a hydroxyl group at the sp^3 C3 atom.

From the experimental point of view, the acid dissociation constant, or its logarithmic expression (pK_a), represents a quantitative measure of heterolytic dissociation in solution. The value of pK_a for water can be calculated from the Gibbs energies:

$$pK_a = [\Delta G_{aq}]/(2.303\ RT) = \\ = [G_{aq}(A^-) + G_{aq}(H^+) - G_{aq}(HA)]/(2.303\ RT) \quad (4)$$

where $G_{aq}(A^-)$ represents Gibbs free energy of anion, $G_{aq}(H^+)$ is total Gibbs free energy of proton (–1104.62 kJ mol^{-1}) (Alongi et al., 2010), and $G_{aq}(HA)$ is total Gibbs free energy of the molecule. Symbol R stands for the gas constant and T is temperature. The calculated reaction Gibbs free energies (ΔG_{aq}) and evaluated pK_a values in water are collected in Table 3.

The lowest predicted pK_a value of reference vitamin C is 6.1 (IEF-PCM) and 7.3 (SMD) and it is related to the deprotonation of the 4-OH group. The reported experimental pK_a values of this weak dibasic acid are 4.25 and 11.79 (Combs, 2008). Probably the lower experimental acidity of deproteinized ascorbic acid is related to the occurrence of resonance structures of the ascorbate anion and the natural limitations of the implicit cavity solvent model. In case of dehydroascorbic acid (**A**), the lowest pK_a values of 8.7 (SMD) and 9.3 (IEF-PCM) are due to the proton abstraction from the C5 atom. The reported experimental value measured in water is ∼9 (Gutierrez, 1988). Unfortunately, their used experimental technique was not able to identify the abstracted bond. Consequently, compared with the available experimental data, proton abstraction from C5—H is the most probable. Influence of keto groups present in the molecule was assumed. It seems that the SMD model overtakes IEF-PCM model by giving the results in better compliance with literature. For molecule **B**, the lowest pK_a values are 13.1 (SMD) and 13.7 (IEF-PCM) corresponding with general pK_a values of aliphatic alcohols (Takahashi et al., 1971). The lowest value is related to the proton abstraction from the **6-OH^B** hydroxyl group, but the differences between the theoretical pK_a values for C3—H and 6O—H^A are minimal. Therefore, in sufficiently basic environment, the possibility of heterolytic dissociation from the mentioned tertiary hydrogen occurs. On the other hand, C8—H group does not share a carbon atom with a hydroxyl group and thus higher pK_a of 42.4 was measured (SMD). The value is regular for tertiary bonds in cyclic organic compounds (Shen et al., 2007).

Tab. 3. Reaction Gibbs energies and pK_a values calculated for water environment.

	ΔG/kJ mol^{-1}		pK_a	
	SMD	**IEF-PCM**	**SMD**	**IEF-PCM**
AA(3-OH)	85.1	94.8	14.9	16.6
AA(4-OH)	41.8	35.0	7.3	6.1
AA(6-OH)	136.0	152.7	23.8	26.7
AA(7-OH)*	163.7	187.0	28.7	32.8
AA(5-H)	168.4	168.9	29.5	29.6
A(6-OH)	123.9	139.4	21.7	24.4
A(7-OH)	63.3	70.5	11.1	12.4
A(5-H)	49.6	52.7	8.7	9.3
B(3-OH)	129.9	127.3	22.8	22.3
B(6-OH^A)	84.9	92.0	14.9	16.1
B(6-OH^B)	74.9	78.5	13.1	13.7
B(7-OH)	83.6	85.2	14.7	14.9
B(3-H)	93.8	90.3	16.4	15.8
B(8-H)	242.3	236.8	42.4	41.5

*Starting geometry does not include hydrogen bond between C4OH···OC7 atomic pair.

Conclusion

Conformation analysis of dehydroascorbic acid and its bicyclic form was performed using the B3LYP DFT functional for the gas-phase and two implicit

solvent models, i.e., IEF-PCM and SMD. For the energetically preferred conformations, the bond dissociation enthalpies, ionization potentials and proton affinities were calculated; values of pK_a were predicted for water environment. Theoretical results indicate that the investigated bicyclic metabolic products of vitamin C can possess small radical scavenging ability. Furthermore, our calculations for vitamin C and dehydroascorbic acid indicate that, from the thermodynamic point of view, the preferable way of homolytic and heterolytic dissociation includes the C—H bond. Therefore, the antioxidant activity mechanism of L-ascorbic acid and its oxidated form should be possible through bonds of tertiary hydrogen groups.

Acknowledgement

The work has been supported by the Slovak Research and Development Agency (APVV-15-0053) and VEGA 1/0504/20 and 1/0461/21. We are grateful to the HPC centre at the Slovak University of Technology in Bratislava, which is a part of the Slovak Infrastructure of High Performance Computing (SIVVP project, ITMS code 26230120002, funded by the European Region Development Funds, ERDF) for the computational time and resources made available. Authors would like to thank Dr. Martin Michalík for his technical support and discussion.

References

Alongi KS, Shields GC (2010) Ann. Rep. Comp. Chem. 6: 113—138.

Becke AD (1988) Phys. Rev. A 38: 3098—3100.

Bendich A, Langseth L (1995) J. Am. Coll. Nutr. 14: 124—136.

Bielski BHJ, Allen AO, Schwarz HA (1981) J. Am. Chem. Soc. 103: 3516—3518.

Bielski BHJ, Cabelli DE, Arudi RL, Ross AB (1985) J. Phys. Chem. Ref. Data 14: 1041—1100.

Binkley JS, Pople JA, Hehre WJ (1980) J. Am. Chem. Soc. 102: 939—947.

Combs GF Jr., The Vitamins — Fundamental Aspects in Nutrition and Health, New York, Elsevier Academic Press, 2008, ISBN-13:978-0-12-183493-7.

Deakin MR, Kovach PM, Stutts KJ, Wightman RM (1986) Anal. Chem. 58: 1474—1480.

Fisher AJ, Ten Pas RH (1966) Anesth. Analg. 45 (5): 531—534.

Flukiger P, Luthi HP, Portmann S, Weber J (2000—2002) MOLEKEL 4.3, Swiss Center for Scientific Computing, Manno Switzerland.

Frisch MJ, Trucks GW, Schlegel HB, Scuseria GE, Robb MA, Cheeseman JR, Scalmani G, Barone V, Petersson GA, Nakatsuji H, Li X, Caricato M, Marenich AV, Bloino J, Janesko BG, Gomperts R, Mennucci B, Hratchian HP, Ortiz JV, Izmaylov AF, Sonnenberg JL, Williams-Young D, Ding F, Lipparini F, Egidi F, Goings J, Peng B, Petrone A, Henderson T, Ranasinghe D, Zakrzewski VG, Gao J, Rega N, Zheng G, Liang W, Hada M, Ehara M, Toyota K, Fukuda R, Hasegawa J, Ishida M, Nakajima T, Honda Y, Kitao O, Nakai H, Vreven T, Throssell K, Montgomery JA Jr., Peralta JE, Ogliaro F, Bearpark MJ, Heyd JJ, Brothers EN, Kudin KN, Staroverov VN, Keith TA, Kobayashi R, Normand J, Raghavachari K, Rendell AP, Burant JC, Iyengar SS, Tomasi J, Cossi M, Millam JM, Klene M, Adamo C, Cammi R, Ochterski JW, Martin RL, Morokuma K, Farkas O, Foresman JB, Fox DJ (2016) Gaussian 16, Revision B.01, Gaussian, Inc., Wallingford CT.

Gutierrez PL (1988) Drug Met. Rev. 19: 319—343.

Lengyel J, Rimarčík J, Vagánek A. Fedor J, Lukeš V, Klein E (2012) Food. Chem. 133: 1435—1440.

Kurata T, Nishikawa Y (2000) Biosci. Biotechnol. Biochem. 64: 1651—1655.

Lee C, Yang W, Parr RG (1988) Phys. Rev. B 37: 785—789.

Merenich AV, Cramer CJ, Truhlar DG (2009) J. Phys. Chem. B 113: 6378—6396.

Michalik M, Lukeš V (2016) Ac. Chim. Slov. 9: 89—94.

Njus D, Kelley PM, Tu YJ, Schlegel HB (2020) F. Rad. Bio. Med. 159: 37—43.

Pandithavidana DR, Jayawardana SB (2019) Molecules 24: 1646.

Rimarčík J, Lukeš V, Klein E, Ilcin M (2010) J. Mol. Struct. 952: 25—30.

Shen K, Fu Y, Li JN, Liu L, Guo QX (2007) Tetrahedron 63: 1568—1576.

Škorňa P, Lengyel J, Rimarčík J, Klein E (2014) Comp. Theor. Chem. 1038: 26—32.

Takahashi S, Cohen LA, Miller HK, Peake EG (1971) J. Org. Chem. 36: 1205—1209.

Tomasi J, Mennucci B, Cammi R (2005) Chem. Rev. 105: 2999—3093.

Tu YJ, Nius D, Schlegel HB (2017) Org. Biomol. Chem. 15: 4417—4431.

Warren JJ, Tronic TA, Mayer JM (2010) Chem. Rev. 110: 6961—7001.

Wilson JX (2002) FEBS Lett. 527: 5—9.

Wyman GM (1955) Chem. Rev. 55: 625—657.

sciendo

Quantum-chemical studies of rutile nanoparticles toxicity II. Comparison of B3LYP and PM6 data

Martin Breza

Department of Physical Chemistry, Faculty of Chemical and Food Technology, Slovak University of Technology, Radlinského 9, 812 37 Bratislava, Slovak Republic
martin.breza@stuba.sk
In the memory of Professor Rudolf Zahradník (1928–2020).

Abstract: The relation between copper atomic charges and metal-ligand interaction energies obtained by PM6 and DFT-B3LYP methods for cytotoxicity prediction of model rutile nanoparticles $[Ti_{40}O_{124}H_{81}]^{7-}$, $[Ti_7O_{28}H_{26}]^{2-}$, $[Ti_2O_{10}H_{10}]^{2-}$, $[Ti_7O_{30}H_{30}]^{2-}$ and their Cu(II) complexes is investigated. Except for Mulliken charges, very good statistical parameters were obtained for the linear relation between the results obtained by both methods if standard accuracy of quantum-chemical calculations is achieved.

Keywords: DFT — B3LYP and PM6 methods, linear regression, metal-ligand interaction energy, population analyses, statistical parameters

Introduction

Biochemical and molecular mechanisms of cytotoxicity include oxidative stress-induced cellular events and alteration of the pathways pertaining to intracellular calcium homeostasis (Huang et al., 2017). Physicochemical properties of nanoparticles (surface, size, morphology, dissolution of ions etc.) influence their interaction with cells and, thus, their overall potential toxicity. Their shape also affects the levels of toxicity. In general, rod shaped nanoparticles are more toxic than the spherical ones (Hsiao and Huang, 2011; Lee et al., 2014; Forest et al., 2017). However, the reason of this phenomenon has not been fully elucidated yet.

Theoretical model studies based on quantum-chemical calculations are capable to shed more light on this phenomenon. Cytotoxicity of nanoparticles can be predicted using the method originally elaborated for the estimation of relative activity of antioxidants (Alagona and Ghio, 2009a, 2009b; Mammino, 2013; Tsiepe et al., 2015; Puškárová and Breza, 2016, 2017; Jelemenská and Breza, 2021) based on their copper coordination ability (metal ion affinity, MIA) and electron density transfer to a hypothetical Cu(II) probe. According to this method, spin density of the Cu^{2+} cation upon ligand coordination decreases whereas the ligand spin density approaches 1. Thus, the ligand is oxidized to a radical cation ($Ligand^{\bullet+}$) while Cu(II) is reduced to Cu(I). In agreement with experimental investigations, the higher antioxidant activity of individual compounds and their reaction sites can be attributed to higher MIA values and higher reducing character towards Cu(II).

Using the semiempirical PM6 method, the above treatment was used in the toxicity study (Breza and Šimon, 2019) of the $[Ti_{40}O_{124}H_{81}]^{7-}$ model cluster based on an idealized rod-like $[Ti_{40}O_{124}]^{88-}$ structure of ca 1.5 nm × 1 nm × 1 nm in size with all monovalent O atoms being protonated. Its planes are significantly deformed due to protonation and the original Ti hexacoordination is sometimes reduced to pentacoordination. Relative toxicity of individual Ti centers in this rutile nanoparticle, as evaluated by the electron density transfer to a Cu^{2+} probe, has maximal values at the pentacoordinated corner and hexacoordinated edge Ti centers with three Ti—OH bonds. However, these centers exhibit the lowest negative interaction energies which can be compensated by the significantly better accessibility of the corner Ti center compared with that of the remaining ones. Ti centers with the most negative interaction energy parameters exhibit the lowest extent of electron density transfer to the Cu^{2+} probe. Rutile nanoparticles destruction starts at the pentacoordinated Ti face centers.

According to B3LYP calculations (Breza and Šimon, 2020), electron density removal from model rutile nanoparticles, such as spherical $^1[Ti_7O_{28}H_{26}]^{2-}$, $^1[Ti_2O_{10}H_{10}]^{2-}$ and rod-like $^1[Ti_7O_{30}H_{30}]^{2-}$, is accompanied with significant changes in their structure and may cause their degradation. Terminal hydroxyls seem to be more reactive than the bridging ones as indicated by their interaction energies. Spherical structures are more reactive than the rod-like chains of (nearly)

the same size. Reverse relation holds for the degree of their toxicity as indicated by the extent of electron density transfer to the Cu^{2+} probe. The experimentally observed higher cytotoxicity of the rod-like nanoparticles in comparison with the spherical ones (see above) can be explained by the higher electron density transfer to the interacting living cells.

Semiempirical methods of quantum chemistry are suitable for the study of large model systems (hundreds of atoms at our available facilities). On the other hand, they are believed, in general, to be less accurate than the *ab initio* or DFT methods. Therefore, the question arises whether the results — or, more exactly, their trends — obtained by both above mentioned studies (Breza and Šimon, 2019, 2020) are comparable. In our recent study, the results (atomic charges and interaction energies) obtained by the PM6 method are re-calculated at the B3LYP level of theory and *vice versa*. Due to technical reasons, fixed original geometries of the systems under study are used for our quantum-chemical calculations. The aim of our study is to compare the trends in the data obtained at both levels of theory for the same geometries of the systems under study.

Method

Single point calculations of the PM6 optimized geometries (Breza and Šimon, 2019) of $^{1}[Ti_{40}O_{124}H_{81}]^{7-}$ and $^{2}[Ti_{40}O_{124}H_{81}Cu]^{5-}$ (model I series, denoted by spin multiplicity as the left superscript) were performed at the DFT level of theory using B3LYP hybrid functional (Becke, 1993) with standard LANL2DZ pseudopotentials and basis sets (Dunning, 1977; Hay and Wadt, 1985) for all atoms. Atomic charges were evaluated in terms of the Mulliken population analysis (MPA) (Mulliken, 1955) and natural population analysis (NPA) (Reed et al., 1988).

Single point calculations of the B3LYP optimized geometries (Breza and Šimon, 2020) of $^{1}[Ti_{7}O_{28}H_{26}]^{2-}$, $^{1}[Ti_{2}O_{10}H_{10}]^{2-}$, $^{1}[Ti_{7}O_{30}H_{30}]^{2-}$, $^{2}[Ti_{7}O_{28}H_{26}Cu]^{0}$, $^{2}[Ti_{2}O_{10}H_{10}Cu]^{0}$ and $^{2}[Ti_{7}O_{30}H_{30}Cu]^{0}$ (model II series) were performed at the semiempirical level of theory using the PM6 method (Stewart, 2007). Atomic charges were evaluated in terms of the Mulliken population analysis (MPA) (Mulliken, 1955).

All the above calculations were performed using the Gaussian09 program package (Frisch et al., 2013). Atomic polar tensor (APT) derived charges (Cioslowski, 1989) demand vibrational analysis to be performed and therefore are unusable in single point calculations. Metal-ligand interaction energy $\Delta_{int}E$ is defined as

$$\Delta_{int}E = E_{Complex} - E_{L} - E_{ion} \quad (1)$$

where $E_{Complex}$ and E_{L} are energies of the $^{2}[L...Cu]^{q+2}$ complex and of the isolated rutile nanoparticle $^{1}L^{q}$ model cluster, respectively, and E_{ion} is energy of the isolated $^{2}Cu^{2+}$ ion (Alagona and Ghio, 2009a, 2009b; Mammino, 2013; Tsiepe et al., 2015; Puškárová and Breza, 2016, 2017; Jelemenska and Breza, 2021).

Similarity of the trends in the results obtained by both quantum-chemical methods can be evaluated by the linear relation:

$$Y = a_1X + a_0 \quad (2)$$

where X and Y are values (i.e., atomic charges and interaction energies) obtained by PM6 and B3LYP methods, respectively, a_1 and a_0 are linear regression parameters. The goodness of fit is evaluated by standard statistical parameters such as the standard deviations of regression parameters and the coefficient of determination R^2.

Results and discussion

a) Model systems I

In the $^{1}[Ti_{40}O_{124}H_{81}]^{7-}$ model cluster (Breza and Šimon, 2019), various Ti centers can be distinguished according to their bonding to hydroxyl groups (OH) and bridging oxygens (O_b) between two Ti atoms. These centers can be divided into three groups and their toxicity can be estimated by neighboring Cu^{2+} probes in the PM6 optimized $^{2}[Ti_{40}O_{124}H_{81}Cu]^{5-}$ model systems as follows (Fig. 1):

i) At the rod corners, only pentacoordinated $Ti(OH)_3(O_b)_2$ centers are found (model I-A).
ii) Rod edges contain either hexacoordinated $Ti(OH)_3(O_b)_3$ (model I-B1), $Ti(OH)_2(O_b)_4$ (model I-B2) and $Ti(OH)(O_b)_5$ (model I-B3) centers or pentacoordinated $Ti(OH)_4(O_b)$ (model I-B4), $Ti(OH)_3(O_b)_2$ (model I-B5) and $Ti(OH)_2(O_b)_3$ (model I-B6) centers.
iii) Rod faces have hexacoordinated $Ti(OH)(O_b)_5$ (model I-C1) or pentacoordinated $Ti(OH)(O_b)_4$ (model I-C2) centers.

Copper atomic charges and interaction energies of model systems I (Fig. 1) are presented in Figs. 2—4 and Table A1 of Appendix. It must be mentioned that DFT calculations of $^{1}[Ti_{40}O_{124}H_{81}]^{7-}$ and $^{2}[Ti_{40}O_{124}H_{81}Cu]^{5-}$ systems face serious technical problems. It was not possible to obtain standard convergence accuracy (10^{-8} root-mean-square change in the density matrix). In most cases, the accuracy was reduced by one or two orders only but in two cases (I-B3 and I-C2 systems, denoted

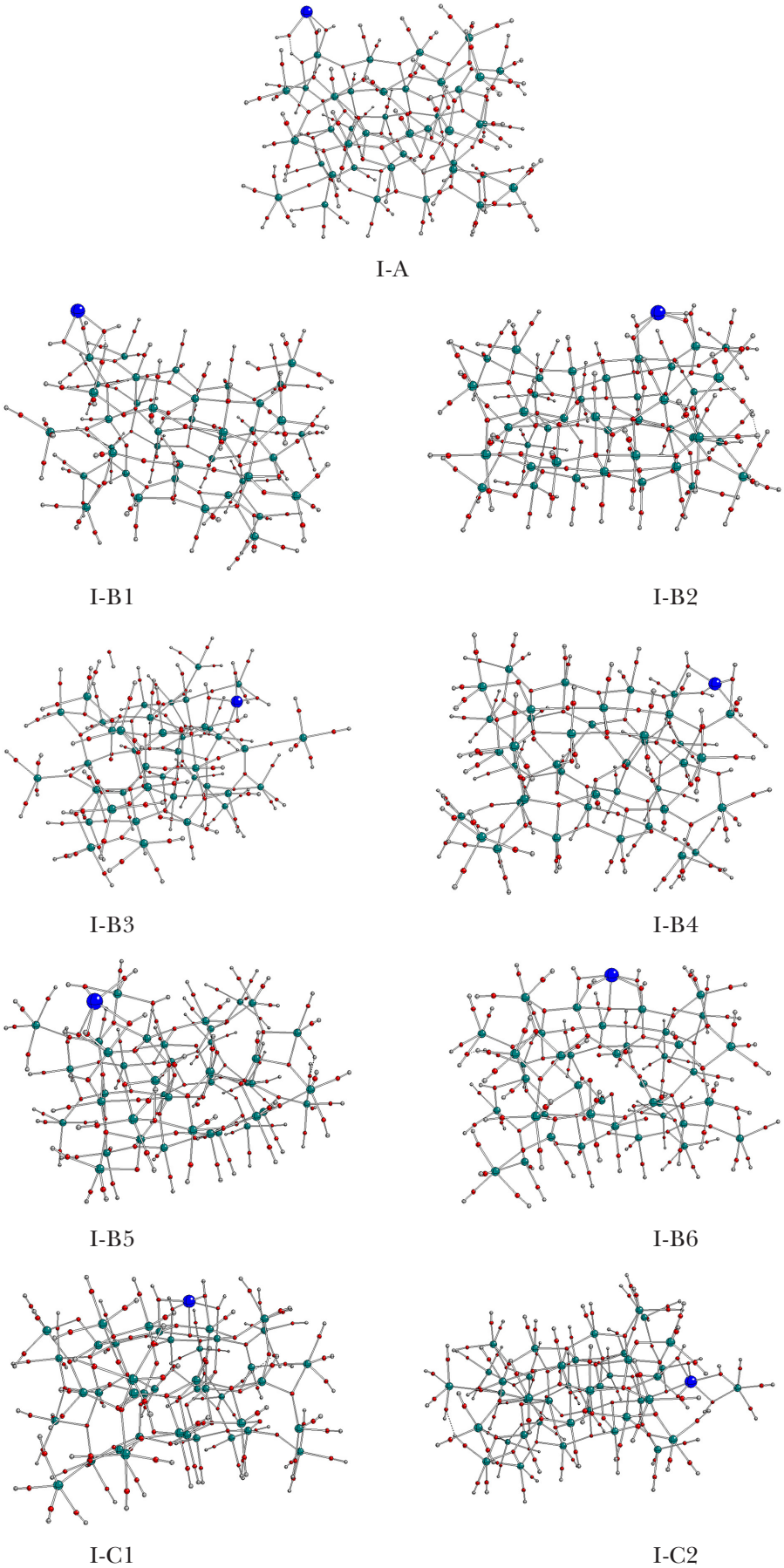

Fig. 1. PM6 optimized geometries of $[Ti_{40}O_{124}H_{81}Cu]^{5-}$ model systems (Ti – green, O – red, H – grey, Cu – blue) (Breza and Šimon, 2019).

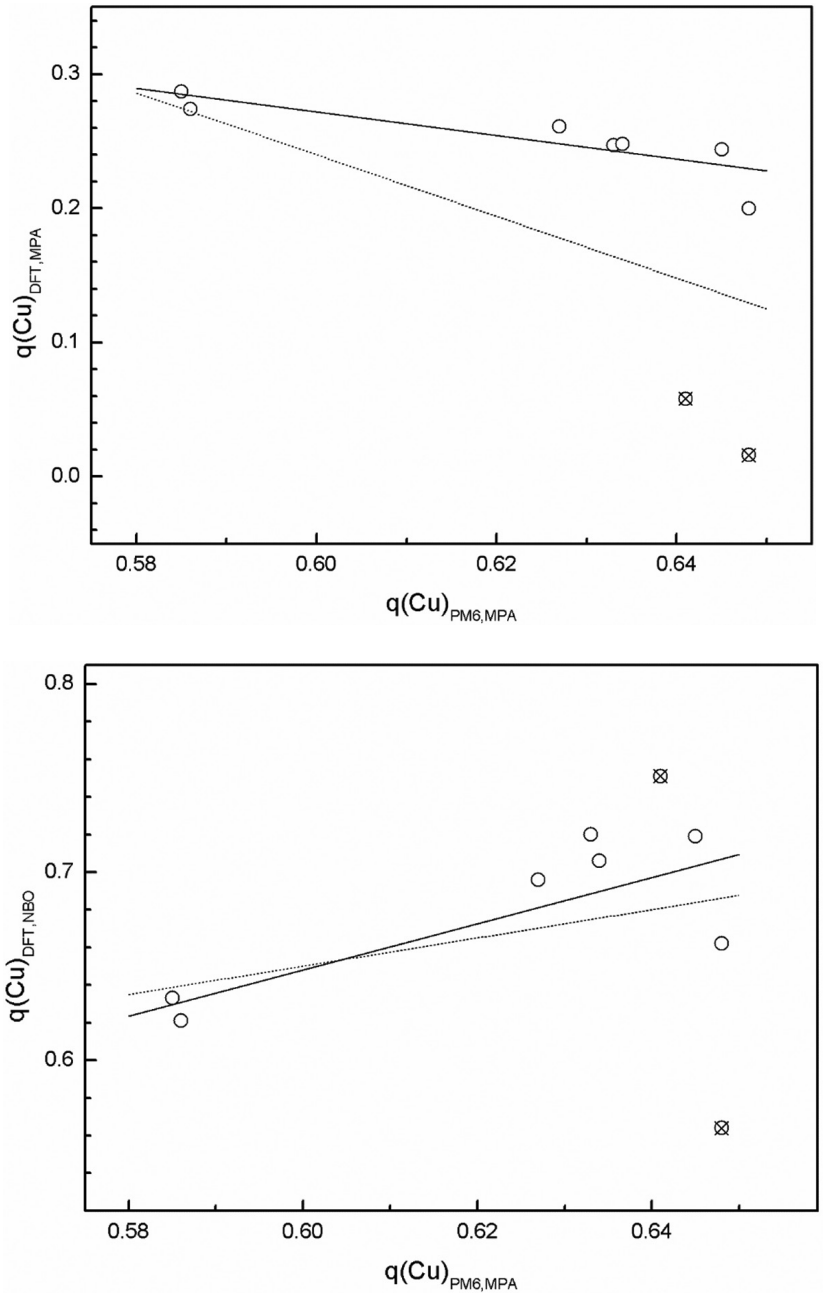

Fig. 2. Plots of MPA (top) and NBO (bottom) charges of Cu obtained by the DFT-B3LYP method *vs* MPA charges of Cu obtained by the PM6 method for ^{2} $[Ti_{40}O_{124}H_{81}Cu]^{5-}$ systems. Dashed and full lines correspond to linear regression for all systems and for all but I-B3 and I-C2 systems (crossed circles), respectively.

by crossed circles in Figs. 2—4), accuracy reduction by four orders was achieved. Therefore, linear regression according to Eq. (2) is presented for all systems and, alternatively, if the two least accurate systems were omitted.

Unlike the NBO charges of copper atoms obtained at the B3LYP level of theory, the MPA ones exhibit reverse trends and decrease with the increasing MPA and APT charges obtained by the semiempirical PM6 method (Table 1, Figs. 2—3). Nevertheless, poor statistical parameters contradict to possible proportionality between copper charges obtained at both levels of theory within the model systems of the I series.

Interaction energy data obtained by the B3LYP and PM6 methods show correct trend only after omitting two least accurate results (I-B3 and I-C2 systems) but their relation also exhibits poor statistical parameters (Table 1, Figs. 4).

Poor statistical parameters of the $^{2}[Ti_{40}O_{124}H_{81}Cu]^{5-}$ systems can be partially ascribed to insufficient accuracy of their B3LYP calculations. Small charge

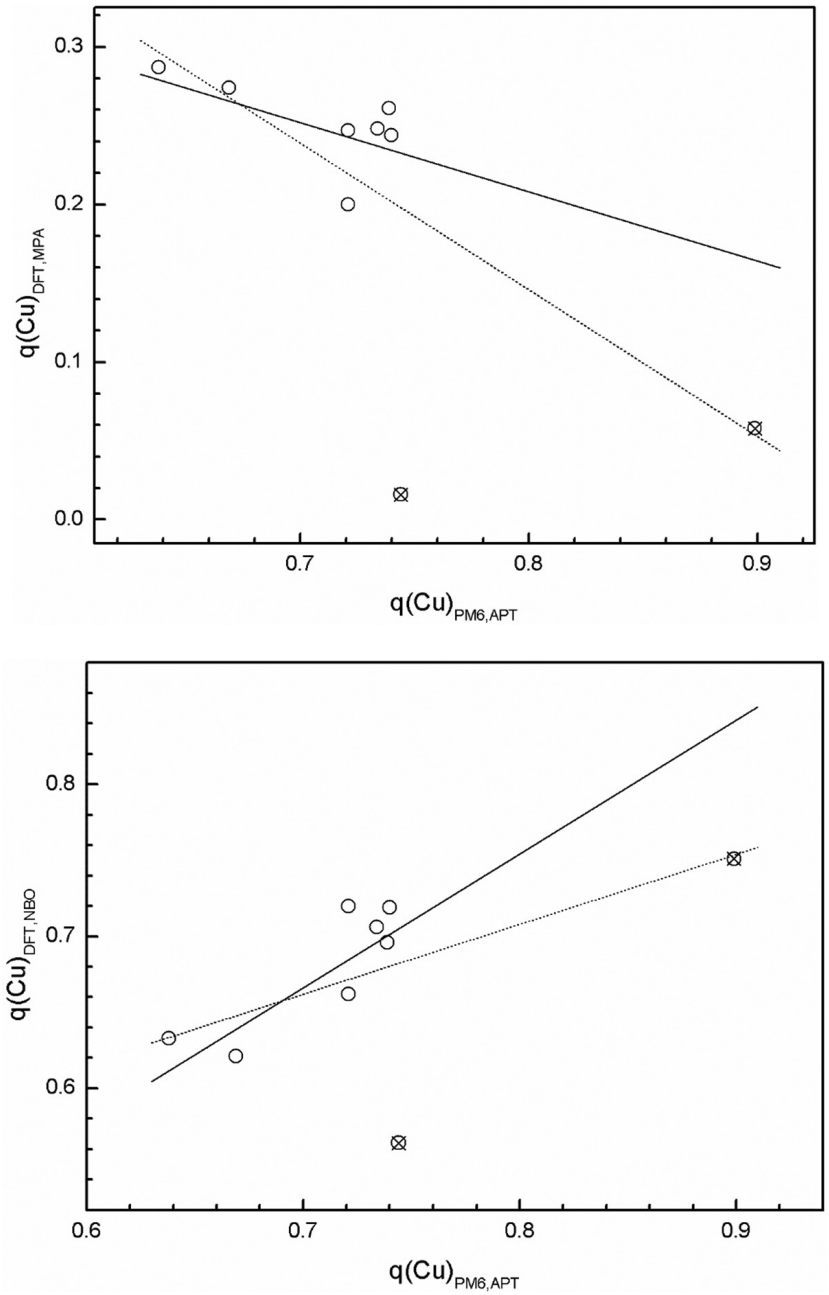

Fig. 3. Plots of MPA (top) and NBO (bottom) charges of Cu obtained by the DFT-B3LYP method *vs* APT charges of Cu obtained by the PM6 method for $^{2}[Ti_{40}O_{124}H_{81}Cu]^{5-}$ systems. Dashed and full lines correspond to linear regression for all systems and for all but I-B3 and I-C2 systems (crossed circles), respectively.

and interaction energy differences between individual model systems near their accuracy limits contribute to the trend looseness as well.

b) Model systems II

The nearly spherical structure of $^{1}[Ti_7O_{28}H_{26}]^{2-}$ (Breza and Šimon, 2020) consists of a single TiO_6 octahedron surrounded by six lateral TiO_6 octahedra. In $^{2}[Ti_7O_{28}H_{26}Cu]^{0}$ model systems, the Cu^{2+} ion is next to the terminal hydroxyl (model II-A1a) or the bridging hydroxyl (models II-A2a and II-A2b) groups (see Fig. 5).

Rod-like chain structures $^{1}[Ti_2O_{10}H_{10}]^{2-}$ and $^{1}[Ti_7O_{30}H_{30}]^{2-}$ (Breza and Šimon, 2020) consist of TiO_6 octahedra bound by double μ-OH bridges as the single bridged structures disintegrate after protonation. In the dimeric $^{2}[Ti_2O_{10}H_{10}Cu]^{0}$ and heptameric $^{2}[Ti_7O_{30}H_{30}Cu]^{0}$ chains, the Cu^{2+} ion is placed next to the terminal hydroxyl (models II-B1a to II-B1c, and II-C1a to II-C1h) or the bridg-

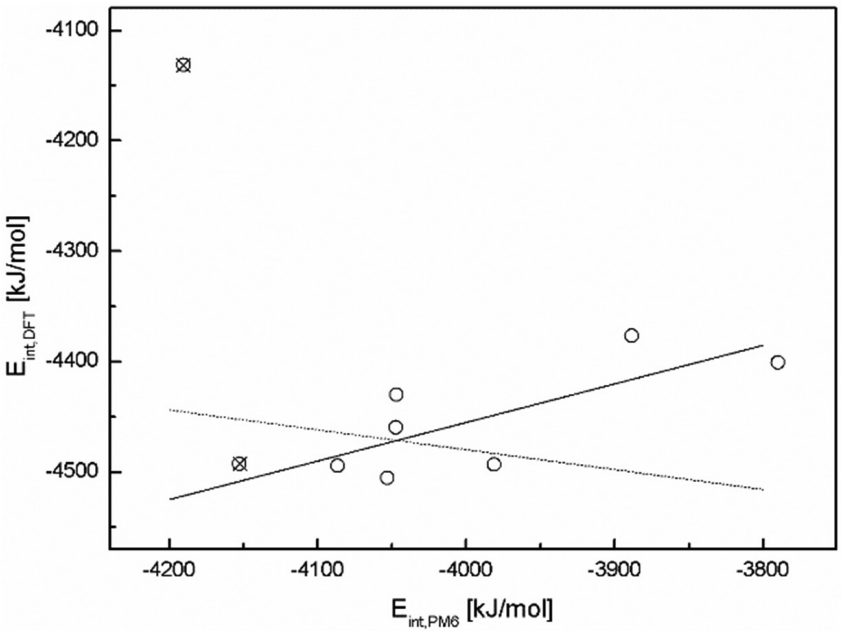

Fig. 4. Plot of interaction energies obtained by the DFT-B3LYP method *vs* the PM6 method for $^{2}[Ti_{40}O_{124}H_{81}Cu]^{5-}$ systems. Dashed and full lines correspond to linear regression for all systems and for all but I-B3 and I-C2 systems (crossed circles), respectively.

Tab. 1. Regression parameters (a_1, a_0) of Eq. (2) with standard deviations for model systems I (see Fig. 1) and the coefficient of determination (R^2) for the dataset consisting of N components.

N	Y	X	a_1	a_0	R^2
9	$q(Cu)_{DFT,MPA}$	$q(Cu)_{PM6,MPA}$	–2.3 ±1.2	1.62 ±0.77	0.23063
	$q(Cu)_{DFT,NBO}$	$q(Cu)_{PM6,MPA}$	0.75 ±0.86	0.20 ±0.54	0.02964
	$q(Cu)_{DFT,MPA}$	$q(Cu)_{PM6,APT}$	–0.93 ±0.38	0.89 ±0.28	0.39006
	$q(Cu)_{DFT,NBO}$	$q(Cu)_{PM6,APT}$	0.46 ±0.26	0.34 ±0.19	0.20839
	$E_{int,DFT}$	$E_{int,PM6}$	–0.18 ±0.35	–5200 ±1400[b)]	0.09858
7[a)]	$q(Cu)_{DFT,MPA}$	$q(Cu)_{PM6,MPA}$	–0.88 ±0.25	0.80 ±0.16	0.64979
	$q(Cu)_{DFT,NBO}$	$q(Cu)_{PM6,MPA}$	1.23 ±0.42	–0.09 ±0.26	0.55334
	$q(Cu)_{DFT,MPA}$	$q(Cu)_{PM6,APT}$	–0.44 ±0.24	0.56 ±0.17	0.27226
	$q(Cu)_{DFT,NBO}$	$q(Cu)_{PM6,APT}$	0.88 ±0.24	0.05 ±0.17	0.67224
	$E_{int,DFT}$	$E_{int,PM6}$	0.35 ±0.14	–3100 ±560 [b)]	0.46067

Remarks:

[a)]I-B4 and I-C2 models omitted

[b)]in kJ/mol units

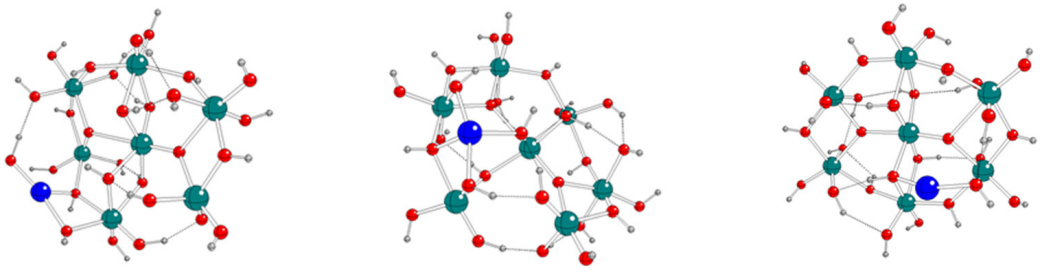

II-A1a II-A2a II-A2b

Fig. 5. B3LYP optimized geometries of $^{2}[Ti_7O_{28}H_{26}Cu]^{0}$ model systems (see Fig. 1 for atom notations) (Breza and Šimon, 2020).

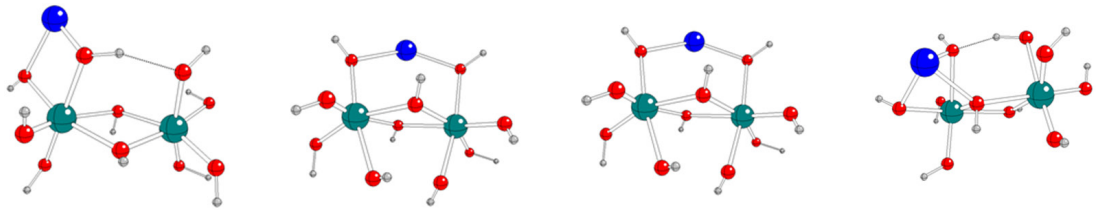

II-B1a II-B1b II-B1c II-B2a

Fig. 6. B3LYP optimized geometries of $^{2}[Ti_2O_{10}H_{10}Cu]^{0}$ model systems (see Fig. 1 for atom notations) (Breza and Šimon, 2020).

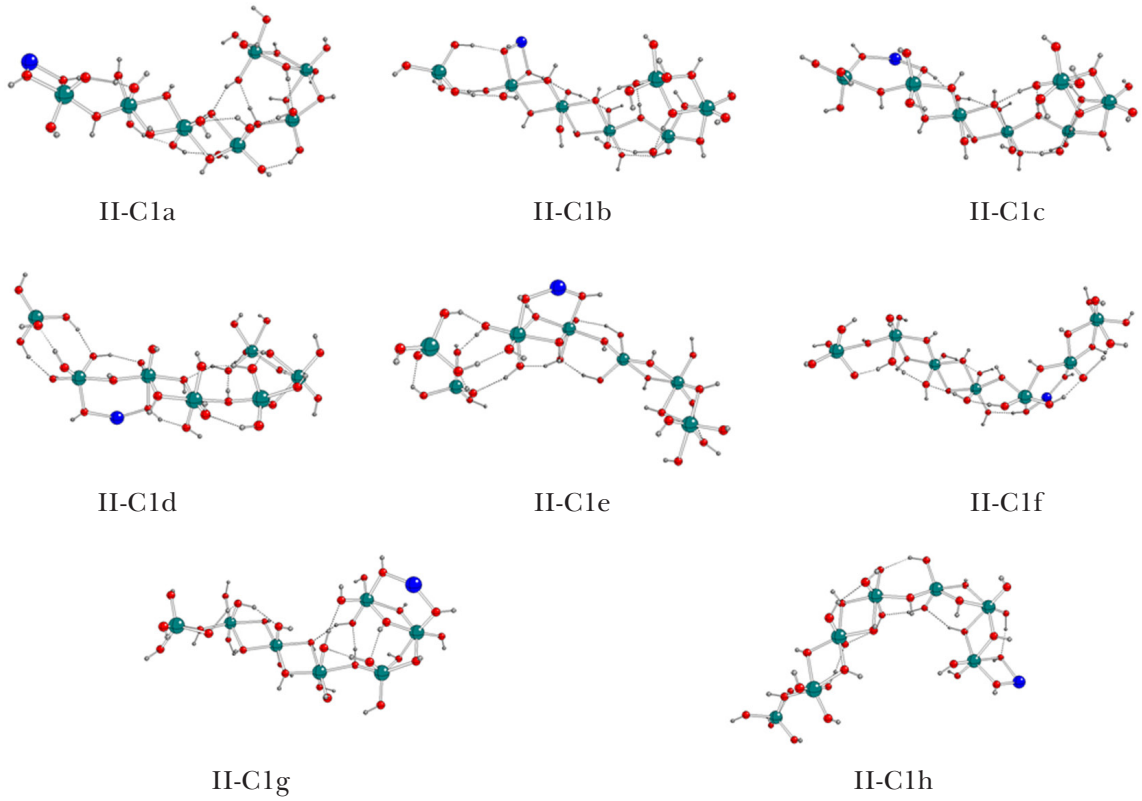

II-C1a II-C1b II-C1c

II-C1d II-C1e II-C1f

II-C1g II-C1h

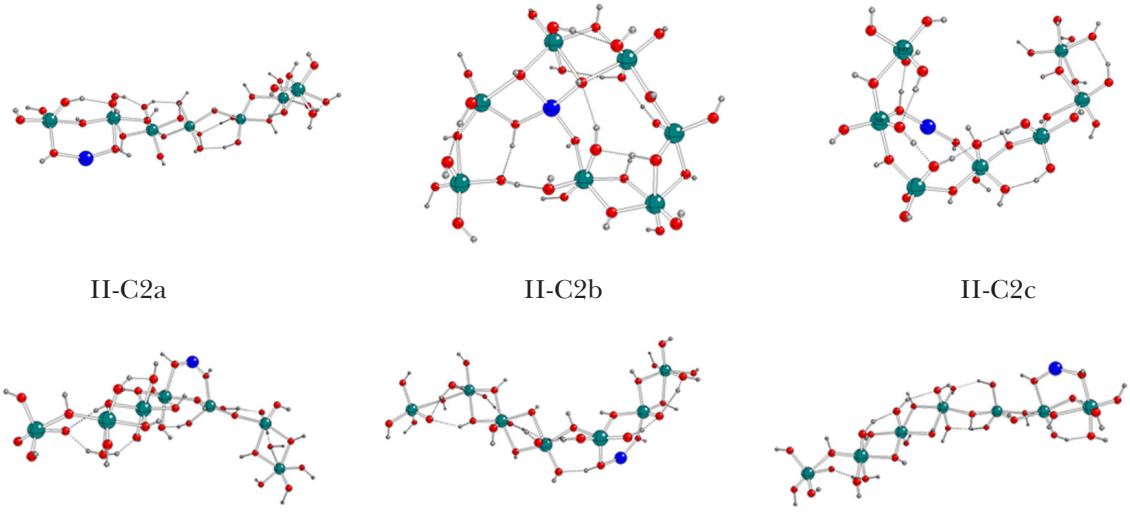

II-C2a II-C2b II-C2c

II-C2d II-C2e II-C2f

Fig. 7. B3LYP optimized geometries of $^{2}[Ti_7O_{30}H_{30}Cu]^{0}$ model systems (see Fig. 1 for atom notations) (Breza and Šimon, 2020).

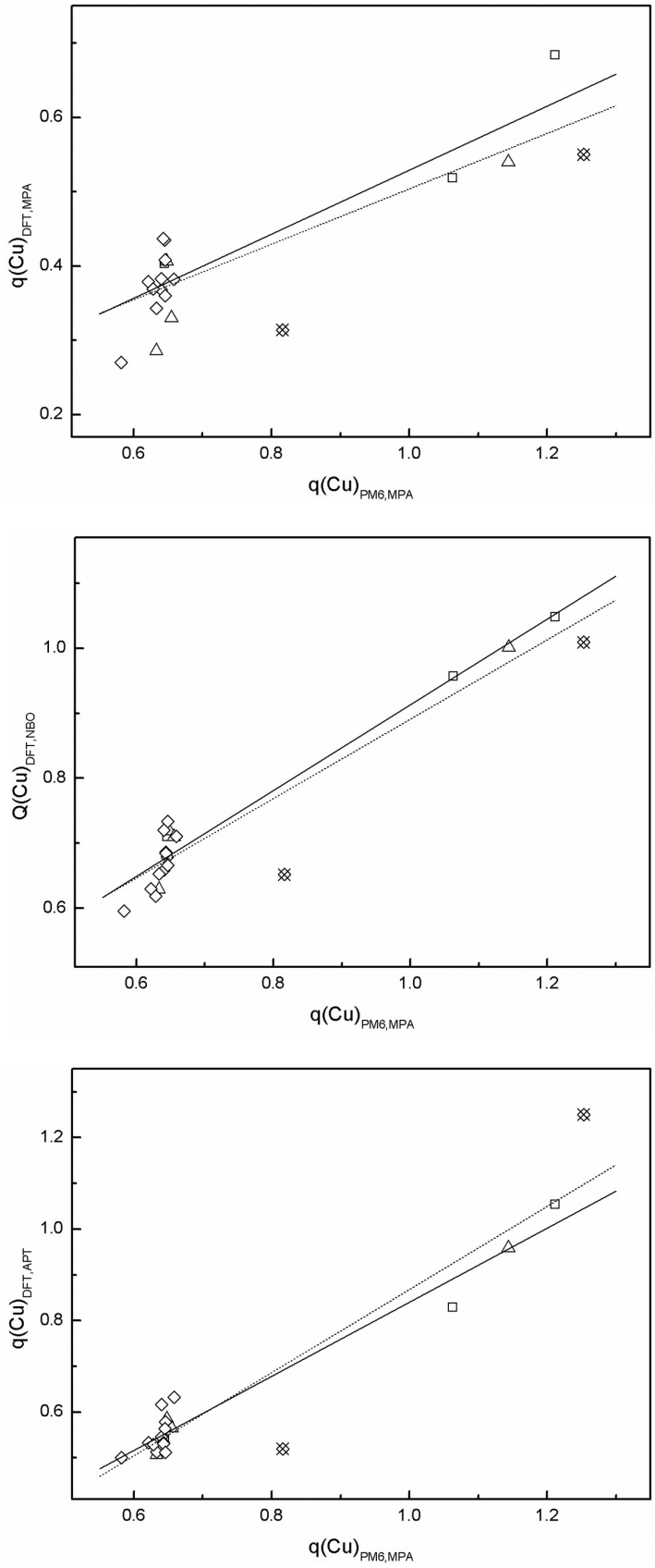

Fig. 8. Plots of MPA (top), NBO (middle) and APT (bottom) charges of Cu obtained by the DFT-B3LYP method *vs* MPA charges of Cu obtained by the PM6 method for $^{2}[Ti_7O_{28}H_{26}Cu]^{0}$ (squares), $^{2}[Ti_2O_{10}H_{10}Cu]^{0}$ (triangles), and $^{2}[Ti_7O_{30}H_{30}Cu]^{0}$ (diamonds) systems. Dashed and full lines correspond to linear regression for all systems and for all but II-C1e and II-C2b systems (crossed diamonds), respectively.

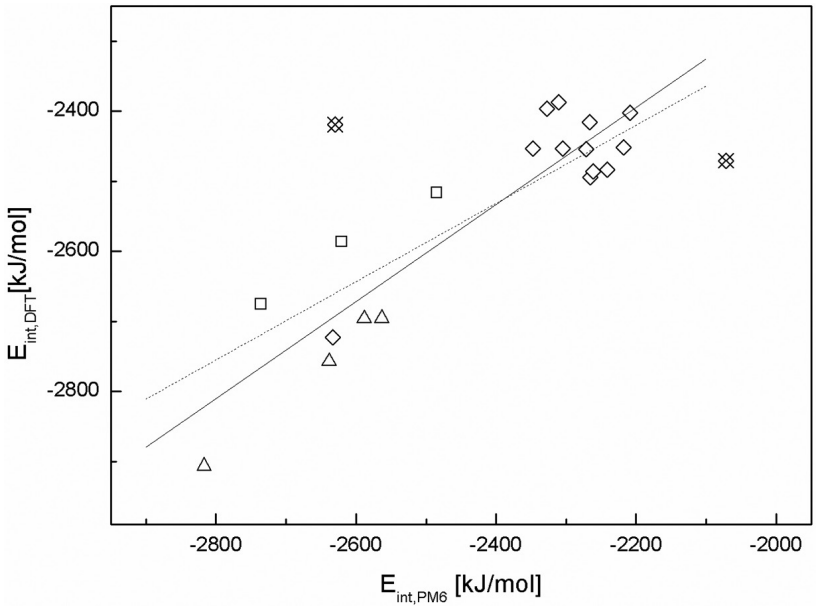

Fig. 9. Plot of interaction energies obtained by the DFT-B3LYP method *vs* the PM6 method for $^2[Ti_7O_{28}H_{26}Cu]^0$ (squares), $^2[Ti_2O_{10}H_{10}Cu]^0$ (triangles), and $^2[Ti_7O_{30}H_{30}Cu]^0$ (diamonds) systems. Dashed and full lines correspond to linear regression for all systems and for all but II-C1e and II-C2b systems (crossed diamonds), respectively.

Tab. 2. Regression parameters (a_1, a_0) of Eq. (2) with standard deviations for model systems II (see Figs. 5—7) and the coefficient of determination (R^2) for the dataset consisting of N components.

N	Y	X	a_1	a_0	R^2
21	$q(Cu)_{DFT,MPA}$	$q(Cu)_{PM6,MPA}$	0.373 ±0.058	0.131 ±0.045	0.66689
	$q(Cu)_{DFT,APT}$	$q(Cu)_{PM6,MPA}$	0.908 ±0.069	–0.040 ±0.054	0.89601
	$q(Cu)_{DFT,NBO}$	$q(Cu)_{PM6,MPA}$	0.610 ±0.046	0.281 ±0.035	0.89888
	$E_{int,DFT}$	$E_{int,PM6}$	0.559 ±0.097	–1190 ±230 [b]	0.61929
19[a]	$q(Cu)_{DFT,MPA}$	$q(Cu)_{PM6,MPA}$	0.431 ±0.059	0.098 ±0.044	0.74127
	$q(Cu)_{DFT,APT}$	$q(Cu)_{PM6,MPA}$	0.809 ±0.044	0.031 ±0.033	0.94896
	$q(Cu)_{DFT,NBO}$	$q(Cu)_{PM6,MPA}$	0.659 ±0.038	0.254 ±0.029	0.94190
	$E_{int,DFT}$	$E_{int,PM6}$	0.693 ±0.075	–870 ±180 [b]	0.82382

Remarks:

[a] II-C1e and II-C2b models omitted

[b] in kJ/mol units

ing hydroxyl (models II-B2a, and II-C2a to II-C2f) groups, respectively (see Figs. 6—7).

Copper atomic charges and interaction energies of model systems II (Figs. 5—7) are presented in Figs. 8—9 and Table A2 of Appendix. Results for II-C1e and II-C2b model systems significantly differ from the remaining $^2[Ti_7O_{30}H_{30}Cu]^0$ ones. Thus, results of the linear regression according to Eq. (2) are presented for all model systems II and the two above mentioned model systems were omitted (Table 2, Figs. 8—9).

Cu charges obtained by the DFT-B3LYP method using NBO and APT treatment increase with their increasing counterparts obtained by the PM6 method with fairly good statistical parameters, especially by omitting the data for II-C1e and II-C2b systems (Table 2, Fig. 8). Nevertheless, significantly worse statistical parameters for the MPA charges obtained by the DFT-B3LYP were obtained.

Slightly worse results (despite the improvement after II-C1e and II-C2b systems omitting) were obtained for interaction energies (Table 2, Fig. 9).

c) All model systems

Despite the 6-311G* basis sets used in the B3LYP calculations of model II systems (Breza and Šimon, 2019), unlike the LANL2DZ ones used in

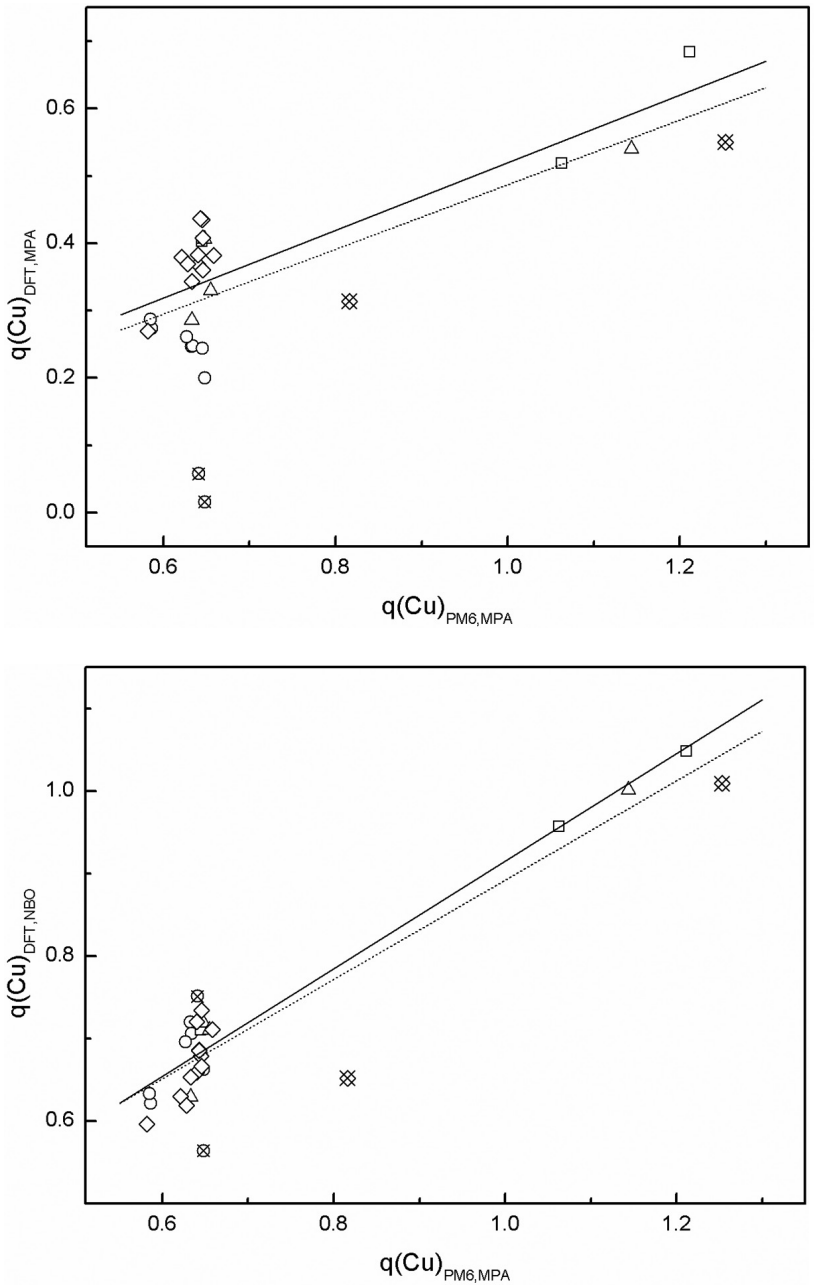

Fig. 10. Plots of MPA (top) and NBO (bottom) charges of Cu obtained by the DFT-B3LYP method *vs* MPA charges of Cu obtained by the PM6 method for $^2[Ti_{40}O_{124}H_{81}Cu]^{5-}$ (circles), $^2[Ti_7O_{28}H_{26}Cu]^0$ (squares), $^2[Ti_2O_{10}H_{10}Cu]^0$ (triangles), and $^2[Ti_7O_{30}H_{30}Cu]^0$ (diamonds) systems. Dashed and full lines correspond to linear regression for all systems and for all but I-B3, I-C2 (crossed circles), II-C1e and II-C2b systems (crossed diamonds), respectively.

this study for model I systems (we were not able to use better basis sets due to technical reasons), correlation of the DFT and PM6 results was attempted for all systems (Table 3, Figs. 10—11). Surprisingly, statistical parameters for Cu charges obtained by the NBO treatment as well as interaction energies (with or without some data omitting) are surprisingly good and indicate linear dependence of the PM6 and DFT results. Only statistical parameters for the MPA charges obtained by the DFT-B3LYP method are significantly worse.

Conclusions

The relation between Cu atomic charges has been investigated in terms of MPA, NBO and APT treatments as well as interaction energies obtained

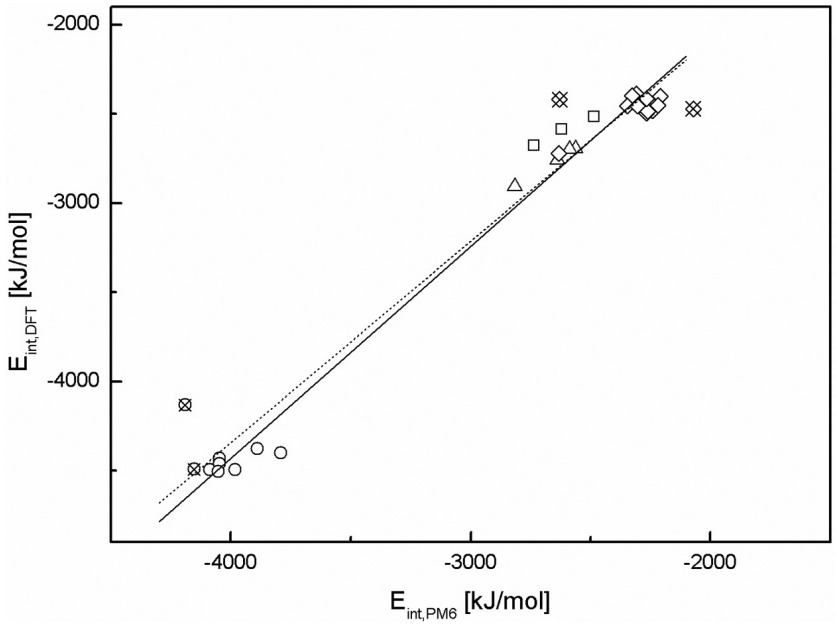

Fig. 11. Plot of interaction energies obtained by the DFT-B3LYP method *vs* the PM6 method for $^2[Ti_{40}O_{124}H_{81}Cu]^{5-}$ (circles), $^2[Ti_7O_{28}H_{26}Cu]^0$ (squares), $^2[Ti_2O_{10}H_{10}Cu]^0$ (triangles), and $^2[Ti_7O_{30}H_{30}Cu]^0$ (diamonds) systems. Dashed and full lines correspond to linear regression for all systems and for all but I-B3, I-C2 (crossed circles), II-C1e and II-C2b systems (crossed diamonds), respectively.

Tab. 3. Regression parameters (a_1, a_0) of Eq. (2) with standard deviations for model systems I and II (see Figs. 1, 5—7) and the coefficient of determination (R^2) for the dataset consisting of N components.

N	Y	X	a_1	a_0	R^2
30	$q(Cu)_{DFT,MPA}$	$q(Cu)_{PM6,MPA}$	0.48 ±0.10	0.007 ±0.075	0.42101
	$q(Cu)_{DFT,NBO}$	$q(Cu)_{PM6,MPA}$	0.602 ±0.047	0.290 ±0.034	0.84992
	$E_{int,DFT}$	$E_{int,PM6}$	1.130 ±0.040	176 ±120 [c]	0.96452
28[a]	$q(Cu)_{DFT,MPA}$	$q(Cu)_{PM6,MPA}$	0.439 ±0.070	0.055 ±0.052	0.58896
	$q(Cu)_{DFT,NBO}$	$q(Cu)_{PM6,MPA}$	0.600 ±0.041	0.293 ±0.030	0.88880
	$E_{int,DFT}$	$E_{int,PM6}$	1.176 ±0.040	290 ±120 [c]	0.97032
26[b]	$q(Cu)_{DFT,MPA}$	$q(Cu)_{PM6,MPA}$	0.502 ±0.081	0.018 ±0.058	0.59683
	$q(Cu)_{DFT,NBO}$	$q(Cu)_{PM6,MPA}$	0.652 ±0.037	0.263 ±0.026	0.92650
	$E_{int,DFT}$	$E_{int,PM6}$	1.188 ±0.031	321 ±91[c]	0.98314

Remarks:

[a] I-B4 and I-C2 models omitted

[b] I-B4, I-C2, II-C1e and II-C2b models omitted

[c] in kJ/mol units

by the PM6 and DFT-B3LYP methods. Unfortunately, Gaussian software refuses to evaluate NBO charges for semiempirical methods. Moreover, APT charges require vibrational analysis for optimized geometries. Despite these restrictions, our results indicate linear dependence between the Cu charges (except for the DFT-B3LYP ones) and interaction energies obtained by both methods. Nevertheless, this conclusion assumes data evaluated with standard accuracy. Our results confirm lower reliability of MPA charges for DFT methods (unlike the semiempirical ones) which is well known.

Acknowledgements

This study has received funding from the European Union's Horizon 2020 research and innovation program under grant agreement No. 685817 (HISENTS). The author thanks the HPC center at the Slovak University of Technology in Bratislava, which is a part of the Slovak Infrastructure of High Performance Computing (SIVVP Project ITMS 26230120002, funded by the European Region Development Funds) for providing computing facilities. The Ministry of Education, Science, Research and Sport of the Slovak Republic is appreciated for funding within the scheme 'Excellent research teams'.

Appendix

Tab. A1. Copper atomic charges, $q(Cu)_{M,P}$, and interaction energies, $E_{int,M}$, for model systems I (Fig. 1) obtained by M = PM6 (Breza and Šimon, 2019) or DFT (this study) methods and P = MPA, APT or NBO population analyses.

Model	$q(Cu)_{PM6,MPA}$	$q(Cu)_{PM6,APT}$	$E_{int,PM6}$ [kJ/mol]	$q(Cu)_{DFT,MPA}$	$q(Cu)_{DFT,NBO}$	$E_{int,DFT}$ [kJ/mol]
I-A	0.586	0.669	–3789.9	0.274	0.621	–4400.7
I-B1	0.585	0.638	–3888.6	0.287	0.633	–4376.8
I-B2	0.633	0.721	–4046.8	0.247	0.72	–4430.3
I-B3	0.648	0.744	–4190.3	0.016	0.564	–4131.3
I-B4	0.634	0.734	–4086.5	0.248	0.706	–4494.6
I-B5	0.648	0.721	–4047.2	0.200	0.662	–4459.9
I-B6	0.645	0.740	–3981.1	0.244	0.719	–4493.4
I-C1	0.627	0.739	–4053.0	0.261	0.696	–4505.3
I-C2	0.641	0.899	–4152.6	0.058	0.751	–4492.7

Tab. A2. Copper atomic charges, $q(Cu)_{M,P}$, and interaction energies, $E_{int,M}$, for model systems II (Figs. 4–6) obtained by M = DFT (Breza and Šimon, 2020) or PM6 (this study) methods and P = MPA, APT or NBO population analyses.

Model	$q(Cu)_{DFT,MPA}$	$q(Cu)_{DFT,APT}$	$q(Cu)_{DFT,NBO}$	$E_{int,DFT}$ [kJ/mol]	$q(Cu)_{PM6,MPA}$	$E_{int,PM6}$ [kJ/mol]
II-A1a	0.518	0.829	0.957	–2586.4	1.063	–2620.3
II-A2a	0.684	1.054	1.048	–2675.8	1.212	–2735.5
II-A2b	0.403	0.541	0.710	–2516.5	0.645	–2484.4
II-B1a	0.406	0.585	0.719	–2695.6	0.648	–2563.0
II-B1b	0.286	0.507	0.629	–2757.2	0.633	–2638.3
II-B1c	0.540	0.959	1.001	–2906.6	1.144	–2816.8
II-B2a	0.330	0.565	0.710	–269.06	0.655	–2588.4
II-C1a	0.382	0.632	0.711	–2401.9	0.658	–2208.5
II-C1b	0.408	0.579	0.734	–2483.4	0.646	–2241.5
II-C1c	0.368	0.546	0.659	–2387.1	0.64	–2310.4
II-C1d	0.379	0.533	0.630	–2396.9	0.621	–2327.8
II-C1e	0.314	0.520	0.652	–2470.5	0.816	–2071.5
II-C1f	0.437	0.533	0.686	–2453.9	0.643	–2271.1
II-C1g	0.343	0.513	0.653	–2494.4	0.633	–2265.6
II-C1h	0.383	0.617	0.720	–2451.8	0.640	–2217.8
II-C2a	0.369	0.529	0.619	–2453.7	0.628	–2347.1
II-C2b	0.550	1.250	1.009	–2419.1	1.253	–2629.8
II-C2c	0.270	0.500	0.596	–2722.8	0.582	–2632.8
II-C2d	0.435	0.564	0.679	–2453.6	0.645	–2305
II-C2e	0.437	0.531	0.685	–2486.5	0.643	–2261.4
II-C2f	0.360	0.512	0.666	–2415.6	0.646	–2266.7

References

Alagona G, Ghio C (2009a) Antioxidant Properties of Pterocarpans through Their Copper(II) Coordination Ability. A DFT Study in Vacuo and in Aqueous Solution. J Phys Chem. A 113: 15206–15216.

Alagona G, Ghio C (2009b) Plicatin B conformational landscape and affinity to copper (I and II) metal cations. A DFT study. Phys Chem Chem Phys 11: 776–790.

Becke AD (1993) Density-functional thermochemistry 3. The role of exact exchange. J Chem Phys 98: 5648–5652.

Breza M, Šimon P (2019) Quantum-chemical studies of rutile nanoparticles toxicity I. Defect-free rod-like model clusters. Acta Chim Slovaca 12: 168–174.

Breza M, Šimon P (2020) On shape dependence of the toxicity of rutile nanoparticles. J Nanopart Res (2020) 22: 0058.

Cioslowski J (1989) A new population analysis based on atomic polar tensors. J Am Chem Soc 111: 8333–8336.

Dunning Jr TH, Hay PJ (1977) Gaussian Basis Sets for Molecular Calculations, in Modern Theoretical Chemistry, (Ed. Schaefer HF III), Vol. 3, Plenum, New York, pp. 1—28.

Frisch MJ, Trucks GW, Schlegel HB, Scuseria GE, Robb MA, Cheeseman JR et al. (2009) Gaussian 09, Revision D.01, Gaussian Inc., Wallingford, CT.

Forest V, Leclerc L, Hochepie JF, Trouvé A, Sarry G, Pourchez J (2017) Impact of cerium oxide nanoparticles shape on their in vitro cellular toxicity. Toxicol Vitro 38: 136—141.

Hay PJ, Wadt WR (1985) Ab initio effective core potentials for molecular calculations — potentials for the transition-metal atoms Sc to Hg. J Chem Phys 82: 270—283.

Hsiao I-L, Huang Y-J (2011) Effects of various physicochemical characteristics on the toxicities of ZnO and TiO nanoparticles toward human lung epithelial cells. Sci Total Environ 409: 1219—1228.

Huang Y-W, Cambre M, Lee H-J (2017) The toxicity of nanoparticles depends on multiple molecular and physicochemical mechanisms. Int J Mol Sci 18: 2702.

Jelemenská I, Breza M (2021) Comparative DFT study of the effectiveness of p-phenylenediamine antioxidants through their coordination ability towards the late 1st row transition metals. Polym. Degrad. Stab. 183: 109438.

Lee JH, Ju JE, Kim BI, Pak PJ, Choi EK, Lee HS, Chung N (2014) Rod-shaped iron oxide nanoparticles are more toxic than sphere-shaped nanoparticles to murine macrophage cells. Environ Toxicol Chem 33: 2759—2766.

Mammino L (2013) Investigation of the antioxidant properties of hyperjovinol A through its Cu(II) coordination ability. J Mol Model 19: 2127—2142.

Mulliken RS (1955) Electronic Population Analysis on LCAO-MO Molecular Wave Functions I. J Chem Phys 23: 1833—1840.

Puškárová I, Breza M (2016) DFT studies of the effectiveness of p-phenylenediamine antioxidants through their Cu(II) coordination ability. Polym Degrad Stab 128: 15—21.

Puškárová I, Breza M (2017) DFT studies of the effectiveness of p-substituted diphenyl amine antioxidants in styrene-butadiene rubber through their Cu(II) coordination ability. Chem Phys Lett 680: 78—82.

Reed AE, Curtiss LA, Weinhold F (1988) Intermolecular interactions from a natural bond orbital, donor-acceptor viewpoint. Chem Rev 88: 899—926.

Stewart JJP (2007) Optimization of parameters for semiempirical methods. V. Modification of NDDO approximations and application to 70 elements. J Mol Model 13: 1173—1213.

Tsiepe TJ, Kabanda M, Serobatse KRN (2015) Antioxidant Properties of Kanakugiol Revealed Through the Hydrogen Atom Transfer, Electron Transfer and M^{2+} (M^{2+} = Cu(II) or Co(II) Ion) Coordination Ability Mechanisms. A DFT Study In Vacuo and in Solution. Food Biophys 10: 342—359.

sciendo

Predictive control of a cascade of biochemical reactors

Martin Mojto, Michaela Horváthová, Karol Kiš, Matúš Furka, Monika Bakošová

Slovak University of Technology in Bratislava, Faculty of Chemical and Food Technology, Institute of Information, Engineering, Automation, and Mathematics, Radlinského 9, 812 37 Bratislava, Slovak Republic
martin.mojto@stuba.sk

Abstract: Rapid growth of the human population has led to various problems, such as massive overload of wastewater treatment plants. Therefore, optimal control of these plants is a relevant subject. This contribution analyses control of a cascade of ten biochemical reactors using simulation results with the aim to design optimal and predictive control strategies and to compare the achieved control performance. The plant represents a complicated process with many variables involved in the model structure, reduced to the single-input and single-output system. The first implemented approach is linear offset-free model predictive control which provides the optimal input trajectory minimising a quadratic cost function. The second control strategy is robust model predictive control with similar features as model predictive control but including the uncertainty of the process. The final approach is generalised predictive control, mostly used in the industry because of its simple structure and sufficiently good control performance. All considered predictive controllers provide satisfactory control performance and remove the steady-state control error despite the constrained control inputs.

Keywords: biochemical reactor, generalised predictive control, model predictive control, robust model predictive control, wastewater treatment

Introduction

The term biochemical reactor describes a processing unit supporting a biologically active environment, which involves living organisms or biochemically active substances. If the environmental conditions inside the biochemical reactor are optimal, microorganisms or cells are effectively fulfilling their function without producing impurities. The productivity and growth of microorganisms can be influenced by temperature and the concentration of dissolved gasses, pH value, and nutrients concentration. Therefore, process control of these variables represents an increasingly relevant part of the biotechnology industry (Henson, 2006). Feedback control systems are applied to achieve optimal growth and productivity and to minimise the production costs. The application of process control strategies in biochemical reactors is an important research subject.

The most common industrial controllers are proportional-integration-derivative (PID) controllers. Their simplicity and straightforward application granted them popularity mainly in the chemical and petrochemical industry. In Rajinikanth and Latha (2010), a PID control system was applied to control an unstable biochemical reactor. A PI controller with fractional order filter has been designed for a biochemical reactor in Vinopraba et al. (2013).

The increased availability of online sensors and analysers allowed implementing more advanced optimisation-based controllers to biochemical reactors. An overview of optimal adaptive algorithms applied to chemical and biochemical reactors is presented in Smets et al. (2004). One of the most advantageous optimisation-based techniques is model predictive control (MPC). This approach has been applied in many areas including chemical engineering and food industry. In MPC, dynamic model of a plant is considered to predict its future behaviour. These algorithms can include constraints on process variables. The optimisation-based approach manages to minimise costs and maximise the quality and safety of the operation. Moreover, MPC is very efficient in multivariable control. In Ramaswamy et al. (2005), MPC was considered to control a biochemical reactor towards an unstable steady state tuning prediction horizon to increase control performance of the plant. Nonlinear model predictive control was used to control fed-batch biochemical reactors in Craven et al. (2014) and Chang et al. (2016).

Throughout the years, multiple predictive controllers based on real-time optimal control have been developed. For instance, generalised predictive control (GPC) (Clarke et al., 1987), where the mathematical model is a controlled auto-regressive and integrated moving-average (CARIMA) model. The objective of GPC is to compute a sequence of future

control signals to minimise a multistage cost function. The GPC method in adaptive and nonadaptive configuration was applied to a fed-batch penicillin production in Rodrigues et al. (2002), with the dissolved oxygen concentration as the controlled variable. The GPC in both, adaptive and nonadaptive, configurations improved control performance of the plant compared to the conventional PID and predictive Dynamic Matrix Control. In Akay et al. (2010), the temperature of a biochemical reactor with baker's yeast production was controlled using the GPC approach. The control performance was analysed considering multiple positive and negative step changes of the set point.

The behaviour of biochemical reactors, both continuous and batch, is usually highly nonlinear. In some cases, the nonlinearity may cause process-model mismatch leading to less effective MPC. To overcome this obstacle, robust MPC (RMPC) was implemented. There are many forms of RMPC: e.g., RMPC using linear matrix inequalities (LMIs) was introduced in Kothrare et al. (1996); Lucia and Engell (2013) designed a nonlinear RMPC for a batch biochemical reactor and improved its control performance. RMPC formulated using linear matrix inequalities was designed for a continuously stirred tank reactor (CSTR) in Oravec and Bakošová (2012) and Oravec et al. (2017).

This paper presents the application of various predictive controllers for a cascade of ten biochemical reactors. The considered plant models wastewater treatment removing undesired compounds from water. Optimal control of these devices is a relevant task as sustainability is nowadays one of the key requirements of industrial production. This research aims to compare control performance of conventional MPC, GPC and RMPC implemented to the cascade of ten biochemical reactors using simulations. The control performance was analysed considering various criteria.

Plant Description

The carrousel plants represent an important part of the industrial wastewater treatment technology. Overall, these plants usually consist of several continuous stirred-tank reactors (CSTR) with a large volume. The disadvantage of this industrial unit is the presence of strong disturbances caused by the unstable feed flow rate and wastewater composition (Pons, 2011).

This research considers a cascade of ten aerated biochemical reactors for the carrousel activation shown in Fig. 1 (Derco et al., 1994; Trautenberger, 2017). The given structure of the cascade provides both oxic and anoxic environments for the biomass. Moreover, each bioreactor involves a vertical fan (aerator) and a supply of airflow, to induce the required conditions for the biochemical processes within the cascade. The feed flow (wastewater) characterised by the concentration of the organic component (S) and impurities such as ammonium salts (NH) or nitrates/nitrites (NO) is fed into the first bioreactor of the cascade. The profile of the mixture composition inside the cascade of bioreactors is the following:

- S_0, NH_0, NO_0 (feed flow),
- S_1, NH_1, NO_1 (output from the first bioreactor),
- S_{10}, NH_{10}, NO_{10} (output from the tenth bioreactor).

A part of a mixture from the tenth bioreactor is returned to the first bioreactor as internal reflux and the rest of the mixture enters the final clarifier. The mixture in the final clarifier is separated by the sedimentation process to the effluent and sludge flow. The second (sludge) reflux is produced by the

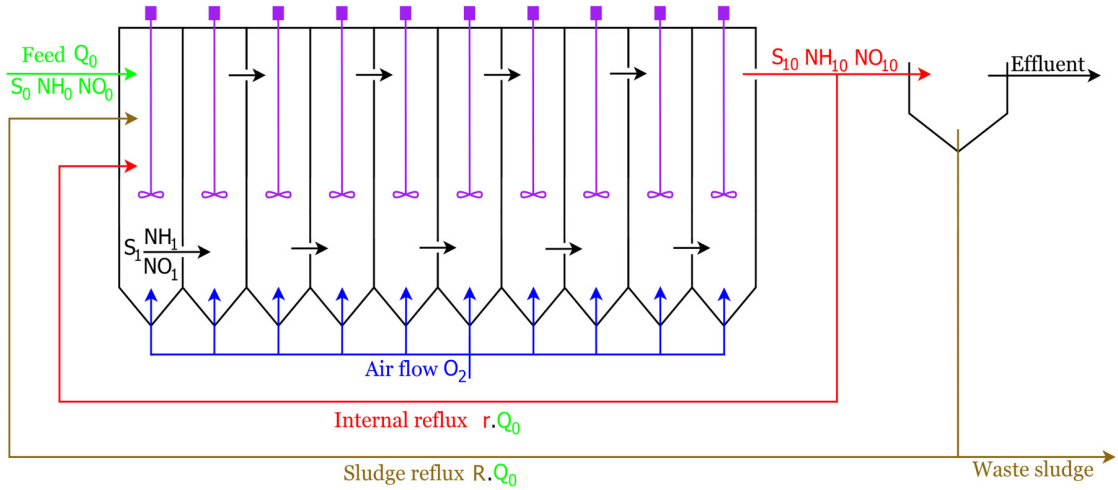

Fig. 1. Flow diagram of the carrousel plant involving the cascade of ten biochemical reactors and a final clarifier.

sludge flow from the clarifier and the rest of the sludge leaves the plant as the waste.

Mass balance equations of the components of the mixture were used to design the mathematical model. These equations follow from the biochemical processes within the plant, such as carbonisation, nitrification, and denitrification. Furthermore, the mathematical model includes the Monod equation to consider the biomass growth. There are several assumptions of the designed mathematical model, such as:

- feed flow without the suspended or solid particles,
- oxygen does not constrain the processes of carbonisation or nitrification,
- reactors inside the cascade are perfectly mixed and variations in the temperature or pH are ignored.

Process identification

The purpose of process identification is to gain desired information about the process dynamics for further analysis (e.g., design of appropriate controllers). The most common structures of the identified models represent a state-space representation or a transfer function. In this case, the identified model represents the transfer function $G(s)$ between:

- the concentration of ammonium salts from the tenth bioreactor (NH_{10}, measured variable and controlled variable in the future),
- the ratio of the internal reflux to the feed flow rate (r, input variable and control input in the future),

in the form of Eq. (1). Since a robust approach was also considered, uncertain parameters were expressed using interval uncertainty within minimal and maximal values of each identified parameter.

The resulting transfer function has the following structure (Furka et al., 2020):

$$G(s) = \frac{b_4 s^4 + b_3 s^3 + b_2 s^2 + b_1 s + b_0}{a_4 s^4 + a_3 s^3 + a_2 s^2 + a_1 s + a_0}, \qquad (1)$$

The numerator is a polynomial of the fourth order with the parameters b_0–b_4 and four zeros. The denominator structure is the same (fourth order polynomial with parameters a_0–a_4) and it involves four poles. The obtained nominal, minimal and maximal values of the transfer function parameters are stated in Tab. 1. The nominal model with nominal values of identified parameters was considered for the design of MPC and GPC. The robust MPC considered vertex systems are models generated for combinations of minimal and maximal values of uncertain parameters. All obtained vertex systems define a convex hull of all possible uncertain systems that represent possible behaviour of the cascade of biochemical reactors. The step response of the process model with nominal, minimal, and maximal parameters is depicted in Fig. 2.

To verify the obtained nominal model of the process, it was compared with the original nonlinear

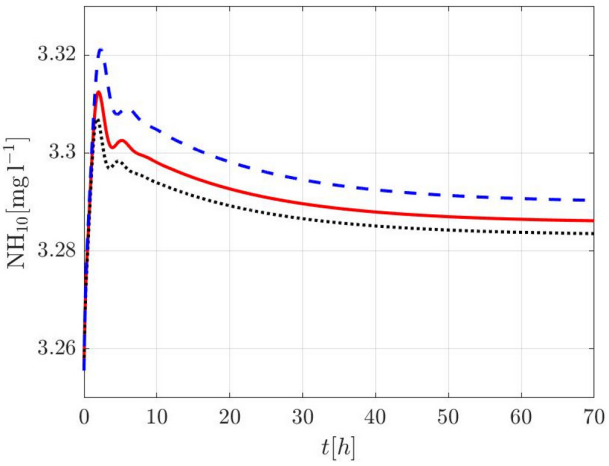

Fig. 2. Step response of the process model with nominal (red solid line), minimal (black dotted line), and maximal (blue dashed line) parameters.

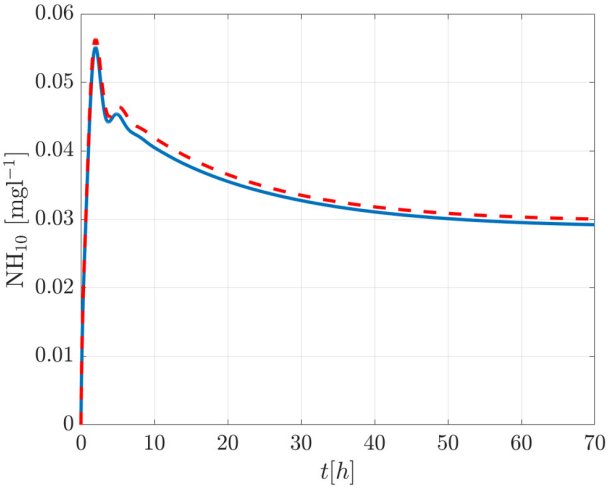

Fig. 3. Comparison of the step response of the nonlinear process (red dashed line) and the identified nominal model (blue solid line).

Tab. 1. Nominal, maximal, and minimal values of identified model parameters.

Parameters	b_0	b_1	b_2	b_3	b_4	a_0	a_1	a_2	a_3	a_4
Nominal	0.03	0.83	0.12	0.11	-56.10^{-3}	0.94	16.77	9.94	5.72	1.00
Maximal	0.04	1.03	0.13	0.11	-54.10^{-3}	1.29	23.06	12.28	6.39	1.00
Minimal	0.02	0.65	0.11	0.10	-52.10^{-3}	0.63	11.24	7.74	5.05	1.00

process (Fig. 3). As it can be seen, the discrepancy (e.g. sum of squared residuals) between the trajectories is negligible. Therefore, the nominal model describes the behaviour of the nonlinear plant sufficiently.

The obtained nominal system can be discretised and transformed to the state-space representation. This form of the model structure is more accessible for the design of controllers. Considering the process dynamics, sampling time $T_s = 0.5$ h is used for discretisation.

Predictive Control Methods

Model predictive control

The cascade of ten biochemical reactors represents a complex system with disturbances and uncertainties. To control this system, linear offset-free MPC was designed and to ensure offset-free control of the plant, augmented model with constant output disturbances was considered (Meader at al., 2009). The augmented state-space model was considered as follows:

$$x(k+1) = Ax(k) + Bu(k),\ x(0) = x_0 \tag{2}$$

$$y(k) = Cx(k) + Fp(k), \tag{3}$$

where $k \geq 0$ is a discrete time instant, $x(k) \in \mathbb{R}^{n_x}$ represents states, $u(k) \in \mathbb{R}^{n_u}$ represents control inputs, $y(k) \in \mathbb{R}^{n_y}$ stands for system outputs and $p(k) \in \mathbb{R}^{n_p}$ stands for constant output disturbances. Parameter x_0 represents the initial conditions of the system. Furthermore, the discrete state-space representation contains matrices $A \in \mathbb{R}^{n_x \times n_x}$, $B \in \mathbb{R}^{n_x \times n_u}$, $C \in \mathbb{R}^{n_y \times n_x}$, $F \in \mathbb{R}^{n_y \times n_p}$ representing state, input, output, and disturbance matrices, respectively.

Based on optimisation, MPC evaluates a sequence of optimal control inputs at each sampling time. The evaluation considers future behaviour of the model and constraints of outputs, inputs, and states. After the evaluation of the sequence of optimal control inputs, MPC considers only the first computed control input to ensure its predictive properties. The optimisation problem is formulated in the following way:

$$\min_{\Delta u(k)} \sum_{k=0}^{N} \left(Q \,\|\, r(k) - y(k) \,\|_2^2 - R \,\|\, \Delta u(k) \,\|_2^2 \right), \tag{4}$$

s.t. $$x(k+1) = Ax(k) + Bu(k),\ x(0) = x_0 \tag{5}$$

$$y(k) = Cx(k) + Fp(k), \tag{6}$$

$$u_{\min} \leq u(k) \leq u_{\max}, \tag{7}$$

$$x_{\min} \leq x(k) \leq x_{\max}, \tag{8}$$

$$y_{\min} \leq y(k) \leq y_{\max}, \tag{9}$$

Parameter N represents the prediction horizon, $r(k) \in \mathbb{R}^{n_y}$ is the reference, $\Delta u(k) = u(k) - u(k-1)$ is the difference of control action. Variables Q and R are tuning matrices weighting control output and control input. The tuning matrices are positively definite and diagonal.

Robust model predictive control

The plant-model mismatch is treated in the RMPC design. The objective of RMPC design is to optimise the state-feedback control law to compute optimal control action. Unlike conventional MPC, RMPC minimises the "worst case" scenario in an infinite cost function horizon at each sampling time. The convex optimisation problem is formulated involving LMIs. In receding horizon setup, RMPC computes the sequence of optimal control actions over the prediction horizon but implements only the first optimal control action. In order to remove steady-state tracking error, $e(k)$, the vector of states was extended by an integral action in the following way:

$$\tilde{x}(k) = \begin{bmatrix} x(k) \\ \sum_{j=0}^{k} e(j) \end{bmatrix},\ e(k) = r(k) - y(k). \tag{13}$$

The extended uncertain state-space model is defined as follows:

$$\tilde{x}(k+1) = \tilde{A}\tilde{x}(k) + \tilde{B}u(k),\ \tilde{x}(0) = \tilde{x}_0 \tag{14}$$

$$y(k) = \tilde{C}\tilde{x}(k), \tag{15}$$

where $\tilde{A}$, $\tilde{B}$, $\tilde{C}$ are matrices of the system extended subject to integral action.

For the purpose of RMPC design, the controlled plant is represented by an uncertain discrete-time state-space model in the following form:

$$\tilde{x}(k+1) = \hat{A}\tilde{x}(k) + \hat{B}u(k),\ x(0) = x_0 \tag{10}$$

$$y = \hat{C}\tilde{x}(k), \tag{11}$$

$$\left[\hat{A}, \hat{B}, \hat{C}\right] \in \operatorname{convhull}\left(\left\{ \left[\tilde{A}^{(v)}, \tilde{B}^{(v)}, \tilde{C}^{(v)} \right], \forall v \right\} \right), \quad v \in n_v \tag{12}$$

where v represents the v-th vertex of the system and n_v represents the total number of system vertices.

Input and output symmetric constraints are formulated as Euclidean and peak norms (Kothrare et al., 1996):

$$\begin{gathered} \left\| u(k) \right\|_2 \leq u_{\text{sat}},\ \left| u_j(k) \right| \leq u_{\text{sat},j}, \\ j \in \{1, 2, \ldots, n_u\},\ \left\| y(k) \right\|_2 \leq y_{\text{sat}}, \end{gathered} \tag{16}$$

where u_{sat} and y_{sat} represent values of the symmetric constraints on control inputs and outputs, respectively. However, this approach tends to be conservative as it does not operate with the full range of feasible values of control inputs. To overcome this obstacle, Huang et al. (2011) presented an improved RMPC design method considering the presence of actuator saturation and gain matrix of the state-feedback control law was evaluated without constraints $\tilde{K}(k) \in \mathbb{R}^{n_u \times (n_x + n_y)}$ and with constraints $F(k) \in \mathbb{R}^{n_u \times (n_x + n_y)}$ (Huang et al., 2011). The control input in the presence of actuator saturation, $u_s(k)$ is then computed using the following equation

$$u_s(k) = \left(E_k^m \tilde{K}(k) + \tilde{E}_k^m F_k\right)\tilde{x}(k), \tag{17}$$

where parameter $E_k^m \in \mathbb{R}^{n_u \times n_u}, \quad \forall m \in \{1, \dots 2^{n_u}\}$ is the matrix of all combinations of constrained control inputs. Matrix $\tilde{E}_k^m \in \mathbb{R}^{n_u \times n_u}, \ \forall m \in \{1, \dots 2^{n_u}\}$ represents the matrix of all combinations of unconstrained control inputs.

$$\tilde{E}_k^m = I - E_k^m. \tag{18}$$

The computation of $\tilde{K}(k)$ and $F(k)$ is transformed into the following LMIs

$$\min_{y_k, X_k, Y_k, U_k, Z_k} y_k + \beta y_{s,k} \tag{19}$$

$$\text{s.t.} \quad \begin{bmatrix} X_k & * & * & * \\ \hat{A}^{(v)} X_k + \hat{B}^{(v)} Y_k & X_k & * & * \\ \tilde{Q}^{1/2} X_k & 0 & \gamma_{s,k} I & * \\ R^{1/2} Y_k & 0 & 0 & \gamma_{s,k} I \end{bmatrix} \succcurlyeq 0, \tag{20}$$

$$\begin{bmatrix} X_k & * & * & * \\ \hat{A}^{(v)} X_k + \hat{B}^{(v)} \left(E_k^m Z_k + \tilde{E}_k^m Y_k\right) & X_k & * & * \\ \tilde{Q}^{1/2} X_k & 0 & \gamma_k I & * \\ R^{1/2} \left(E_k^m Z_k + \tilde{E}_k^m Y_k\right) & 0 & 0 & \gamma_k I \end{bmatrix} \succcurlyeq 0, \tag{21}$$

$$\begin{bmatrix} 1 & * \\ \tilde{x}(k) & X_k \end{bmatrix} \succcurlyeq 0, \tag{22}$$

$$\begin{bmatrix} u_{sat}^2 I & * \\ Y_k^T & X_k \end{bmatrix} \succcurlyeq 0, \tag{23}$$

$$\begin{bmatrix} U_k & * \\ Y_k^T & X_k \end{bmatrix} \succcurlyeq 0, \ U_{j,j} \le u_{sat,j}^2, \ j \in \{1, 2, \dots, n_u\}, \tag{24}$$

$$\begin{bmatrix} X_k & * \\ \hat{C}\left[\hat{A}^{(v)} X_k + \hat{B}^{(v)} \left(E_k^m Z_k + \tilde{E}_k^m Y_k\right)\right] & y_{sat}^2 I \end{bmatrix} \succcurlyeq 0, \tag{25}$$

$$\gamma_k - \gamma_{s,k} > 0. \tag{26}$$

Minimisation of auxiliary weight parameter $\gamma_k > 0$ ensures the minimisation of the weighted inverted Lyapunov matrix, X_k, defined as:

$$X_k = \gamma_k P^{-1}, \ P = P^T \succcurlyeq 0. \tag{27}$$

Matrix P represents the Lyapunov matrix. The optimised parameter $\gamma_{s,k} > 0$ shows the weight on unconstrained control input. The weighting constant $\beta > 0$ represents another degree of freedom in the MPC design. Parameters $\tilde{Q} \in \mathbb{R}^{(n_x + n_y) \times (n_x + n_y)}$ and $R \in \mathbb{R}^{n_u \times n_u}$ are weighting matrices. Matrix $\tilde{Q}$ was extended subject to the extended state vector from Eq. (13).

Auxiliary matrix of the controller design without constraints, Z_k is defined as follows:

$$Z_k = \tilde{K} X_k, \tag{28}$$

matrix Y_k represents the auxiliary matrix of the constrained controller design. parameter U_k represents auxiliary matrix of inputs of robust MPC. Symbol * represents the symmetric structure of the matrix, I is the identity matrix of appropriate dimensions and 0 denotes zero matrix of appropriate dimensions.

unconstrained state-feedback controller gain is then computed as follows:

$$\tilde{K} = Z_k X_k^{-1}, \tag{29}$$

constrained state-feedback controller gain is then computed as follows:

$$F = Y_k X_k^{-1}. \tag{30}$$

The considered predictive algorithms (RMPC and MPC) require measurements of the states to compute optimal control input. However, the states of the biochemical reactor considered in this paper were not measurable, therefore the Luenberger state observer was introduced. Detail information on the state observer implementation can be found in Furka et al. (2020).

Generalised predictive control

The considered cascade of ten bioreactors is a SISO system and therefore GPC represents a suitable option for the control of such a plant. This form of the predictive controller is based on the controlled auto-regressive and integrated moving-average (CARIMA) model with the following structure:

$$\alpha(z) y(k) = \beta(z) u(k) + T(z) \frac{d(k)}{\Delta}, \tag{31}$$

where $\alpha(z)$ and $\beta(z)$ are polynomials representing the denominator and numerator of the discrete transfer function for the process:

$$\alpha(z) = 1 + \alpha_1 z^{-1} + \dots + \alpha_n z^{-n}, \tag{32}$$

$$\beta(z) = \beta_1 z^{-1} + \dots + \beta_m z^{-m}, \tag{33}$$

polynomial $T(z)$ explains the behaviour of the disturbances and $d(k)$ is a random variable with zero

mean. The ratio between $d(k)$ and Δ represents slowly varying disturbances.

The advantage of GPC control strategy using the CARIMA model is in unbiased prediction provided by incorporated estimation of disturbances as the previous equation can be transformed to the following incremental form:

$$\alpha(z)\Delta y(k) = \beta(z)\Delta u(k) + T(z)d(k), \tag{34}$$

where $\Delta u(k) = u(k) - u(k-1)$.

Subsequently, products in the previous equation can be modified as follows (Chen, 2013):

$$\begin{aligned} &\textstyle\sum_{i=1}^{n} \alpha_i \Delta y(k+1-i) = \\ &= \textstyle\sum_{i=1}^{n} \beta_i \Delta u(k-i) + \sum_{i=1}^{n} T_i d(k-i). \end{aligned} \tag{35}$$

Prediction of the output can be derived from the left side of Eq. (35):

$$\begin{aligned} &y(k) + \textstyle\sum_{i=1}^{n+1} (\alpha_i - \alpha_{i-1}) y(k-i) = \\ &= \textstyle\sum_{i=1}^{n} \beta_i \Delta u(k-i) + \sum_{i=1}^{n} T_i d(k-i), \end{aligned} \tag{36}$$

where $\alpha_{n+1} = 0$.

This control strategy determines control input minimising the following cost function:

$$J = \left[r(k) - \hat{y}(k)\right]^T Q \left[r(k) - \hat{y}(k)\right] + \Delta u(k)^T R \Delta u(k), \tag{37}$$

where $\hat{y}(k) = G\Delta u(k) + \hat{y}^*(k)$, variables Q and R are tuning matrices and G is a lower-triangular matrix (Clarke et al., 1987).

The output prediction assuming $\Delta u(k) = 0$ is expressed by:

$$\tilde{y}^*(k+j) = H\Phi^j \tilde{x}(k) + H\Phi^{j-1} \Lambda \left[y(k) - H\tilde{x}(k)\right], \tag{38}$$

where the structure of matrices $H\Phi^j$ and $H\Phi^{j-1}$ is shown in (Chen, 2013).

The following structure of input increment can be derived by setting the gradient of Eq. (37) to zero (Grimble, 1992):

$$\begin{aligned} \Delta u(k) &= (G^T Q G + R)^{-1} G^T Q \left[r(k) - \tilde{y}^*(k)\right] = \\ &= K \left[r(k) - \tilde{y}^*(k)\right], \end{aligned} \tag{39}$$

where K is the gain of the controller.

The state-space representation is derived using observable canonical form realisation. The model structure has the following form:

$$x(k+1) = \Phi x(k) + \Gamma \Delta u(k) + \Lambda d(k), \tag{40}$$

$$y(k) = Hx(k) + d(k), \tag{41}$$

matrices Φ, Γ, Λ and H are defined in (Chen, 2013).

The suitable state observer for the designed state-space model (Eq. (40)) is written as:

$$\tilde{x}(k+1) = \Phi \tilde{x}(k) + \Gamma \Delta u(k) + \Lambda \left[y(k) - H\tilde{x}(k)\right]. \tag{42}$$

Results and Discussion

Control setup

The offset-free reference tracking problem was analysed considering a sequence of the step changes of the reference value. The closed-loop control was designed in the MATLAB/Simulink R2019a environment using CPU i7 3.4 GHz and 8 GB RAM.

To formulate optimisation problems of MPC, YALMIP (Löfberg 2004), toolbox was introduced. The optimisation problem of MPC was solved by the GUROBI Optimization (2020). Weighting matrices Q and R and prediction horizon N were tuned as:

$$Q = \begin{bmatrix} 0.01 & 0 & 0 & 0 \\ 0 & 0.01 & 0 & 0 \\ 0 & 0 & 0.01 & 0 \\ 0 & 0 & 0 & 0.01 \end{bmatrix}, \; R = 1, \; N = 30. \tag{43}$$

The constraints on control input were set as follows: $0 \le u(k) \le 60$. Neither the control output, nor the states were constrained during the MPC design.

To formulate robust MPC, MUP toolbox was considered. Semidefinite programming problems (SDPs) were formulated using YALMIP (Löfberg, 2004) and solved by MOSEK (MOSEK ApS., 2019). Variables $\tilde{Q}$ and R were systematically tuned as follows:

$$\tilde{Q} = \begin{bmatrix} 0.01 & 0 & 0 & 0 & 0 \\ 0 & 0.01 & 0 & 0 & 0 \\ 0 & 0 & 0.01 & 0 & 0 \\ 0 & 0 & 0 & 0.01 & 0 \\ 0 & 0 & 0 & 0 & 5 \end{bmatrix}, \; R = 1. \tag{44}$$

The constraints on control input were set as follows: $0 \le u(k) \le 60$. The control output was not constrained during the design of robust MPC.

When designing MPC and RMPC, the Luenberger state observer was considered to augment the state-space from Eq. (2). The disturbance matrix was considered as follows:

$$F = 1. \tag{45}$$

The state-observer used observer gain designed using pole placement in the following way:

$$L = \begin{bmatrix} 0.047 \\ 1.935 \\ -70.218 \\ 300.593 \\ 6.593 \end{bmatrix}. \tag{46}$$

The setup of prediction horizon N and weighting matrices (Q and R) of the GPC control strategy is

the same as in case of MPC (see Eq. (43)). Due to relatively long prediction horizon, it is impractical to display matrix $G \in \mathbb{R}^{N\times N}$ (see Eq. (39)) from the structure of the GPC controller. As it was mentioned before, matrices of the state-space observer (Φ, Γ, Λ and H) were designed according to Chen (2013).

Control performance

The designed predictive controllers were considered to control the plant described by the linear transfer function in Eq. (1). To compare the controllers, two reference step changes were generated, one positive and one negative. The controlled output is depicted in Fig. 4a) and Fig 5a). The corresponding control input is depicted in Fig. 4b) and Fig 5b). All predictive controllers were compared by simulation using the nominal model of the biochemical reactor. To ensure the consistency of the results, similar values of weighting matrices were considered in all predictive methods. The performance of designed control strategies was also compared by integral absolute error (IAE) and integral squared error (ISE). These criteria have the following structures:

$$\text{IAE} = \sum_{k=0}^{150} |e(k)|, \quad \text{IAE} = \sum_{k=0}^{150} e(k)^2, \tag{47}$$

where $e(k)$ is the control error. The resulting values of IAE and ISE criteria are listed in Tab. 2. The obtained values confirm better control performance of MPC, and GPC compared to RMPC.

The resulting trajectories show that all the designed controllers removed the steady-state control error, and each controlled system reached the reference value without offset. Moreover, MPC and RMPC

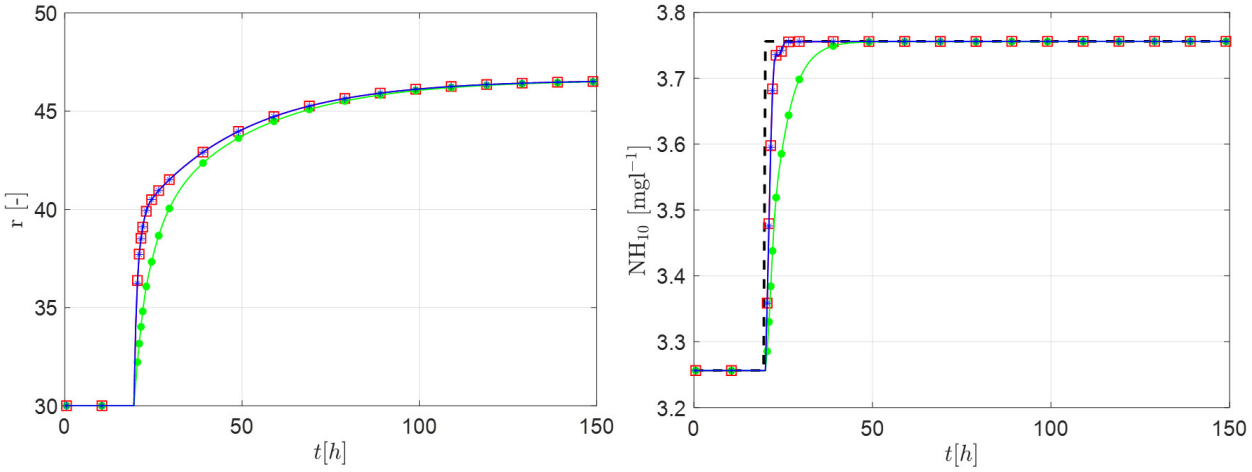

a) Control input to the process b) Output from the process

Fig. 4. Comparison of the control performance provided by positive reference step change. MPC (□), RMPC (●), GPC (*), reference (dashed black) line.

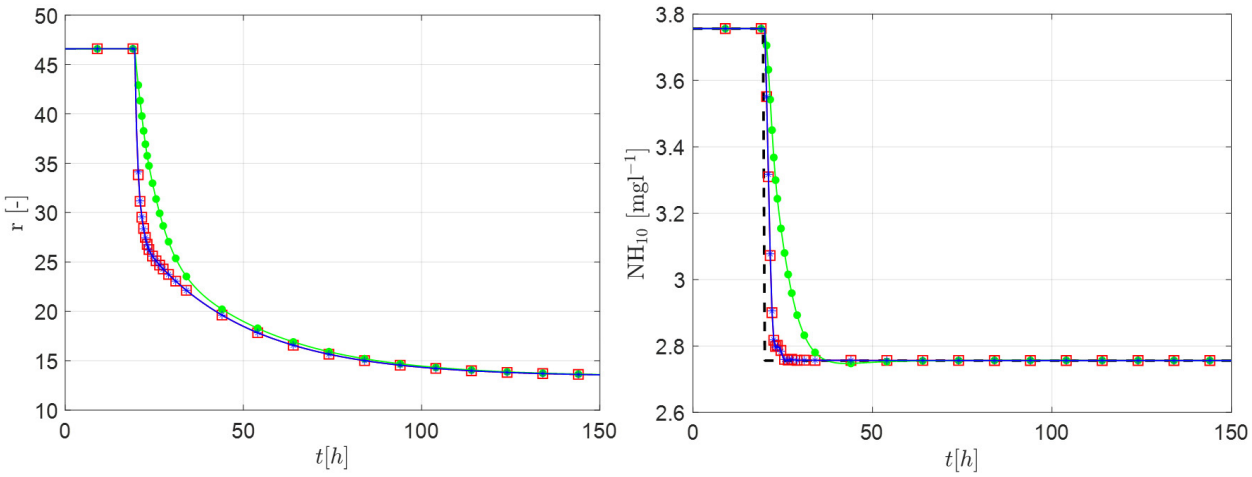

a) Control input to the process b) Output from the process

Fig. 5. Comparison of the control performance provided by negative reference step change. MPC (□), RMPC (●), GPC (*), reference (dashed black) line.

Tab. 2. Comparison of IAE [mg l^{-1} h] and ISE [mg^2 l^{-2} h] criteria of the designed controllers.

Criterion	**IAE [mg l^{-1} h]**			**ISE [mg^2 l^{-2} h]**		
Controller	MPC	RMPC	GPC	MPC	RMPC	GPC
First step change	1.5580	4.7197	1.5594	0.5176	1.2543	0.5205
Second step change	3.1161	9.9396	3.1189	2.0704	5.6376	2.0820
Sum	4.6741	14.6593	4.6783	2.5880	6.8919	2.6025

satisfied the constraints on the control input. The GPC did not consider constraints on the control input during the design.

According to the results, MPC and GPC achieved almost the same control performance. This is mainly caused by the assumption that the controlled process is a single-input-single-output system.

Variations of the feed flow rate represent external disturbance. In the simulation results, variations of the feed flow were considered to be minor and occasional and compensated by a well-tuned controller. If the disturbance is significant, it could be measured to design a control loop with disturbance rejection. Moreover, significant variations of the feed flow rate can still be reduced by storing the feed in additional tank before it enters the carrousel plant.

The output variable of the process (Fig. 4b and 5b) was stabilized faster than the input variable (Fig. 4a and 5a). The reason is the presence of a stable zero in the transfer function of the studied process. All designed controllers try to compensate the effect of this zero and therefore the input variable is still varying while the output variable is already in steady state.

There are also slight differences between the input trajectory of RMPC and of other controllers. This is reflected in the increased settling time and both IAE and ISE criteria. This is an expected result because unlike other controllers, the design of RMPC includes an uncertain model of the plant. If the case study considered control of a nonlinear model, RMPC would be expected to outperform both MPC and GPC, as the process model mismatch would be significant.

Conclusion

In this paper, the design and application of multiple predictive controllers were investigated. The controllers were applied for a cascade of ten biochemical reactors using simulations. First, conventional MPC and GPC were designed for a nominal model of the plant. RMPC was designed, considering an uncertain model of the plant. To design the RMPC, LMI-based approach with reduced conservativeness was applied. The control performance of the designed controllers was compared using integral criteria. As expected, the conventional MPC and GPC control performance was almost identical. Application of the RMPC decreased the control performance; however, this approach is able to handle uncertain and nonlinear behaviour of the plant.

Acknowledgement

The authors gratefully acknowledge the contribution of the Scientific Grant Agency of the Slovak Republic under the grants 1/0585/19 and 1/0545/20, the Slovak Research and Development Agency under the project APVV-15-0007. M. Horváthová was also supported by an internal STU grant.

References

Akay B, Ertunç S, Bursali N, Hapoğlu H, Alpbaz M (2010) Application of generalized predictive control to baker's yeast production, Chemical Engineering Communications, 190: 999—1017.

Chang L, Xinggao L, Henson MA (2016) Nonlinear model predictive control of fed-batch fermentations using dynamic flux balance models, Journal of Process Control, 42: 137—149.

Chen Y (2013) A Novel DMC-Like Implementation of GPC, 2013 International Conference on Mechatronic Sciences, Shenyang, China: 362—366.

Clarke DW, Mohtadi C, Tuffs PS (1987) Generalized predictive control — Part I. The basic algorithm, Automatica, 23: 137—148.

Craven S, Whelan J, Glennon B (2014) Glucose concentration control of a fed-batch mammalian cell bioprocess using a nonlinear model predictive controller, Journal of Process Control, 24: 344—357.

Derco J, Hutňan M, Králik M (1994) Modelling of carrousel type activation (in Slovak), Vodní hospodářství, 42: 23—27.

Furka M, Kiš K, Horváthová M, Mojto M, Bakošová M, (2020) Identification and Control of a Cascade of Biochemical Reactors, 2020, Cybernetics & Informatics, Velké Karlovice, Czech Republic.

Grimble MJ (1992) Generalized predictive optimal control: An introduction to the advantages and limitations, International Journal of System Science 23: 85—98.

GUROBI Optimization (2020) GUROBI Optimizer Quick Start Guide. Version 9.0.

Henson MA (2006) Biochemical reactor modeling and control, IEEE Control Systems Magazine, 26: 54–62.

Huang H, Li D, Lin Z, Xi Y (2011) An improved robust model predictive control design in the presence of actuator saturation, Automatica, 47: 861–864.

Kothare MV, Balakrishnan V, Morari M (1996) Robust constrained model predictive control using linear matrix inequalities, Automatica, 32: 1361–1379.

Löfberg J (2004) YALMIP: A Toolbox for Modeling and Optimization in MATLAB, Proceedings. of the CACSD Conference, Taipei, Taiwan.

Lucia S, Engell S (2013) Robust nonlinear model predictive control of a batch bioreactor using multi-stage stochastic programming, European Control ConfeSCHrence (ECC), Zurich, Switzerland.

MOSEK ApS. (2019) The MOSEK optimization toolbox for MATLAB manual. Version 9.0.

Oravec J, Bakošová M (2012) Robust Constrained MPC Stabilization of a CSTR, Acta Chimica Slovaca, 5: 153–158.

Oravec J, Bakošová M (2015) Software for efficient LMI-based robust MPC design, Proceedings of the 20th International Conference on Process Control, Štrbské Pleso, Slovakia, 272–277.

Oravec J, Bakošová M, Hanulová L, Horváthová M (2017) Design of Robust MPC with Integral Action for a Laboratory Continuous Stirred-Tank Reactor, Proceedings of the 21st International Conference on Process Control, Štrbské Pleso, Slovakia, 459–464.

Pons MN, Mourot G, Ragot J (2011) Modeling and simulation of a carrousel for long-term operation, IFAC World Congress, Milan, Italy.

Rajinikanth V, Latha K (2010) Identification and Control of Unstable Biochemical Reactor, International Journal of Chemical Engineering and Applications, 1: 106–111.

Ramaswamya S, Cutrightb TJ, Qammar HK (2005) Control of a continuous bioreactor using model predictive control, Process Biochemistry, 40: 2763–2770.

Rodrigues JAD, Toledo ECV, Maciel Filho R (2002) A tuned approach of the predictive-adaptive GPC controller applied to a fed-batch bioreactor using complete factorial design, Computers & Chemical Engineering, 26: 1493–1500.

Vinopraba T, Sivakumaran N, Narayanan S, Radhakrishnan TK (2013) Design of fractional order controller for Biochemical reactor, IFAC Proceedings Volumes, 46: 205–208.

Smets IY, Claes JE, November EJ, Georges BP, Van Impe JF (2004) Optimal adaptive control of (bio)chemical reactors: past present and future, Journal of Process Control, 14: 795–805.

Trautenberger R (2017) Modelling and control of a cascade of biochemical reactors, Bachelor Thesis, SCHK, Bratislava, Slovakia.